Zastosowanie mikrotomografii w geoinżynierii: od nauki do praktyki inżynierskiej

Łukasz Kaczmarek

Warszawa, 20.04.2017

Prezi

BADANIA NUAKOWE

Zastosowanie mikrotomografii w geoinżynierii: od nauki do praktyki inżynierskiej

Łukasz Kaczmarek

Warszawa, 20.04.2017

ZASTOSOWANIE W PRAKTYCE

Prezi

High-resolution computed microtomography

The μCT allows for precise analysis of the homogeneity and structure geometry, as well as development of numerical models. The theoretical basis of μCT was very well described by Ketcham and Carlson (2001); Baker, Mancini et al. (2012) and by Gnudde and Boone (2013) in the review papers. Examples of μCT analysis of various type of porous media were presented in articles by Appoloni, Fernandes and Rodrigues (2007); Bielecki et al. (2013). μCT has also been used for analysis of flow through rock specimens by: Petchsingto and Karpyn (2009); Dvorkin et al. (2009). Literature data and our own investigations indicate that μCT analysis has a wide range of applications in geology.

$$\kappa = \mu_s \rho_s + \mu_w \theta \rho_w$$

ρ_s - density of solid material (g cm^{-3}),
μ_w - water mass attenuation coefficient (κ/ρ, cm^2 g^{-1}),
ρ_w - density of water (g cm^{-3}),
Θ - volumetric rock water content (cm^3 cm^{-3}).

$$\Delta I = -\kappa I \Delta x$$

ΔI - change in intensity of X-ray beam interacting with absorber of thickness (keV),
Δx - absorber of thickness (cm).

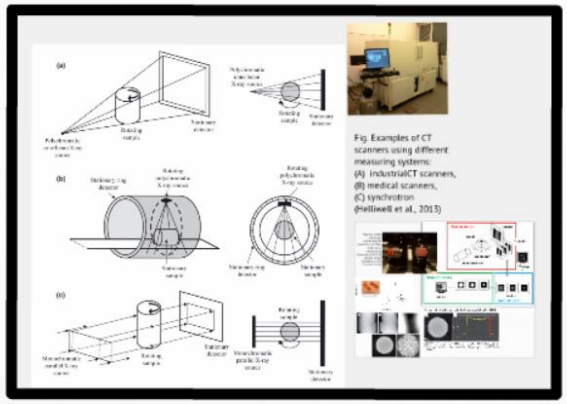

Fig. Examples of CT scanners using different measuring systems: (A) IndustrialCT scanners, (B) medical scanners, (C) synchrotron (Helliwell et al., 2013)

nalysis has a wide range of applications in geology.

$$\kappa = \mu_s \rho_s + \mu_w \theta \rho_w$$

ρ_s - density of solid material (g cm^{-3}),
μ_w - water mass attenuation coefficient (κ/ρ, cm^2 g^{-1}),
ρ_w - density of water (g cm^{-3}),
Θ - volumetric rock water content (cm^3 cm^{-3}).

$$\Delta I = -\kappa I \Delta x$$

ΔI - change in intensity of X-ray beam interacting with absorber of thickness (keV),
Δx - absorber of thickness (cm).

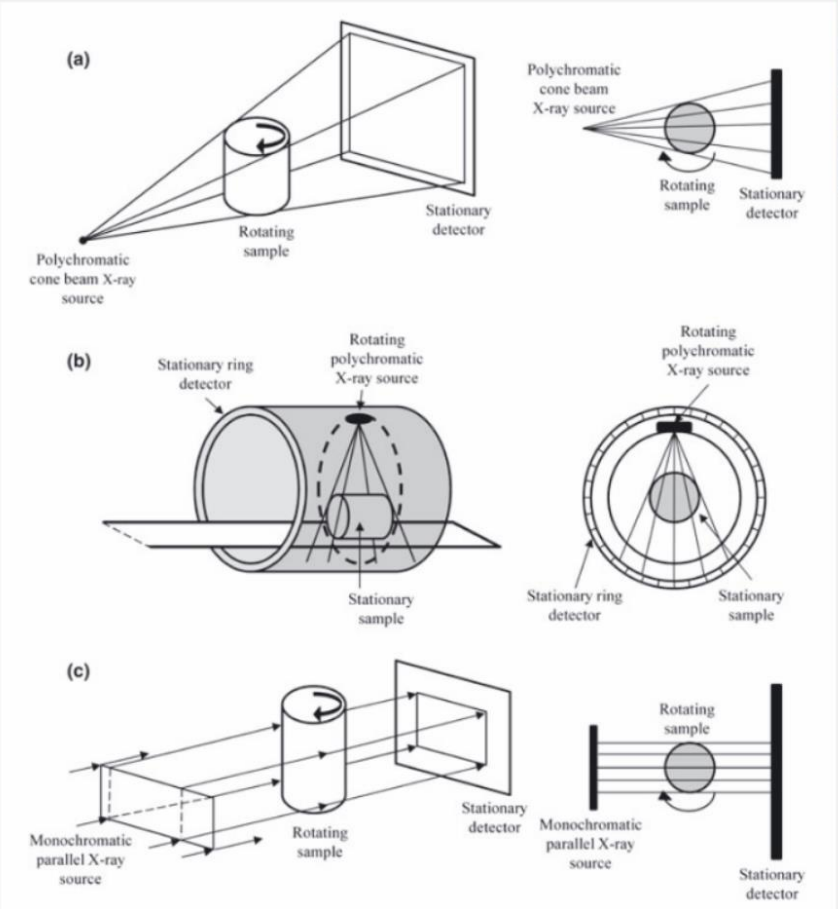

Fig. Examples of CT scanners using different measuring systems:
(A) industrialCT scanners,
(B) medical scanners,
(C) synchrotron
(Helliwell et al., 2013)

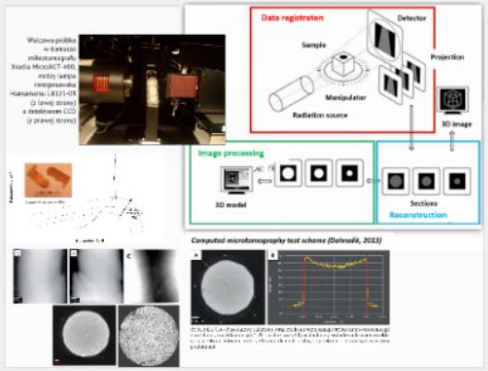

Walcowa próbka w komorze mikrotomografu Xradia MicroXCT-400, midzy lampa rentgenowska Hamamatsu L8121-03 (z lewej strony) a detektorem CCD (z prawej strony)

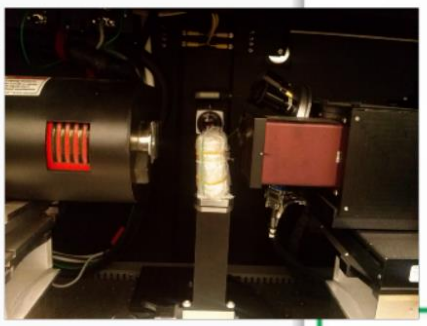

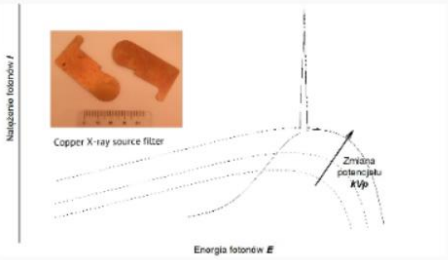

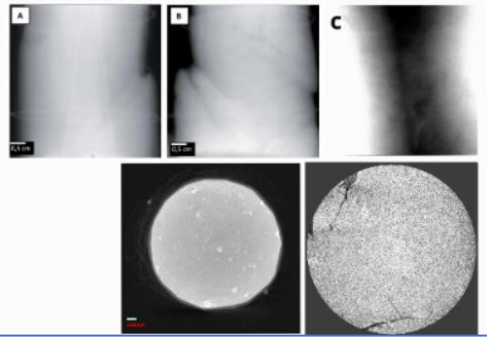

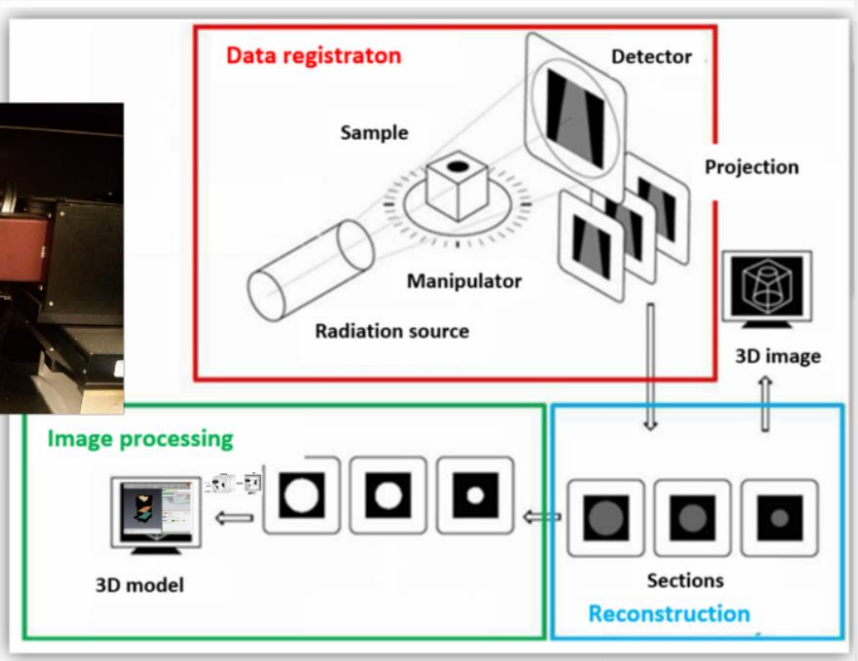

Computed microtomography test scheme (Dohnalik, 2013)

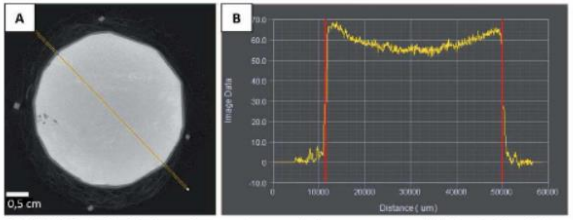

RYSUNEK 7. A – Przykładowy zaburzony obraz przekroju poprzecznego próbki iłu mio-plioceńskiego zjawiskiem „twardnienia wiązki"; B – wykres wartości pochłaniania promieniowania rentgenowskiego w przekroju liniowym próbki, gdzie oś odciętych to długość przekroju, a oś rzędnych to wartość pochłaniania

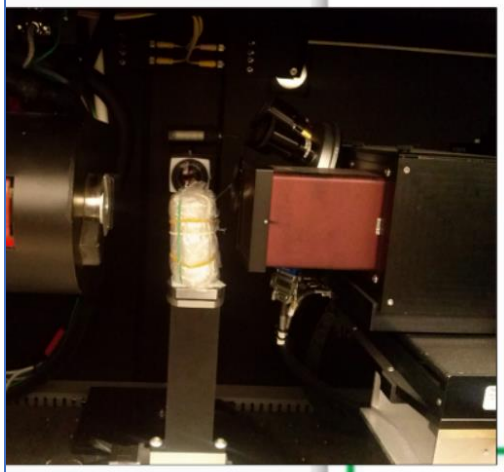

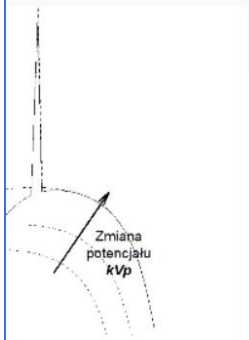

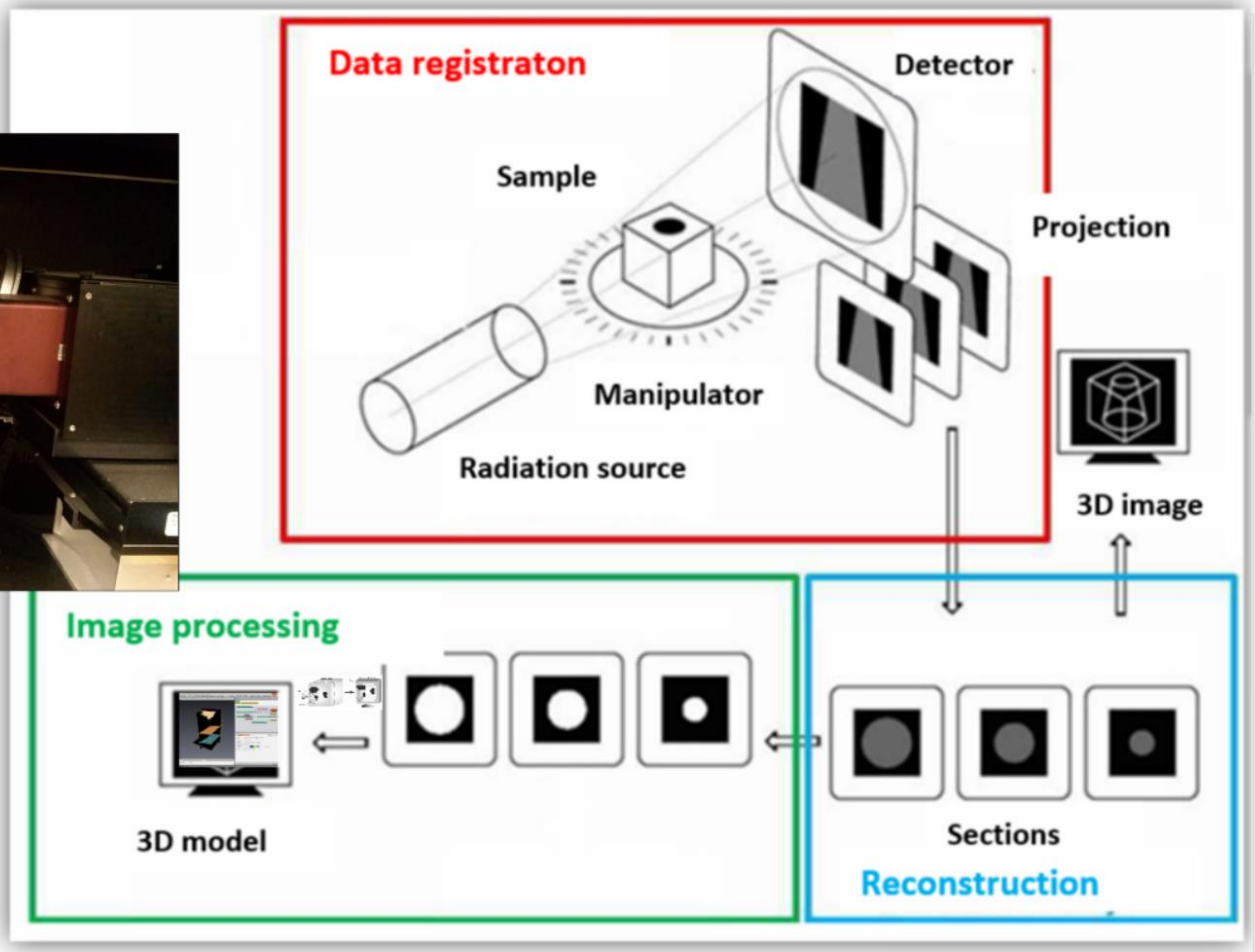

Computed microtomography test scheme (Dohnalik, 2013)

Prezi

Image processing

3D model

Prezi

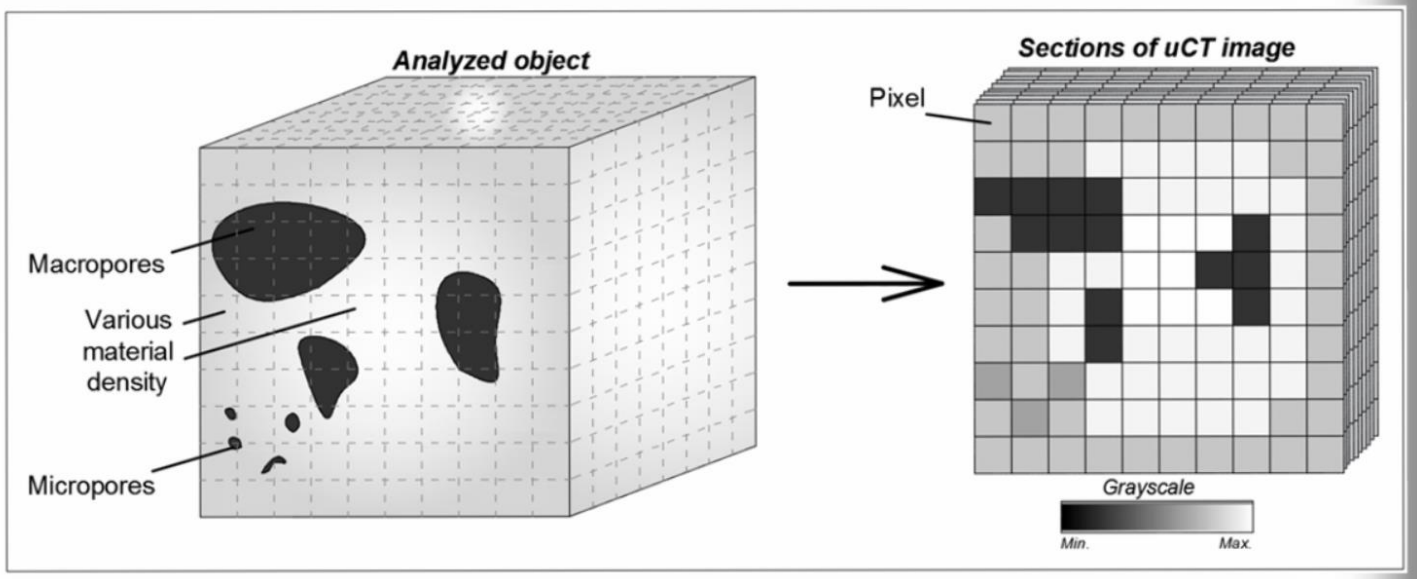
Analyzed object
Macropores
Various material density
Micropores
Sections of uCT image
Pixel
Grayscale
Min.
Max.

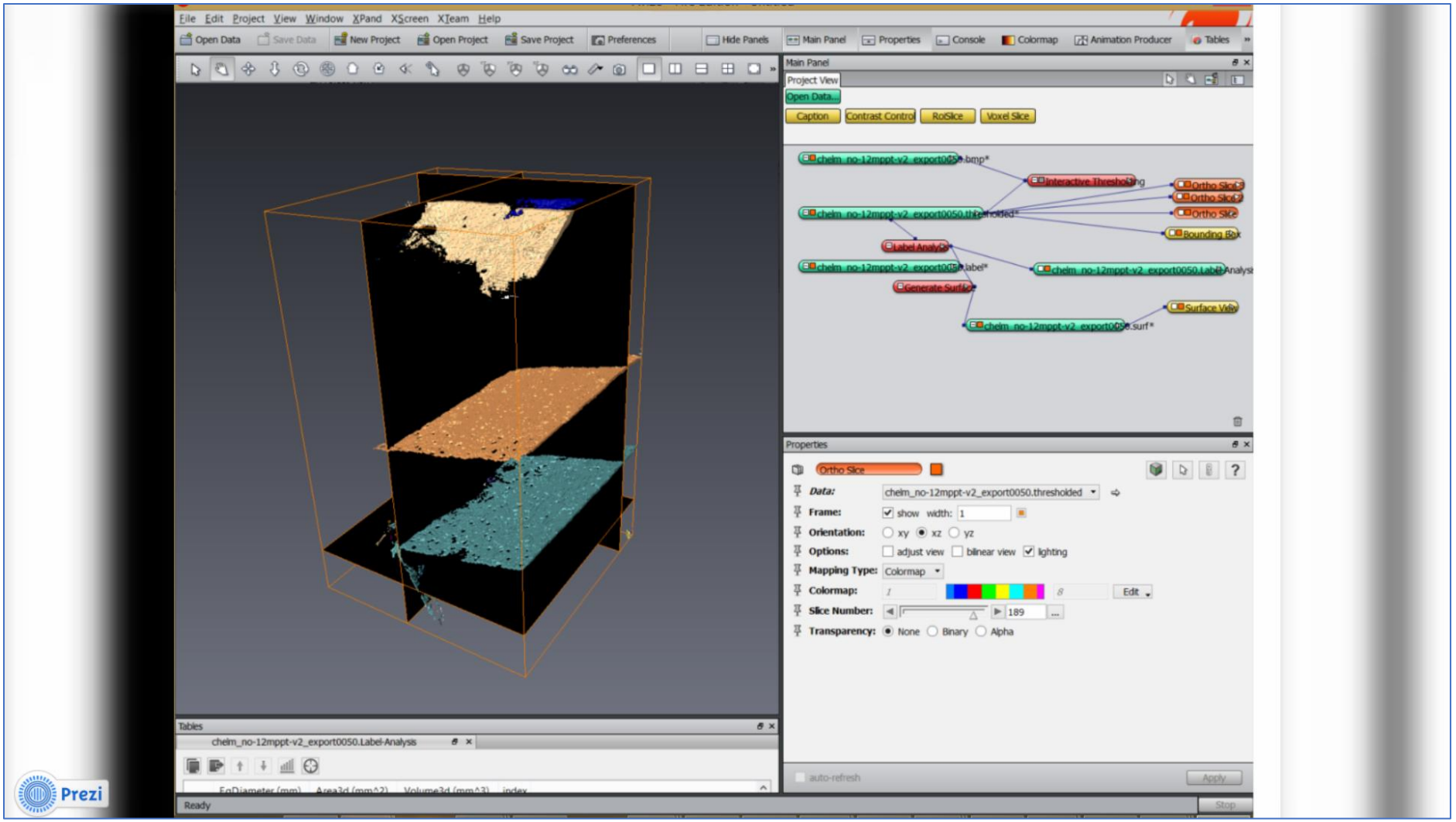
File Edit Project View Window XPand XScreen XTeam Help
Open Data
Save Data
New Project
Open Project
Save Project
Preferences
Hide Panels
Main Panel
Properties
Console
Colormap
Animation Producer
Tables
Main Panel
Project View
Open Data...
Caption
Contrast Control
RoiSlice
Voxel Slice
Properties
Ortho Slice
Data:
chelm_no-12mppt-v2_export0050.thresholded
Frame:
show
width:
Orientation:
xy
xz
yz
Options:
adjust view
bilinear view
lighting
Mapping Type:
Colormap
Colormap:
Edit
Slice Number:
189
Transparency:
None
Binary
Alpha
auto-refresh
Apply
Tables
chelm_no-12mppt-v2_export0050.Label-Analysis
Ready
Stop

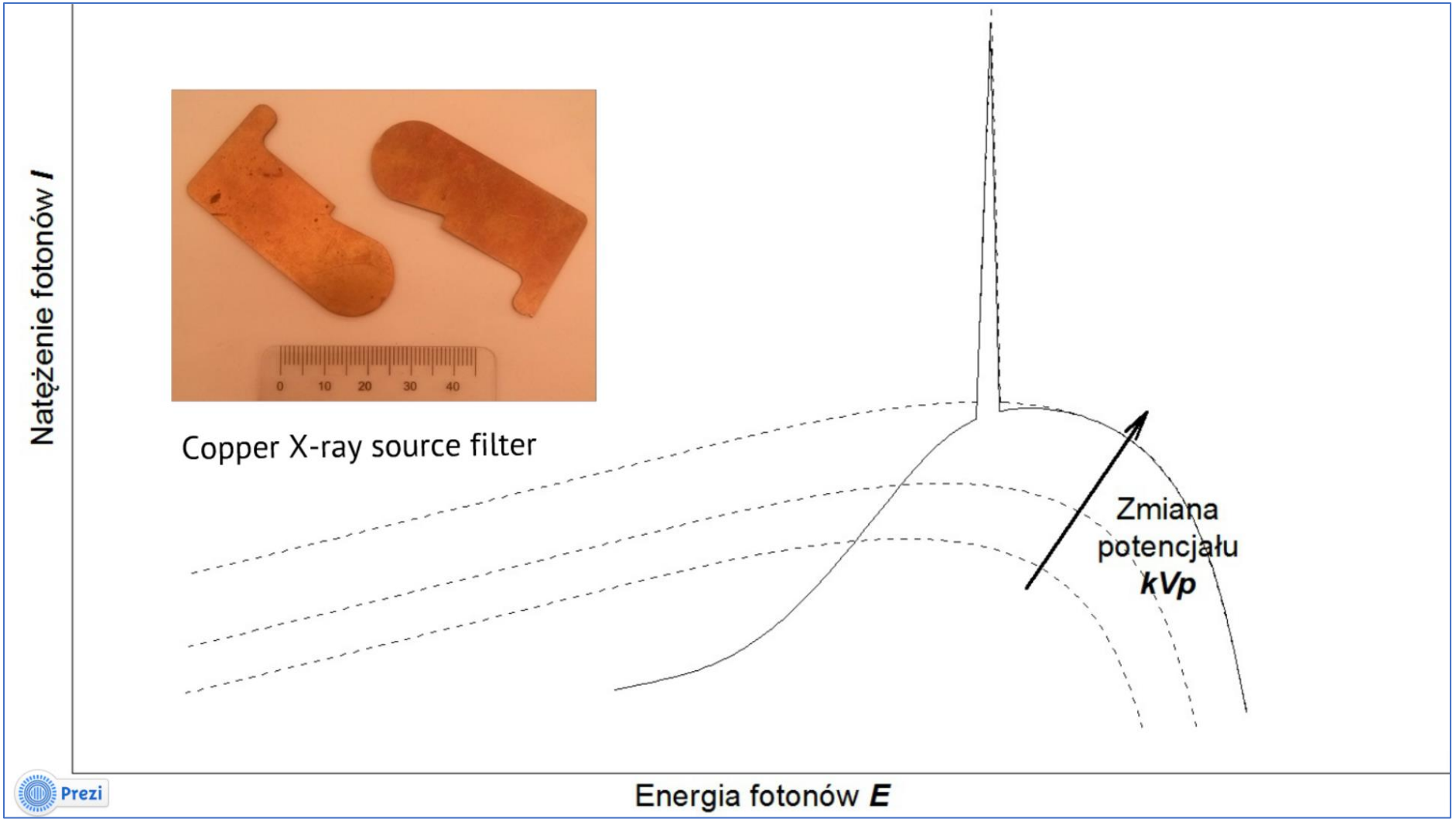
Natężenie fotonów *I*
Copper X-ray source filter
Zmiana potencjału *kVp*
Energia fotonów *E*
Prezi

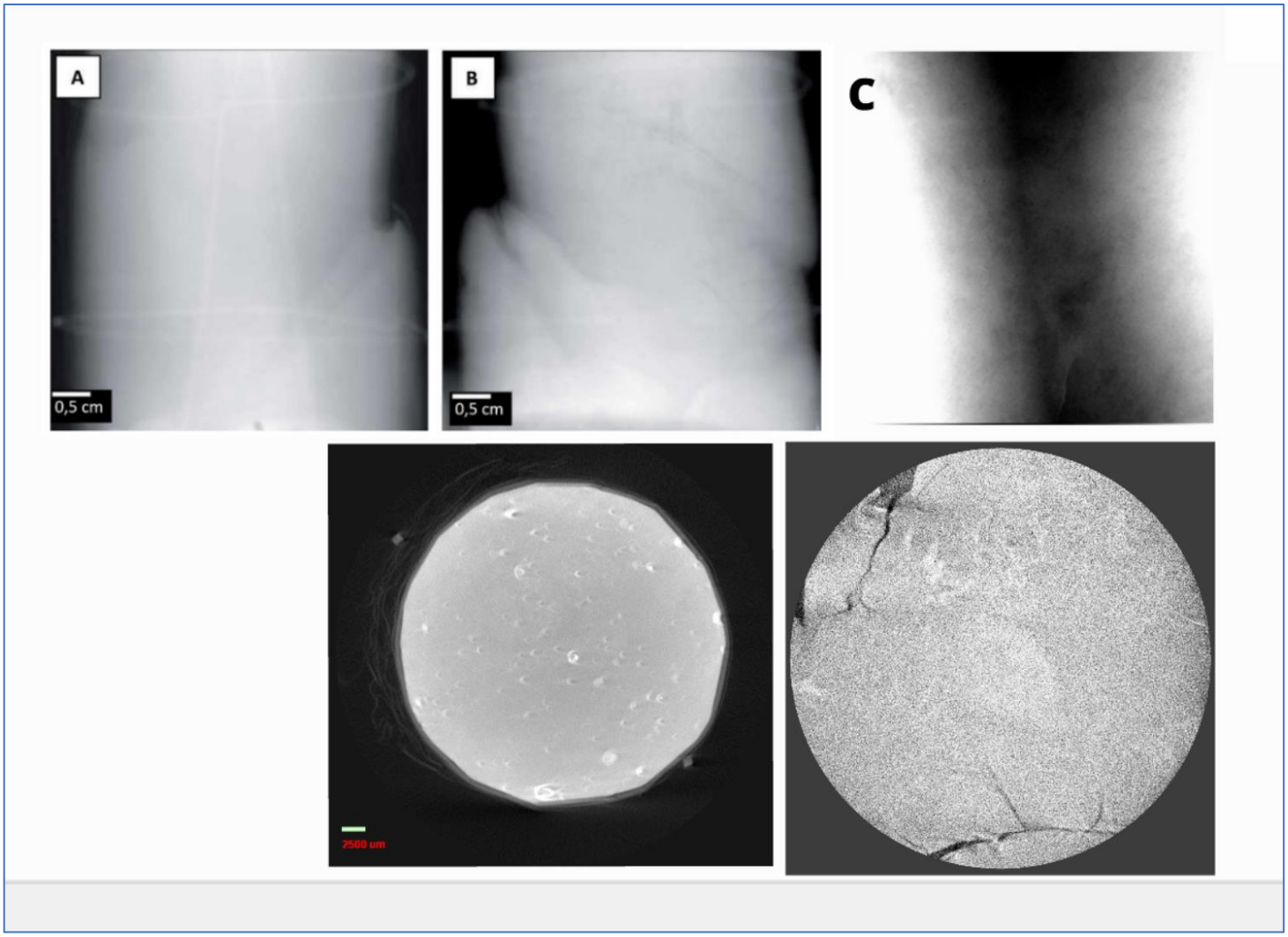
A
0,5 cm
B
0,5 cm
C
2500 um

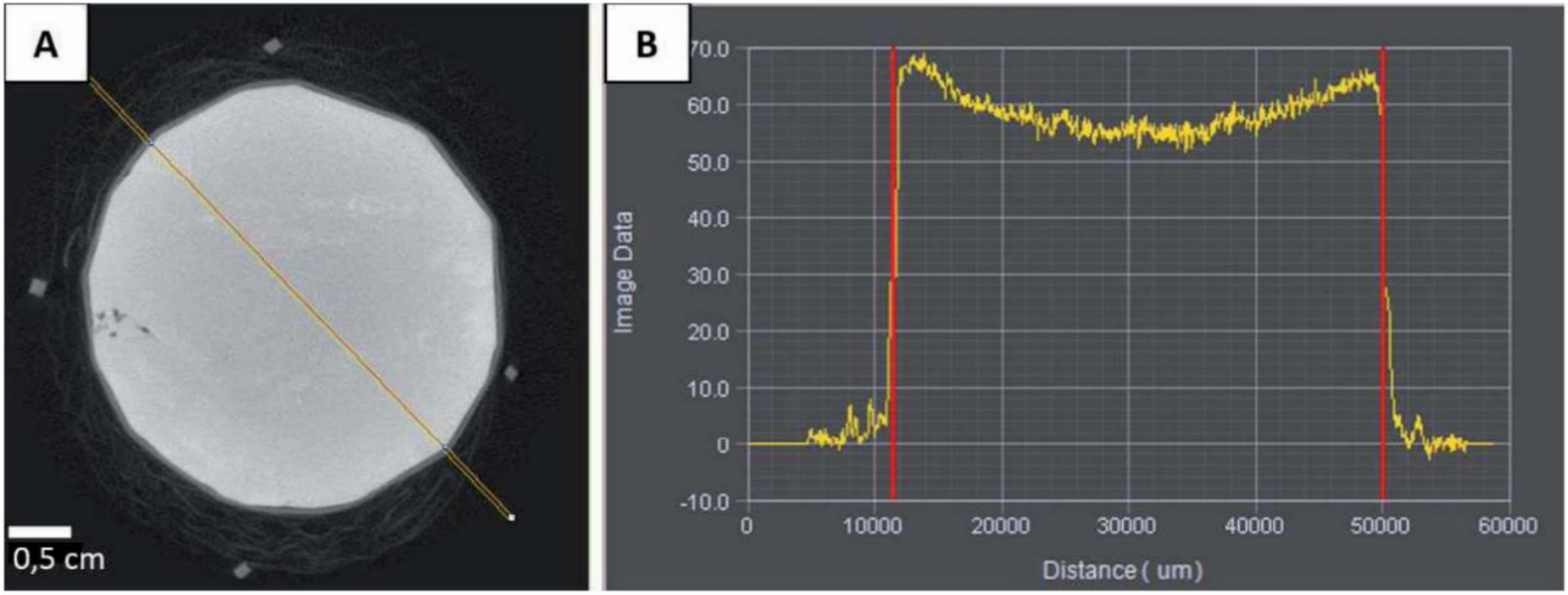

RYSUNEK 7. A – Przykładowy zaburzony obraz przekroju poprzecznego próbki iłu mio-plioceńskiego zjawiskiem „twardnienia wiązki”; B – wykres wartości pochłaniania promieniowania rentgenowskiego w przekroju liniowym próbki, gdzie oś odciętych to długość przekroju, a oś rzędnych to wartość pochłaniania

Prezi

Magnetyczny Rezonans Jądrowy

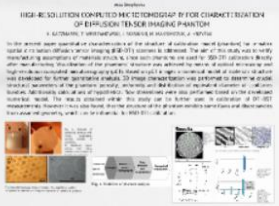

BADANIA NUAKOWE

Wietrzenie skał

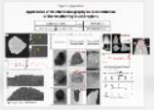

Geofizyka

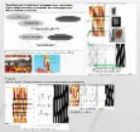

Zastosowanie mikrotom
od nauki do praktyki inż

Łukasz Kaczmarek

Prezi

Acta Geophysica

HIGH-RESOLUTION COMPUTED MICROTOMOGRAPHY FOR CHARACTERIZATION OF DIFFUSION TENSOR IMAGING PHANTOM

Ł. KACZMAREK, T. WEJRZANOWSKI, J. SKIBIŃSKI, M. MAKSIMCZUK, A. KRZYŻAK

In the present paper quantitative characterization of the structure of calibration model (phantom) for b-matrix spatial distribution diffusion tensor imaging (BSD-DTI) scanners is addressed. The aim of this study was to verify manufacturing assumptions of materials structure, since such phantoms are used for BSD-DTI calibration directly after manufacturing. Visualization of the phantoms' structure was achieved by means of optical microscopy and high-resolution computed microtomography (μCT). Based on μCT images a numerical model of materials structure was developed for further quantitative analysis. 3D image characterization was performed to determine crucial structural parameters of the phantom: porosity, uniformity and distribution of equivalent diameter of capillaries bundles. Additionally calculations of hypothetical flow streamlines were also performed based on the developed numerical model. The results obtained within this study can be further used in calibration of DTI-BST measurements. However it was also found, that the structure of the phantom exhibits some flaws and discrepancies from assumed geometry, which can be influential for BSD-DTI calibration.

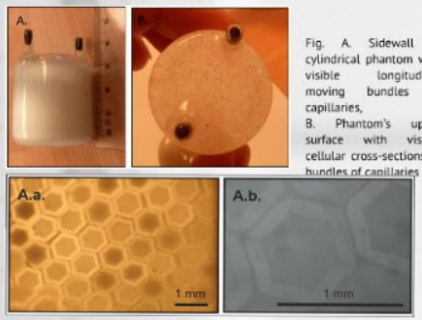

Fig. A. Sidewall of cylindrical phantom with visible longitudinal moving bundles of capillaries, B. Phantom's upper surface with visible cellular cross-sections of bundles of capillaries

Fig. Optical microscopy image of sample: A.a., Capillaries bundles of cylindrical phantom; A.b. Singular capillaries of cylindrical phantom

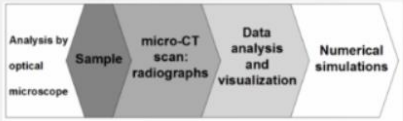

Fig. 1. Workflow of phantom analysis

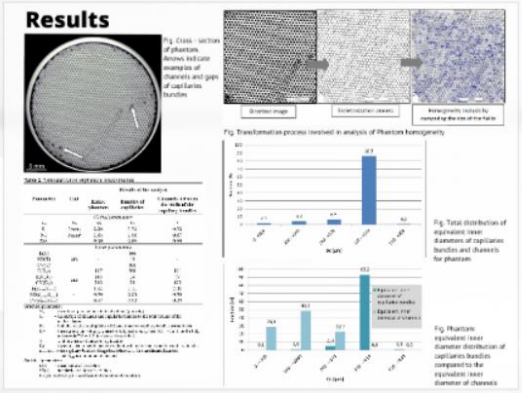

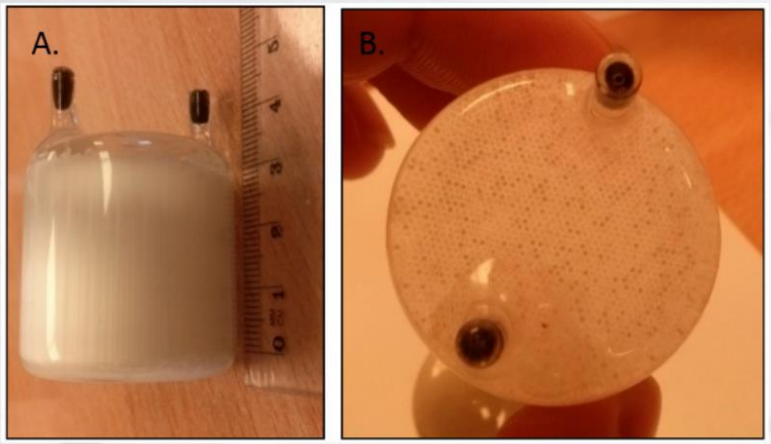

Fig. A. Sidewall of cylindrical phantom with visible longitudinal moving bundles of capillaries,
B. Phantom's upper surface with visible cellular cross-sections of bundles of capillaries

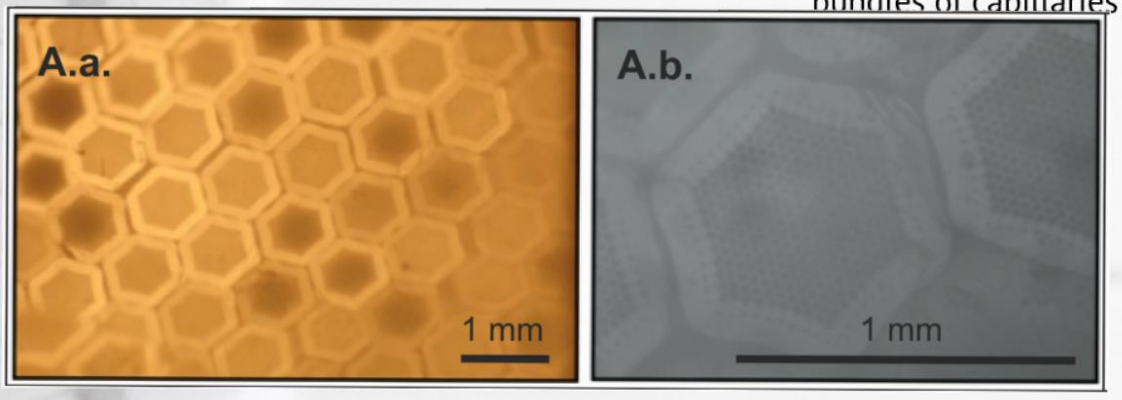

Fig. Optical microscopy image of sample: A.a., Capillaries bundles of cylindrical phantom; A.b. Singular capillaries of cylindrical phantom

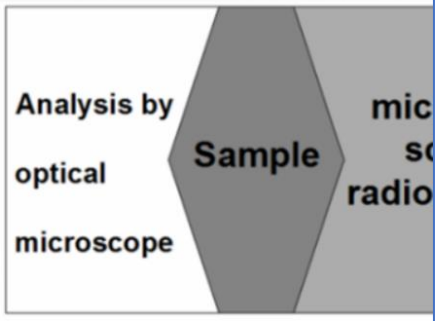

Fig. 1. Workflow of

Prezi

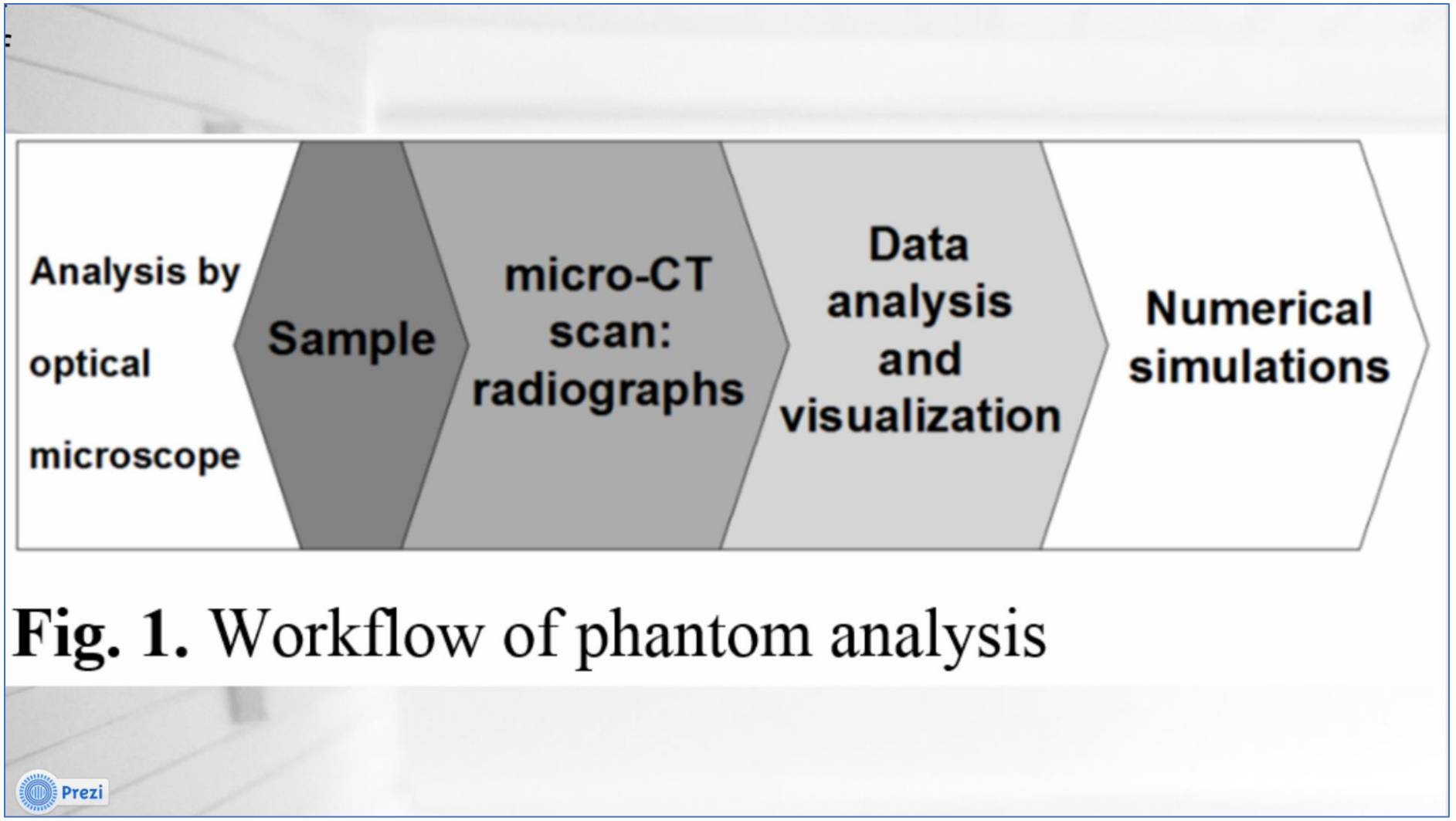

Fig. 1. Workflow of phantom analysis

Results

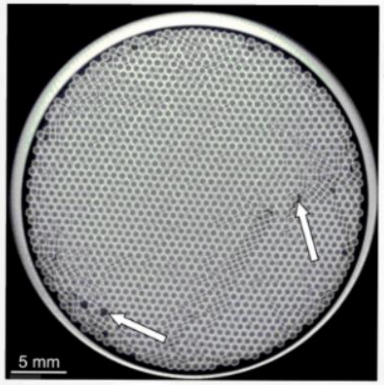

Fig. Cross - section of phantom. Arrows indicate examples of channels and gaps of capillaries bundles

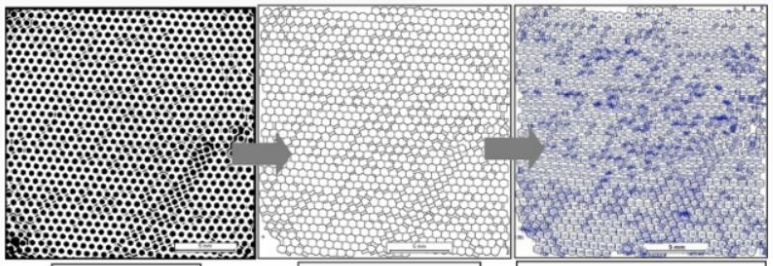

Fig. Transformation process involved in analysis of Phantom homogeneity

Table 2. Parameterization of phantom microstructure

Parameter	Unit	Results of the analysis		
		Entire phantom	Bundles of capillaries	Channels between the walls of the capillary bundles
Global parameters				
V_V	%	38	35	3
S_V	1/mm	2.29	1.96	0.32
N_A	1/mm²	2.85	1.98	0.87
DA	-	0.89	0.89	0.90
Local parameters				
E(T)	µm	-	166	-
SD(T)			18	
CV(T)			108	
E(D_C)	µm	437	508	191
SD(D_C)		145	14	77
CV(D_C)		340	28	403
E(d_{max}/d_{min})	-	1.34	1.11	2.01
SD(d_{max}/d_{min})		0.50	0.03	0.59
CV(d_{max}/d_{min})		0.37	0.02	0.29

Structural parameters:
- V_V – the ratio of pore volume to total volume (porosity)
- S_V – the surface of channels and capillaries bundles to the total volume of the analyzed area
- N_A – both the relative multiplicity of channels and/or capillary bundles per unit area
- DA – the degree of anisotropy, where for fully isotropic system DA = 0, and for the fully anisotropic DA = 1 (http://www.skyscan.be/)
- T – wall thickness of the capillary bundles
- D_C – the equivalent inner diameters (without walls) of channels and/or capillary bundles
- D_{max}/D_{min} – the capillary bundles elongation (where D_{max} is a maximum diameter, and D_{min} is a minimum diameter)

Statistical parameters:
- E(x) – mean value of variable x
- SD(x) – standard deviation of variable x
- CV(x) =SD(x)/E(x) – coefficient of variation of variable x

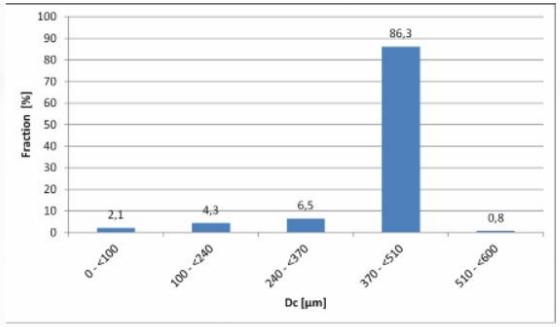

Fig. Total distribution of equivalent inner diameters of capillaries bundles and channels for phantom

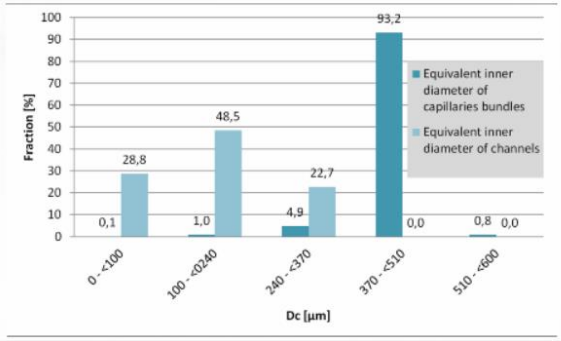

Fig. Phantom: equivalent inner diameter distribution of capillaries bundles compared to the equivalent inner diameter of channels

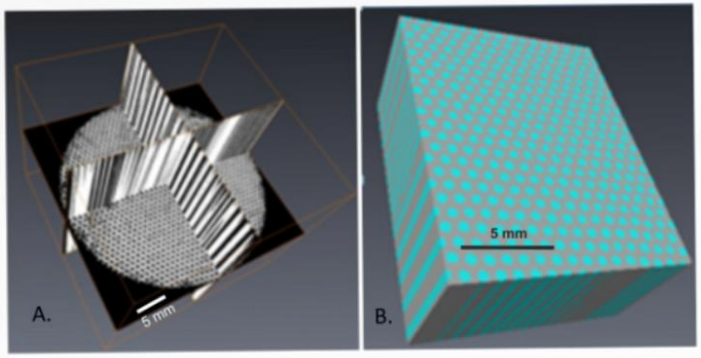

Fig. Phantom visualization: A - binarized cross-sections;
B - capillaries without deleted channels

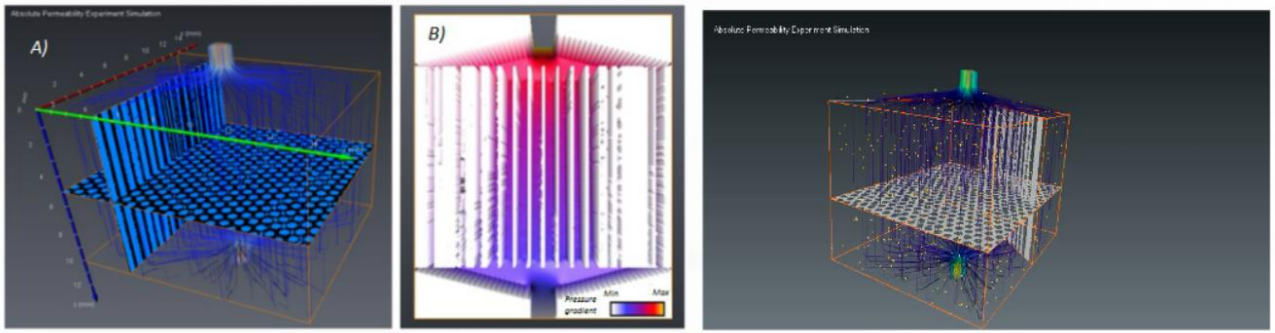

Fig. Visualization of A – streamlines, B - pressure gradient in phantom

Prezi

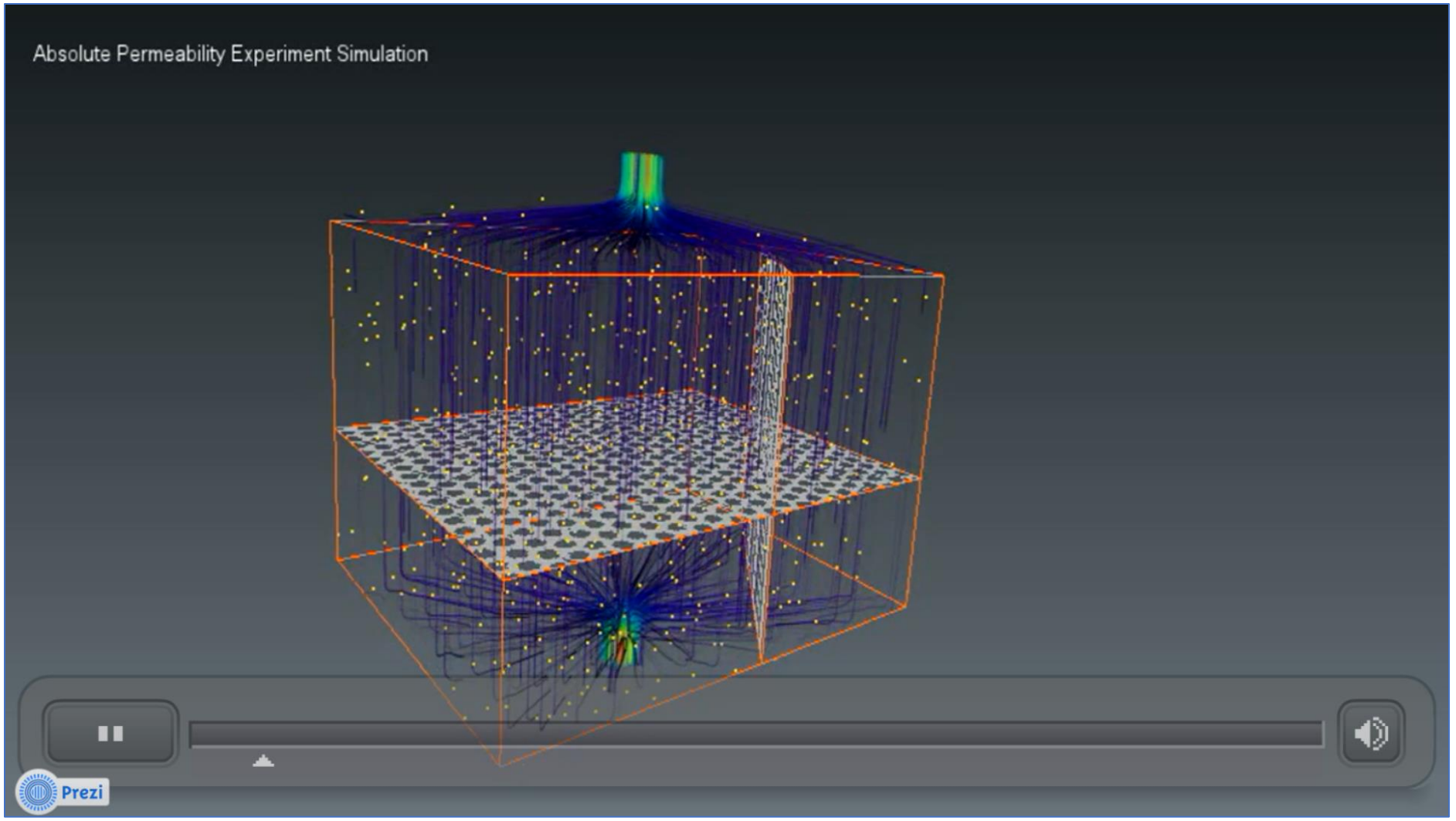
Absolute Permeability Experiment Simulation
Prezi

Magnetyczny Rezonans Jądrowy

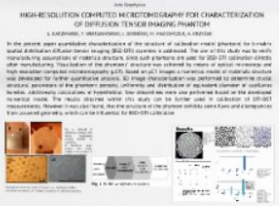

BADANIA NUAKOWE

Wietrzenie skał

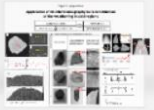

Geofizyka

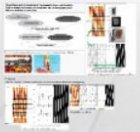

Zastosowanie mikrotom
od nauki do praktyki inży

Łukasz Kaczmarek

Prezi

Paper in preparation

Application of 3D-microtomography to reconstruction of the weathering in cold regions

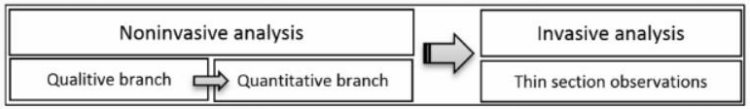

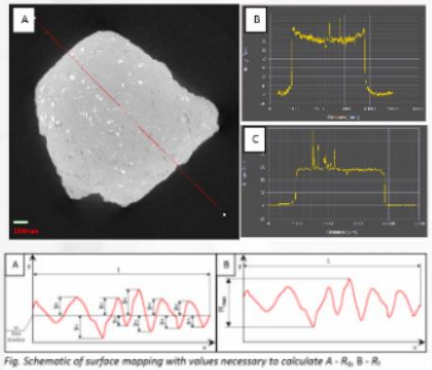

Fig. Schematic of surface mapping with values necessary to calculate A - R_a, B - R_t

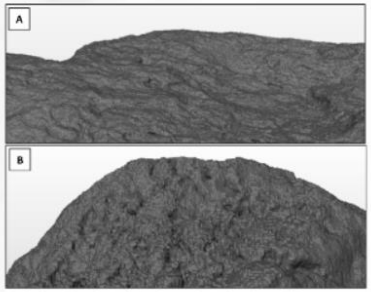

Fig. Surface of sample 1 affecting by mechanical weathering (A) and biochemical weathering (B)

Table 2. 3-demensional numerical model and internal structure of rock sample

Serial number of sample	Sample photography	3-dimensional model of rock sample with visualization of pores inside rock samples	Disturb zones in the μCT internal structure cross-section of rock samples
1		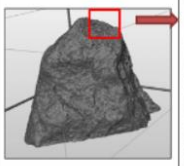	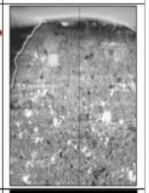
2		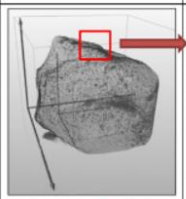	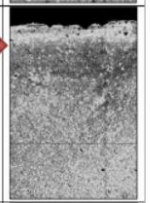
3		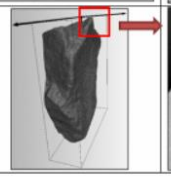	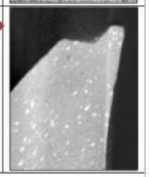

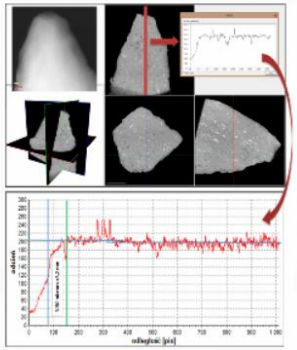

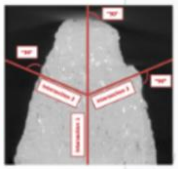

Table 3. Parameterization of rock structures

Parameter	Number of sample 1	2	3	Unit
Rock solid global parameters				
V_c	0.91	1.09	0.45	%
$E(S_v)$	0.196	0.147	0.285	
$SD(S_v)$	0.065	0.040	0.027	1/mm
$CV(S_v)$	0.023	0.275	0.095	
Biochemical weathering surface parameters				
V_c	1.16	2.68	0.32	%
$E(R_a)$	282	228	173	
$SD(R_a)$	159	168	119	μm
$CV(R_a)$	0.5	0.5	0.7	
$\Sigma(R_t)$	1180	971	714	
$SD(R_t)$	546	444	465	μm
$CV(R_t)$	0.5	0.5	0.7	
Mechanical weathering surface parameters				
V_c	1.07	1.45	0.20	%
$E(R_a)$	181	129	139	
$SD(R_a)$	118	70	85	μm
$CV(R_a)$	0.6	0.6	0.6	
$\Sigma(R_t)$	715	545	551	
$SD(R_t)$	359	269	271	μm
$CV(R_t)$	0.5	0.5	0.5	

Structural parameters:
V_c – the ratio of pore volume to total volume (porosity)
S_v – the surface of discords and capillaries bundles to the total volume of the analytical area
R_a – the mean square deviation of the profile
R_t – the distance between the highest point and recess of the profile
Statistical parameters:
$E(x)$ – mean value of variable x
$SD(x)$ – standard deviation of variable x
$CV(x) = SD(x)/E(x)$ – coefficient of variation of variable x

Prezi

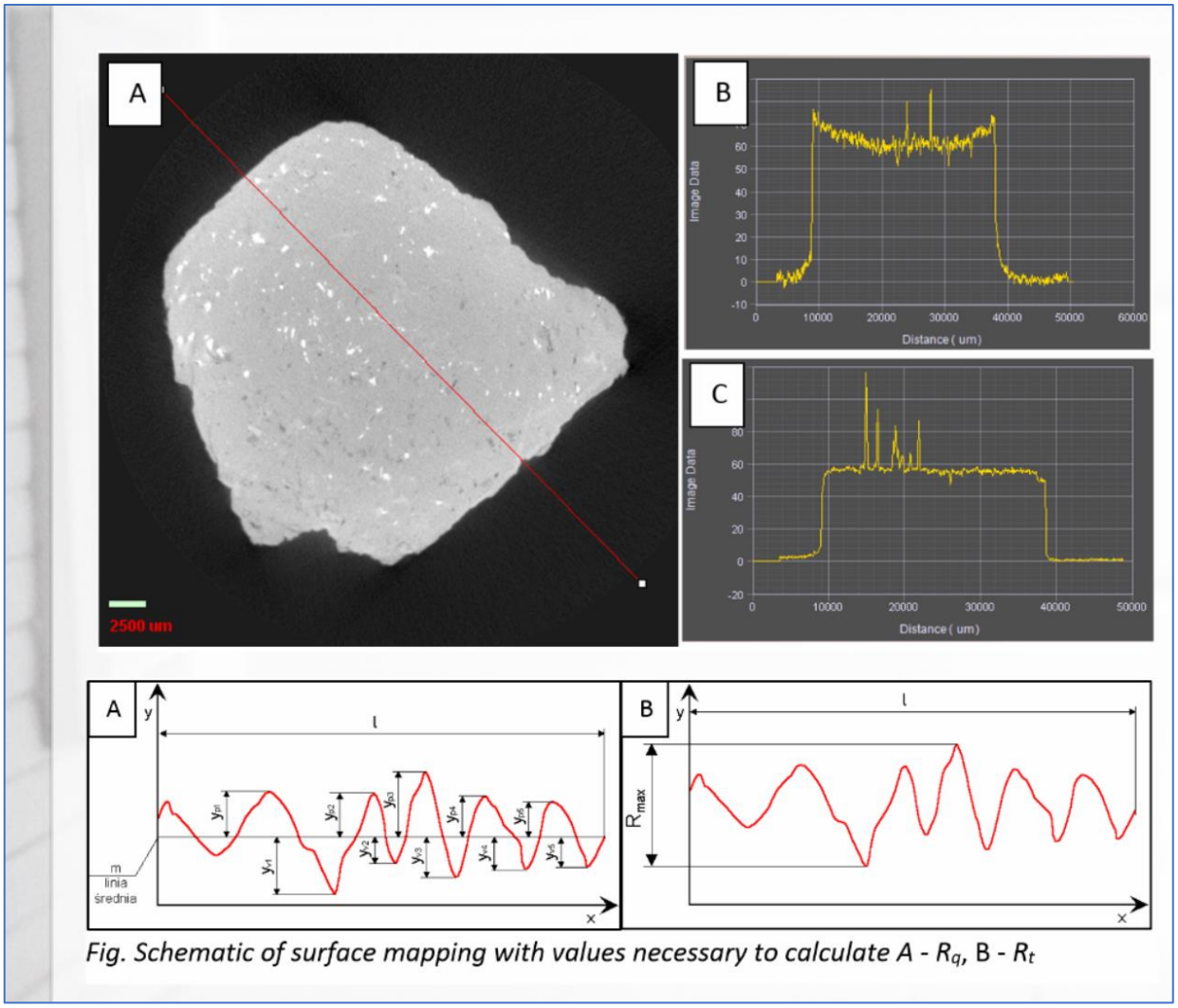

Fig. Schematic of surface mapping with values necessary to calculate A - R_q, B - R_t

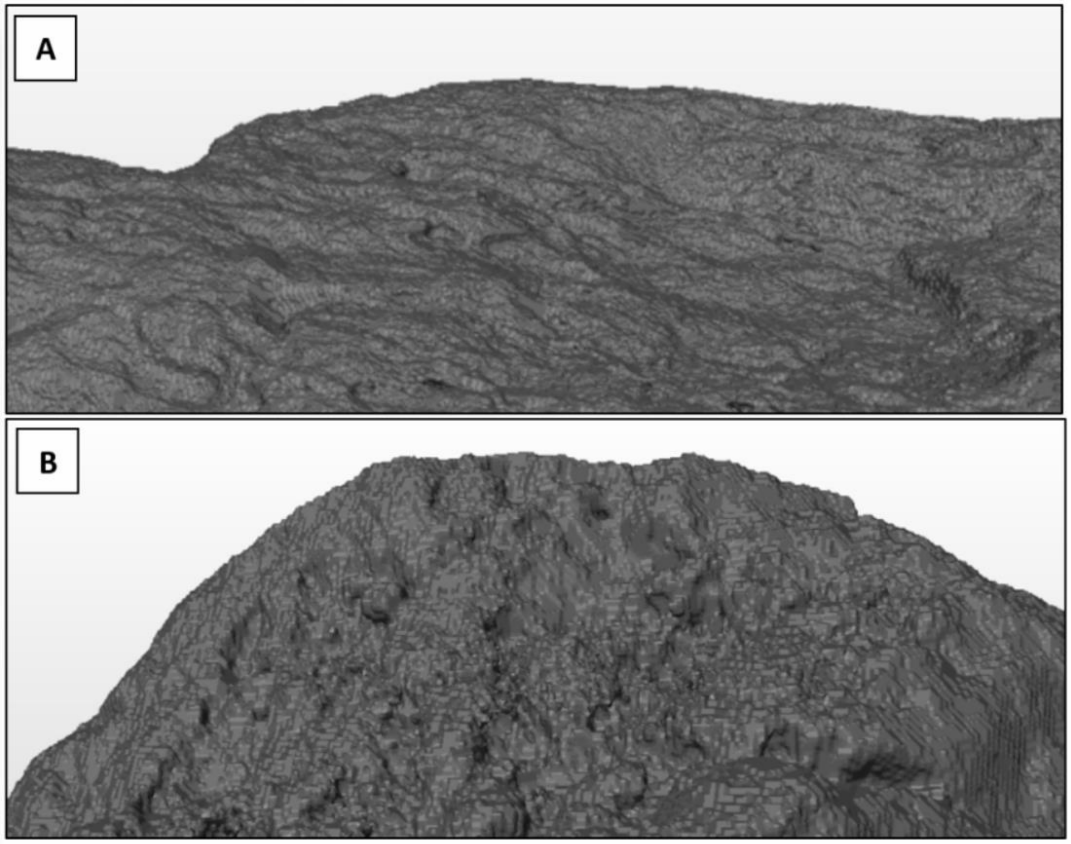

Fig. Surface of sample 1 affecting by mechanical weathering (A) and biochemical weathering (B)

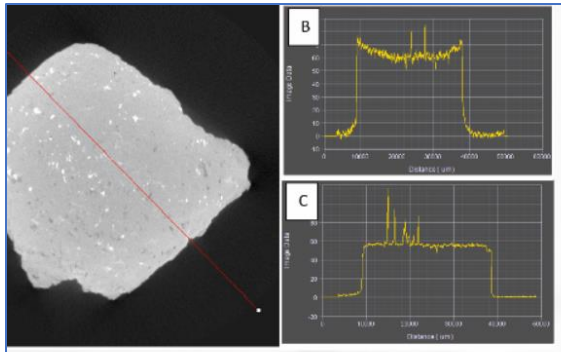

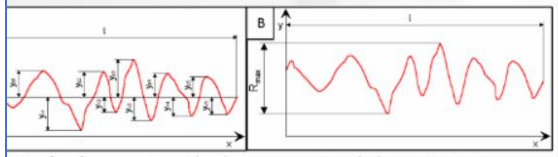

atic of surface mapping with values necessary to calculate A - R_q, B - R_t

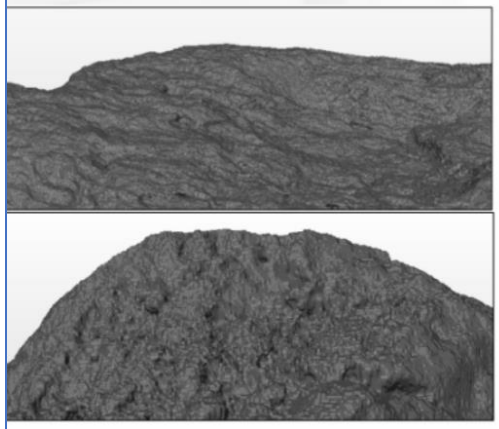

urface of sample 1 affecting by mechanical weathering (A)

ng (B)

Table 2. 3-demensional numerical model and internal structure of rock sample

Serial number of sample	Sample photography	3-dimensional model of rock sample with visualization of pores inside rock samples	Disturb zones in the µCT internal structure cross-section of rock samples
1		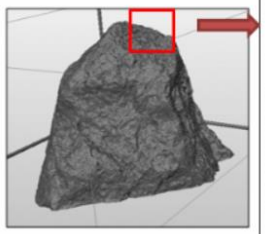	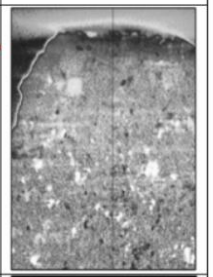
2		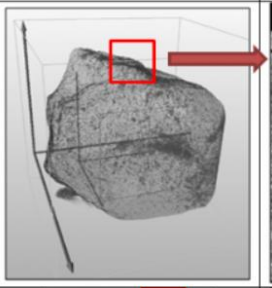	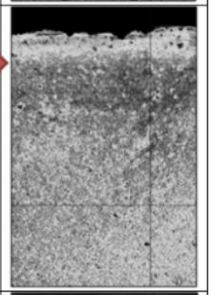
3	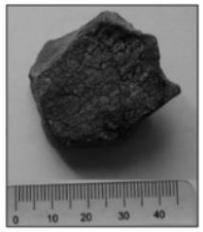	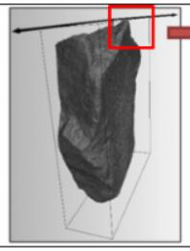	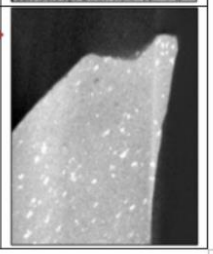

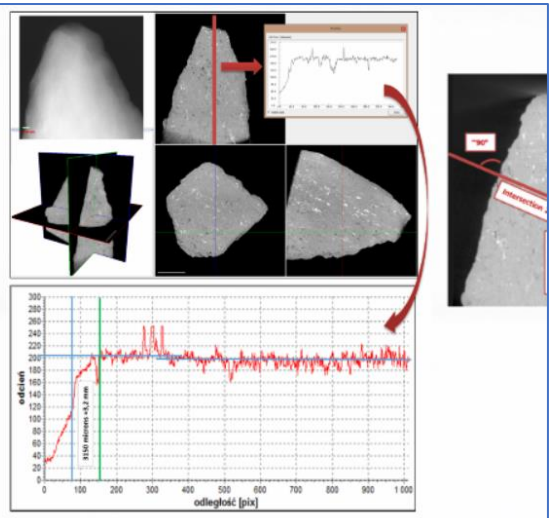

Table 3. Parameterization of rock structures

Parameter	Number of sample 1	2	3	Unit
Rock solid global parameters				
V_c	0.94	1.49	0.45	%
$E(S_v)$	0.196	0.147	0.283	
$SD(S_v)$	0.005	0.040	0.027	1/mm
$CV(S_v)$	0.023	0.275	0.095	
Biochemical weathering surface parameters				
V_c	1.16	2.68	0.32	%
$E(R_q)$	282	228	173	
$SD(R_q)$	156	108	119	µm
$CV(R_q)$	0.5	0.5	0.7	
$E(R_t)$	1180	971	714	
$SD(R_t)$	546	444	465	µm
$CV(R_t)$	0.5	0.5	0.7	
Mechanical weathering surface parameters				
V_c	1.07	1.45	0.20	%
$E(R_q)$	181	129	139	
$SD(R_q)$	118	70	83	µm
$CV(R_q)$	0.6	0.6	0.6	
$E(R_t)$	715	545	551	
$SD(R_t)$	359	269	271	µm
$CV(R_t)$	0.5	0.5	0.5	

Structural parameters:
V_V – the ratio of pore volume to total volume (porosity)
S_V – the surface of channels and capillaries bundles to the total volume of the analyzed area
R_q – the mean square deviation of the profile
R_t – the distance between the highest point and recess of the profile

Statistical parameters:
E(x) – mean value of variable x
SD(x) – standard deviation of variable x
CV(x) –SD(x)/E(x) – coefficient of variation of variable x

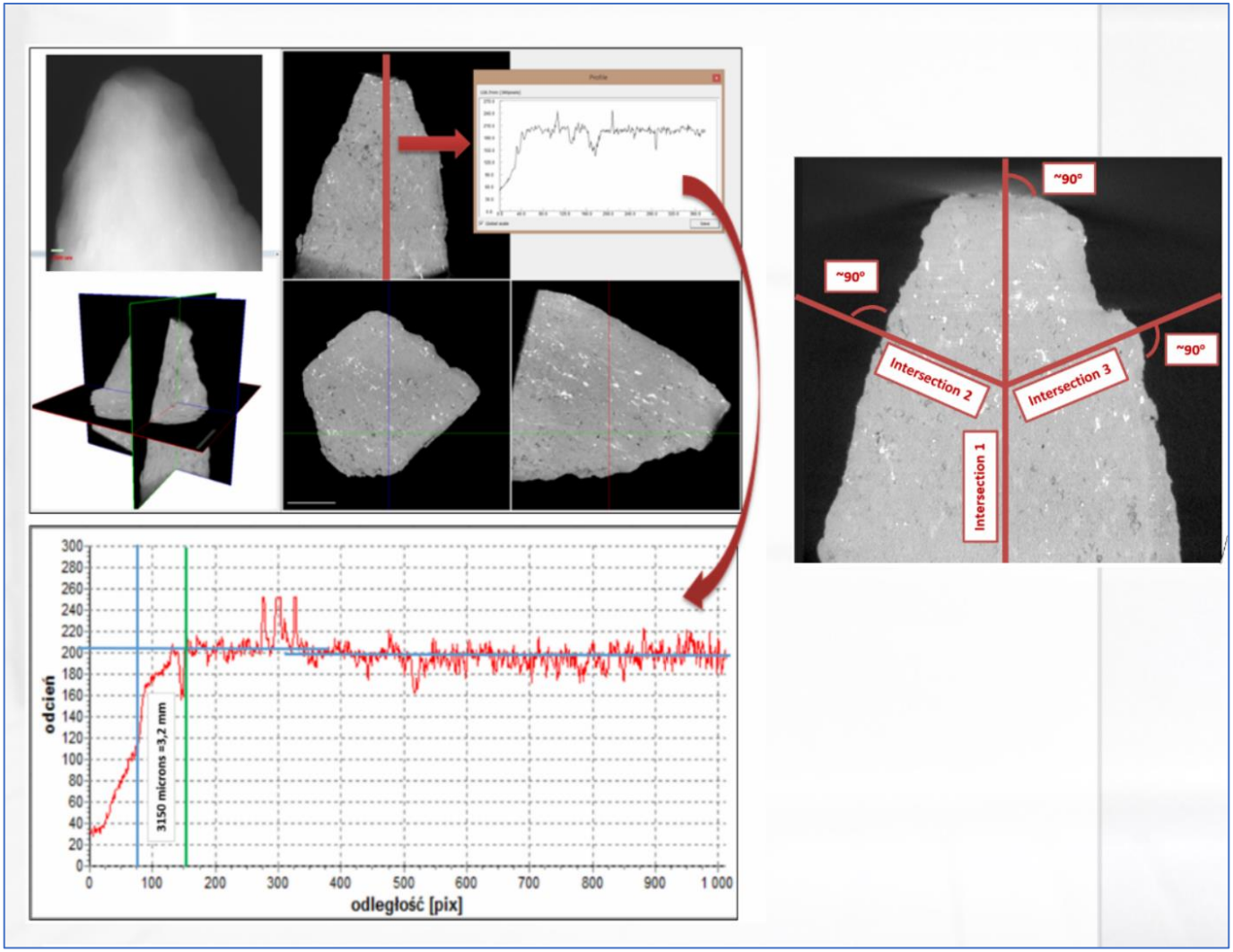
odcień
odległość [pix]
3150 microns =3,2 mm
~90°
~90°
~90°
Intersection 2
Intersection 3
Intersection 1

Table 3. Parameterization of rock structures

Parameter	Number of sample			Unit
	1	2	3	
Rock solid global parameters				
V_v	0.94	1.49	0.45	%
$E(S_v)$	0.196	0.147	0.283	
$SD(S_v)$	0.005	0.040	0.027	1/mm
$CV(S_v)$	0.023	0.275	0.095	
Biochemical weathering surface parameters				
V_v'	1.16	2.68	0.32	%
$E(R_q)$	282	228	173	
$SD(R_q)$	156	108	119	µm
$CV(R_q)$	0.5	0.5	0.7	
$E(R_t)$	1180	971	714	
$SD(R_t)$	546	444	465	µm
$CV(R_t)$	0.5	0.5	0.7	
Mechanical weathering surface parameters				
V_v''	1.07	1.45	0.20	%
$E(R_q)$	181	129	139	
$SD(R_q)$	118	70	83	µm
$CV(R_q)$	0.6	0.6	0.6	
$E(R_t)$	715	545	551	
$SD(R_t)$	359	269	271	µm
$CV(R_t)$	0.5	0.5	0.5	

Structural parameters:

V_V – the ratio of pore volume to total volume (porosity)

S_V – the surface of channels and capillaries bundles to the total volume of the analyzed area

R_q – the mean square deviation of the profile

R_t – the distance between the highest point and recess of the profile

Statistical parameters:

E(x) – mean value of variable x

SD(x) – standard deviation of variable x

CV(x) =SD(x)/E(x) – coefficient of variation of variable x

Magnetyczny Rezonans Jądrowy

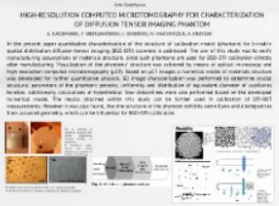

BADANIA NUAKOWE

Wietrzenie skał

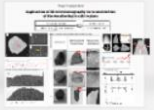

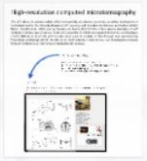

Geofizyka

Zastosowanie mikrotom
od nauki do praktyki inż

Łukasz Kaczmarek

Prezi

Novel Approach in Analysis of Fractures in Reservoir Rocks by Digital Image Processing of Computed Microtomography and Microresistivity Test Results

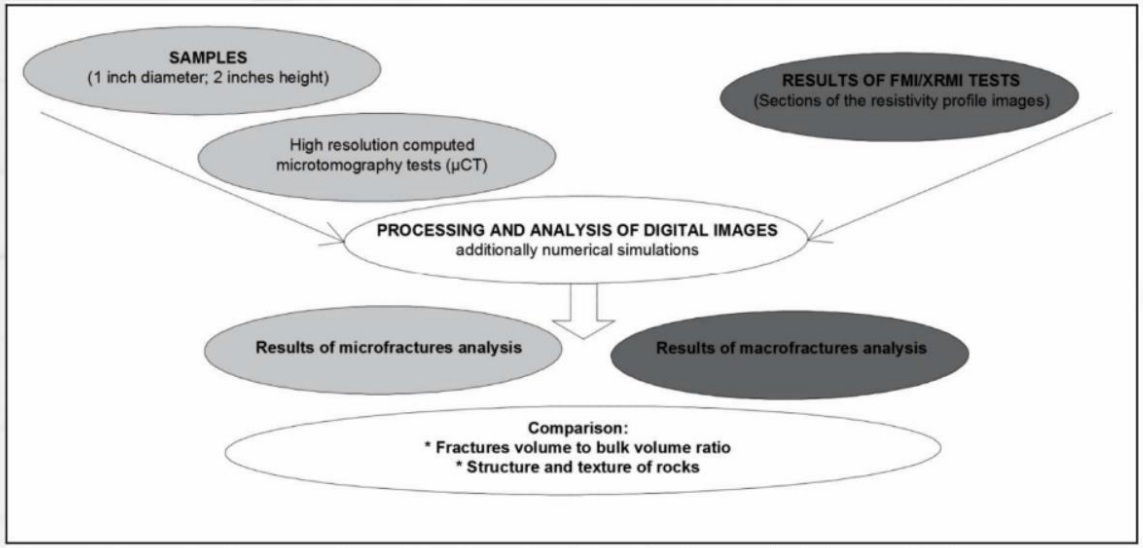

Fig. 4. Schematic diagram of combination of μCT and microresistivity methods

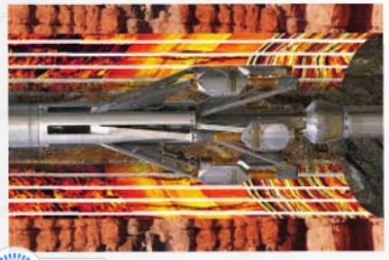

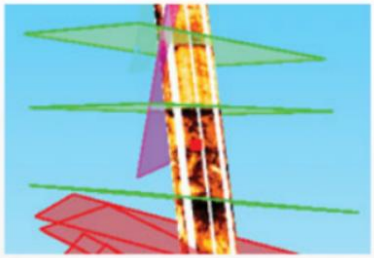

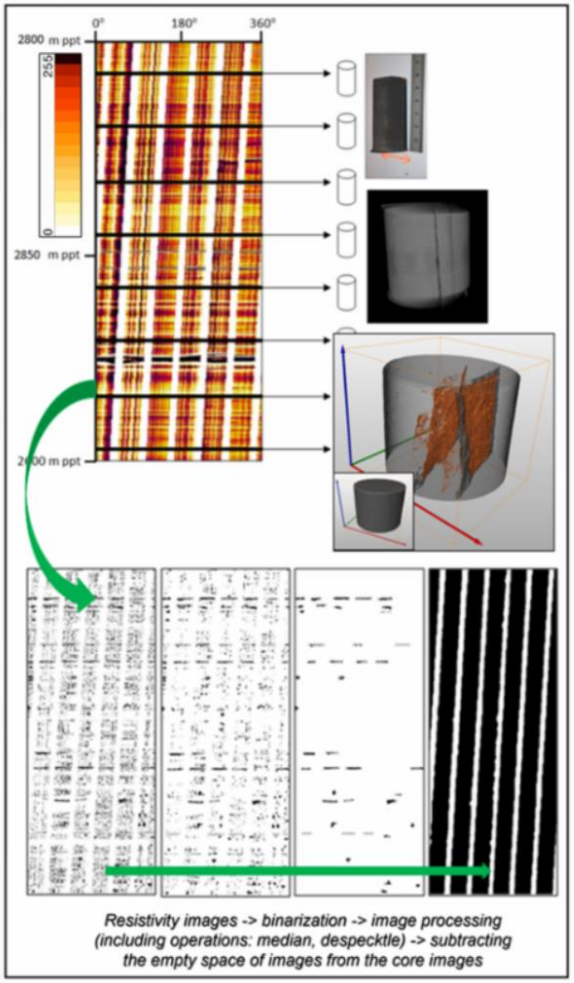

Fig. Schematic chart of use in combination of μCT results and microresistivity imaging

Prezi

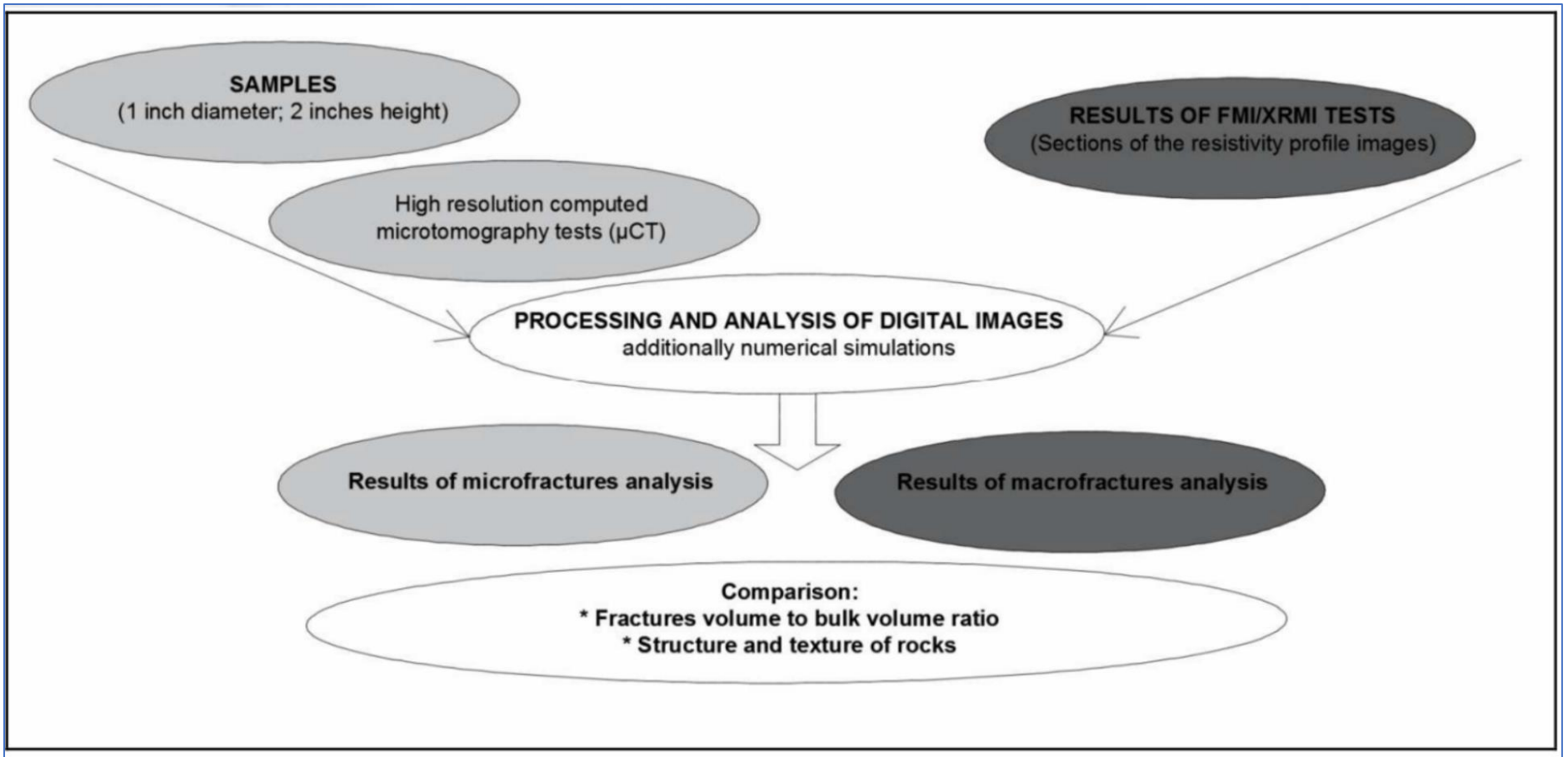

Fig. 4. Schematic diagram of combination of μCT and microresistivity methods

ir Rocks by
raphy and

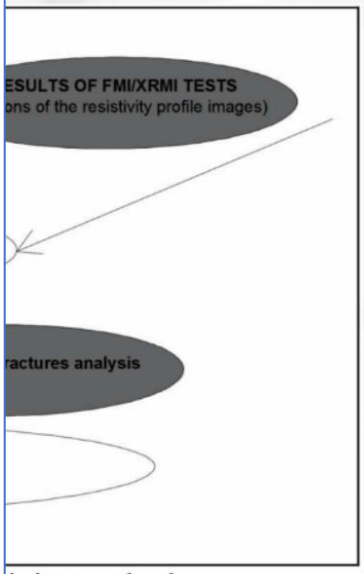

ivity methods

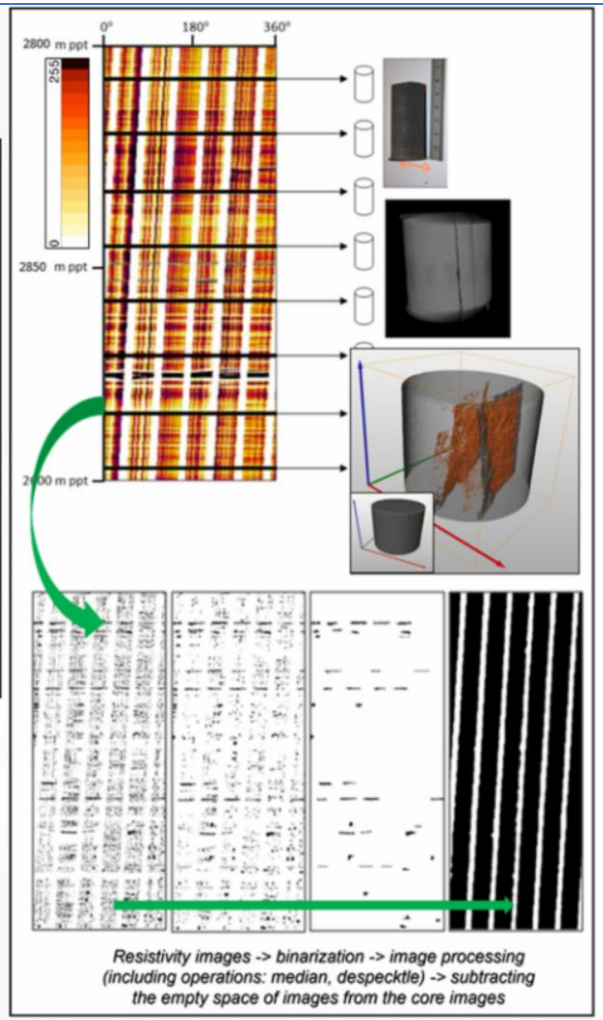

Fig. Schematic chart of use in combination of μCT results and microresistivity imaging

Zastosowanie mikrotomografii w geoinżynierii: od nauki do praktyki inżynierskiej

Łukasz Kaczmarek

Warszawa, 20.04.2017

BADANIA NUAKOWE

Magnetyczny Rezonans Jądrowy

Wietrzenie skał

Geofizyka

ZASTOSOWANIE W PRAKTYCE

Komputerowa analiza właściwości zbiornikowych przestrzeni porowej piaskowców oraz ich wytrzymałości, na podstawie mikrotomografii rentgenowskiej

Przebieg pełzania iłu neogeńskiego z Warszawy w badaniach trójosiowych z wykorzystaniem mikrotomografii komputerowej

fii w geoinżynierii:
'skiej

Warszawa, 20.04.2017

ZASTOSOWANIE W PRAKTYCE

Komputerowa analiza właściwości zbiornikowych przestrzeni porowej piaskowców oraz ich wytrzymałości, na podstawie mikrotomografii rentgenowskiej

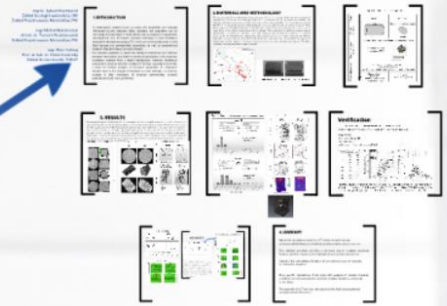

Przebieg pełzania iłu neogeńskiego z Warszawy w badaniach trójosiowych z wykorzystaniem mikrotomografii komputerowej

Prezi

Komputerowa analiza właściwości zbiornikowych przestrzeni porowej piaskowców oraz ich wytrzymałości, na podstawie mikrotomografii rentgenowskiej

mgr in. Łukasz Kaczmarek
Zakład Geologii Inynierskiej, UW
Zakład Projektowania Materiałów, PW

mgr Michał Maksimczuk
dr hab. in. Tomasz Wejrzanowski
Zakład Projektowania Materiałów, PW

mgr Zhao Yufeng
Prof. dr hab. in. Heinz Konietzky
Zakład Geomechaniki, TUBAF

1.INTRODUCTION

In heterogenic material such as rocks, the properties are strongly influenced by the structure. Both, structure and properties can be nowadays characterized in more details due to progress in equipment development. One of modern research technique is high-resolution computed-ray tomography (μCT) which can be favorably used in rock fluid storage and permeability recognition as well as geotechnical study of structure impact on rock strength.

The research question is about the utility of combining μCT internal structure recognition and further numerical calculations with regard to sandstone samples from a hybrid hydrocarbon reservoir. Numerical calculations produce detailed analyses of storage capacity and provide a basis for further analysis of transport properties. An important related issue is the impact of structure on rock strength. In order to analyze it after simulation of absolute permeability, uniaxial compression tests were performed.

2.MATERIALS AND METHODOLOGY

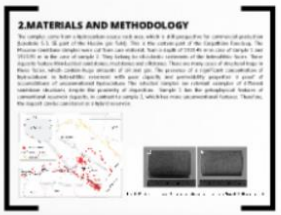

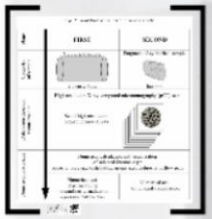

3. RESULTS

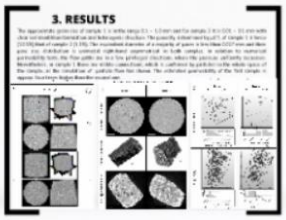

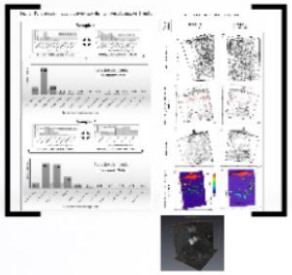

Verification

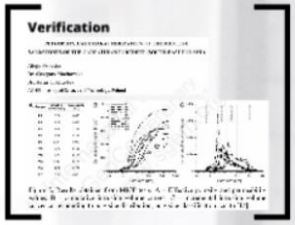

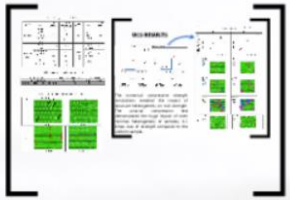

4.SUMMARY

Numerical calculations based on μCT results revealed storage and permeability features of a hybrid sandstone hydrocarbon reservoir.

The outlined procedure provides a universal way to evaluate structural features and their impact on the hydraulical and mechanical behavior.

Sample 1 has petrophysical features of conventional reservoir deposits, in contrast to sample 2.

More specific calculations of lab tests with analysis of variable boundary conditions as well as parametric and back analysis should be carried out in the future.

The potential of μCT has been extended into the field of petrophysical and geomechanical science.

Prezi

1.INTRODUCTION

In heterogenic material such as rocks, the properties are strongly influenced by the structure. Both, structure and properties can be nowadays characterized in more details due to progress in equipment development. One of modern research technique is high-resolution computed microtomography (μCT) which can be favorably used in rock fluid storage and permeability recognition as well as geotechnical study of structure impact on rock strength.

The research question is about the utility of combining μCT internal structure recognition and further numerical calculations with regard to sandstone samples from a hybrid hydrocarbon reservoir. Numerical calculations produce detailed analyses of storage capacity and provide a basis for further analysis of transport properties. An important related issue is the impact of structure on rock strength. In order to analyze it after simulation of absolute permeability, uniaxial compression tests were performed.

2.MATERIALS AND METHODOLOGY

The samples come from a hydrocarbon source rock area, which is still prospective for commercial production (borehole S-3, SE part of the Husów gas field). This is the eastern part of the Carpathian Foredeep. The Miocene sandstone samples were cut from core material, from a depth of 1920.45 m in case of sample 1 and 1923.95 m in the case of sample 2. They belong to siliciclastic sediments of the heterolithic facies. These deposits feature thin-bedded sandstones, mudstones and siltstones. There are many cases of structural traps in these facies, which contain huge amounts of oil and gas. The presence of a significant concentration of hydrocarbons in heterolithic reservoirs with poor capacity and permeability properties is proof of accumulations of unconventional hydrocarbon. The selected samples are relevant examples of different sandstone structures, despite the proximity of deposition. Sample 1 has the petrophysical features of conventional reservoir deposits, in contrast to sample 2, which has more unconventional features. Therefore, the deposit can be considered as a hybrid reservoir.

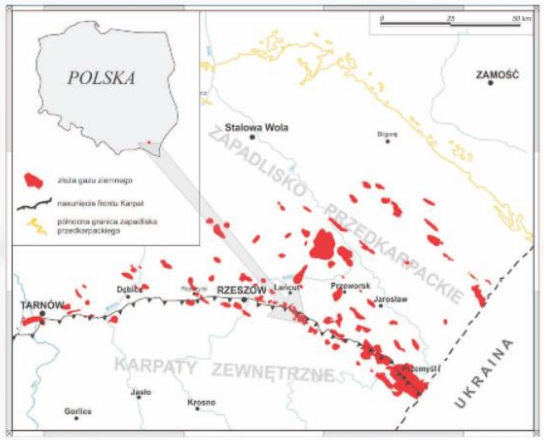

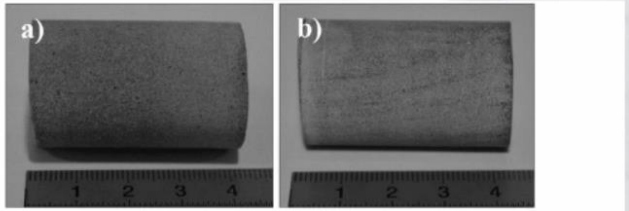

Fig. 1. Photos of analyzed Miocene sandstone samples: A – Sample 1, B – Sample 2

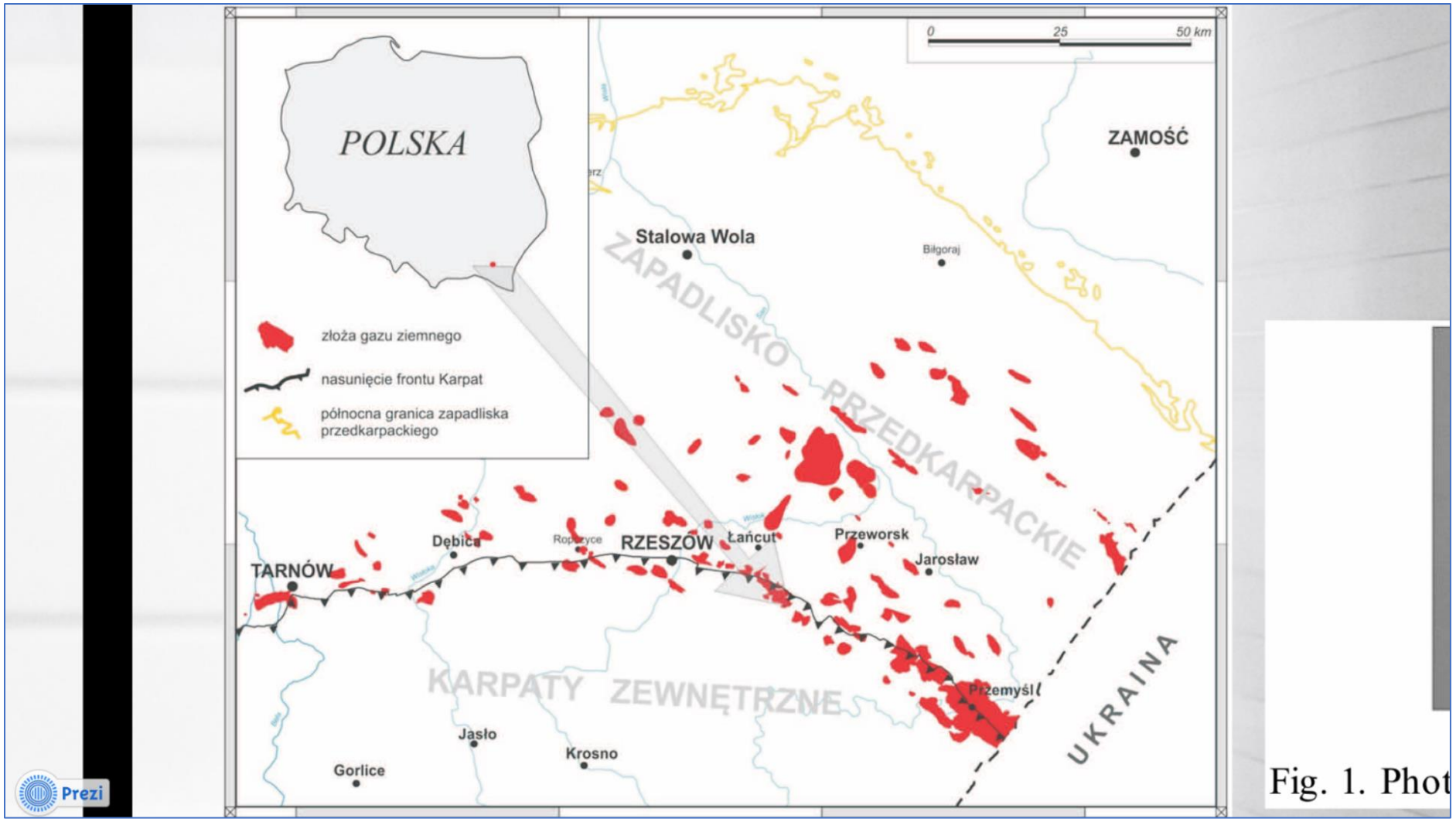
POLSKA
złoża gazu ziemnego
nasunięcie frontu Karpat
północna granica zapadliska przedkarpackiego
0
25
50 km
ZAMOŚĆ
Stalowa Wola
Biłgoraj
ZAPADLISKO PRZEDKARPACKIE
TARNÓW
Dębica
Ropczyce
RZESZÓW
Łańcut
Przeworsk
Jarosław
KARPATY ZEWNĘTRZNE
Przemyśl
UKRAINA
Jasło
Krosno
Gorlice
Prezi

Fig. 1. Phot

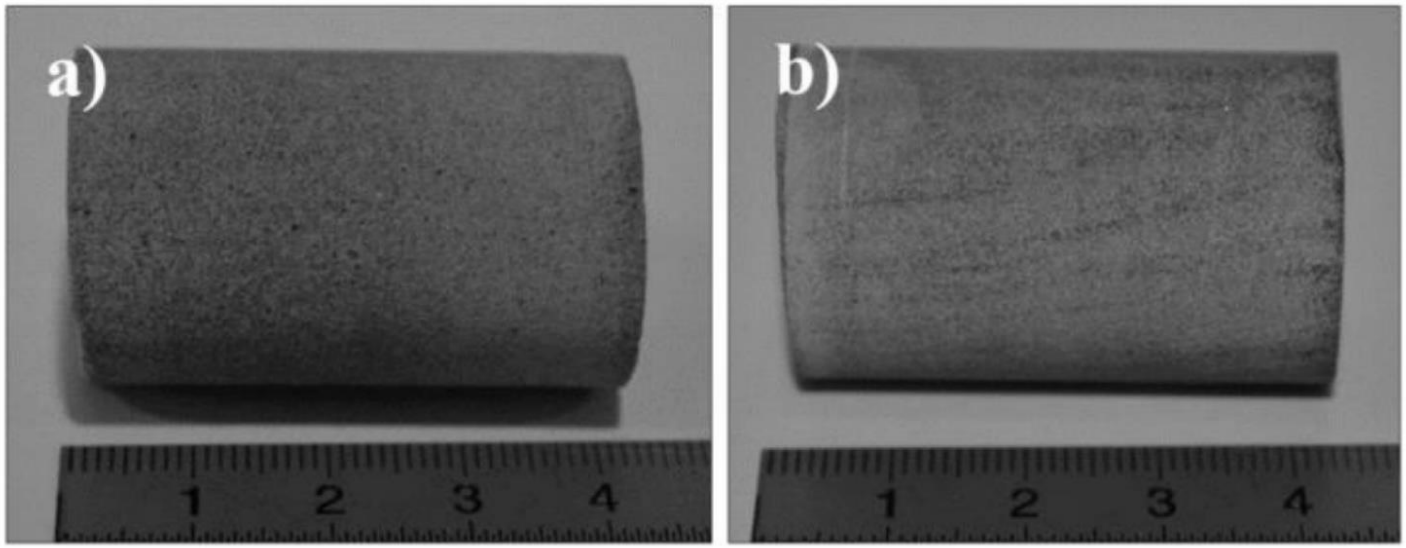

Fig. 1. Photos of analyzed Miocene sandstone samples: A – Sample 1, B – Sample 2

Prezi

Fig. 2. Workflow of sandstone sample study

Stage	FIRST	SECOND
Geometry of sample	Cylindrical sample 2.5 cm x 4 cm	Fragment of cylindrical sample 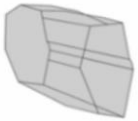 few mm
Data acquisition and reconstruction	High-resolution X-ray computed microtomography (µCT) scan	
	Set of high-resolution bitmap images (1024) 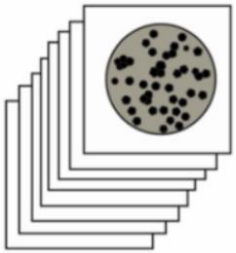	
Numerical processing	Numerical calculation and visualization of selected features e.g.: porosity, pore size distribution, grains size, tortuosity of flow path	
	Numerical test of permeability - streamlines visualization - pressure distribution	Numerical test of uniaxial compression

Prezi

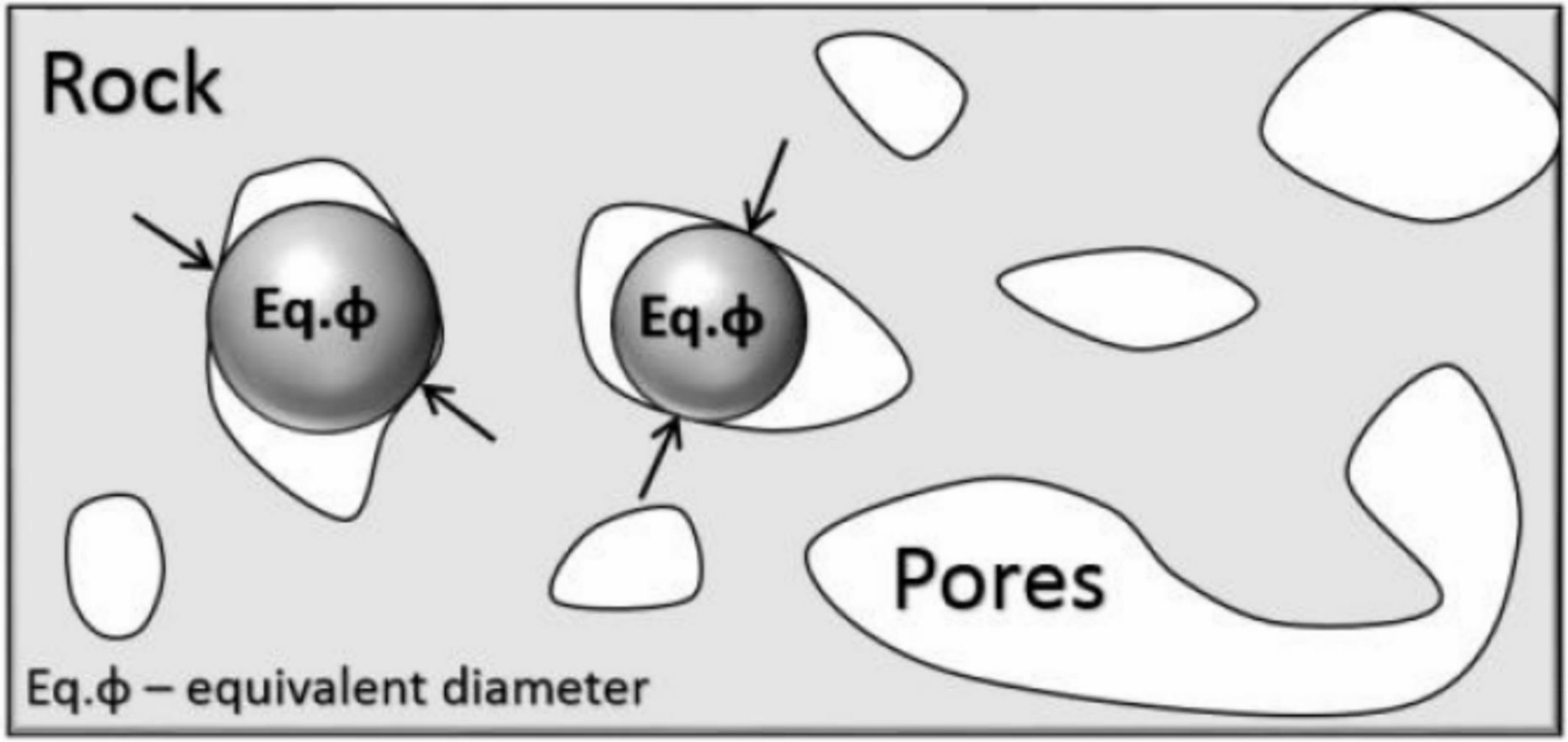

Fig. 3. Scheme the equivalent diameter

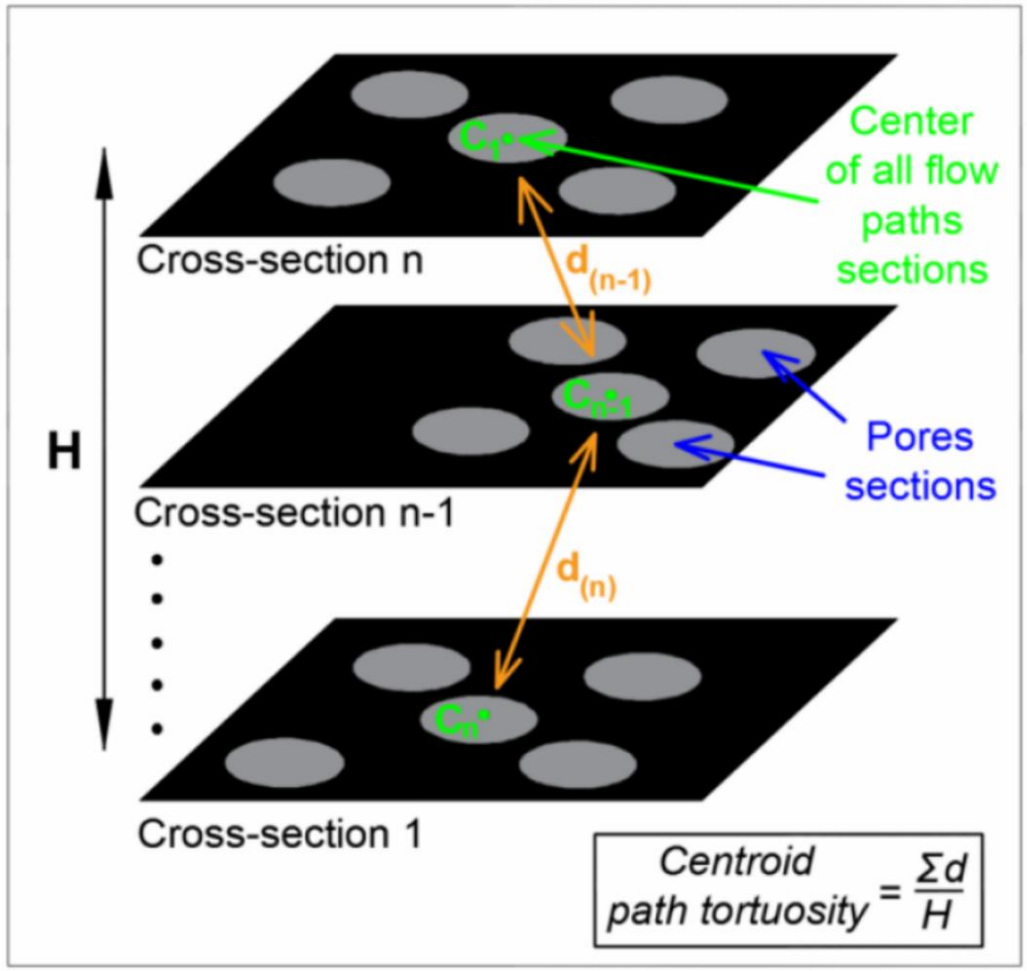

Fig. 4. Schematic diagram of centroid path tortuosity calculation

3. RESULTS

The approximate grain size of sample 1 is in the range 0.1 – 1.0 mm and for sample 2 it is 0.01 – 0.1 mm with clear sedimentation lamination and heterogenic structure. The porosity, determined by µCT, of sample 1 is twice (10.3%) that of sample 2 (5.3%). The equivalent diameter of a majority of pores is less than 0.027 mm and their pore size distribution is unimodal right-hand asymmetrical in both samples. In relation to numerical permeability tests, the flow paths are in a few privileged directions, where the pressure uniformly decreases. Nevertheless, in sample 1 there are visible connections, which is confirmed by particles in the whole space of the sample, as the simulation of particle flow has shown. The estimated permeability of the first sample is approx. four times higher than the second one.

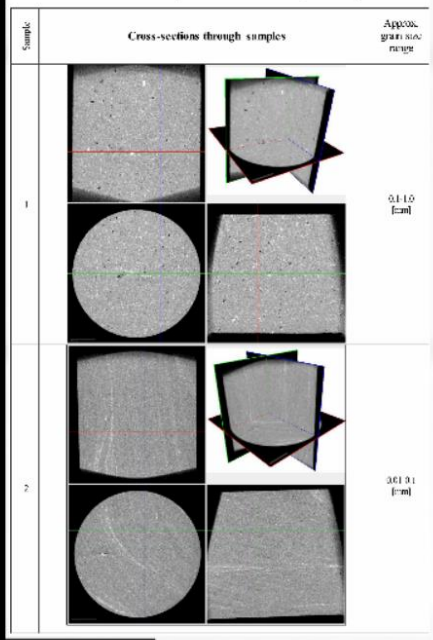

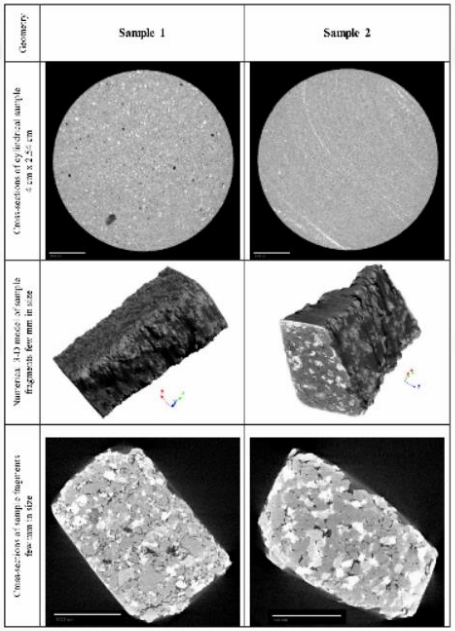

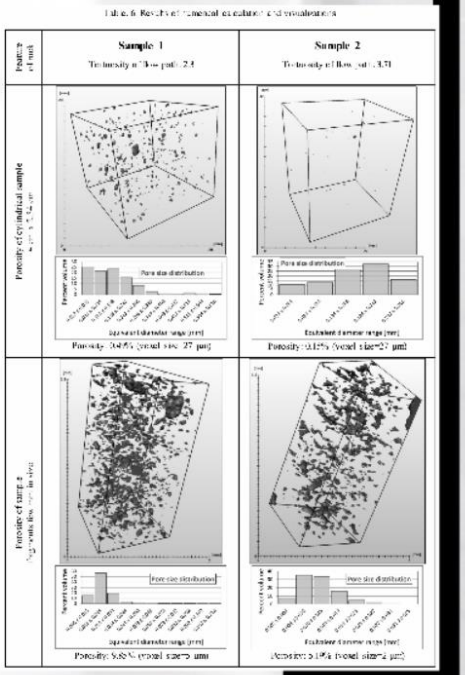

Table. 4. Results of data acquisition and reconstruction of cylindrical samples

Sample	Cross-sections through samples	Approx. grain size range
1		0.1-1.0 [mm]
2		0.01-0.1 [mm]

Table. 5. Resu

Geometry	Sa
Cross-sections of cylindrical sample 4 cm x 2.54 cm	
Numerical 3-D model of sample fragments few mm in size	
Cross-sections of sample fragments few mm in size	

ylindrical samples

Table. 5. Results of data acquisition and reconstruction: structure comparison

	Approx. grain size range	Geometry	Sample 1	Sample 2
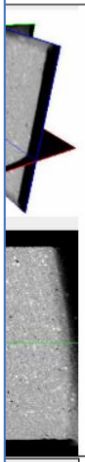	0.1-1.0 [mm]	Cross-sections of cylindrical sample 4 cm x 2.54 cm	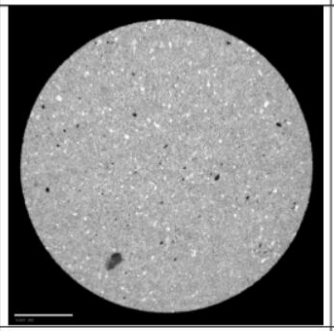	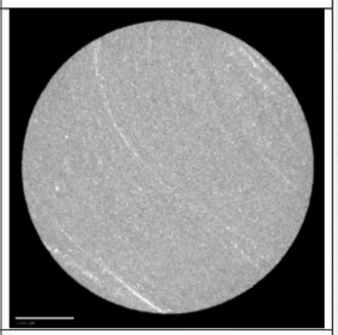
		Numerical 3-D model of sample fragments few mm in size	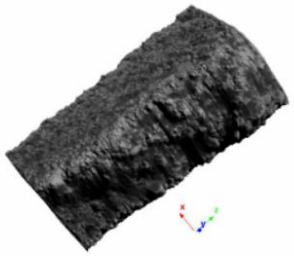	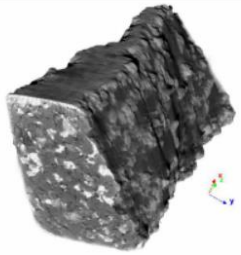
	0.01-0.1 [mm]	Cross-sections of sample fragments few mm in size	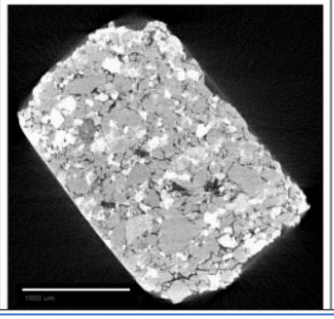	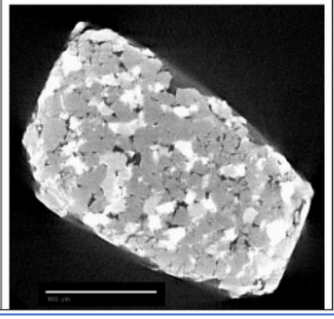

Feature of rock	Sam
	Tortuosity of
Porosity of cylindrical sample 4 cm x 2.54 cm	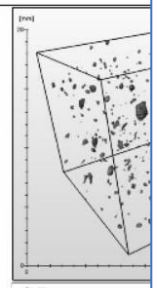 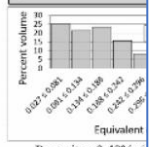 Porosity: 0.49% (
Porosity of sample fragments few mm in size	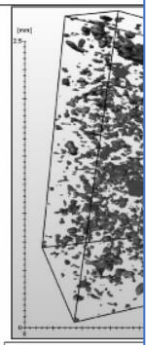 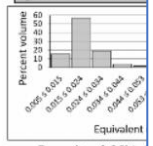 Porosity: 9.85% (

tructure comparison

Sample 2

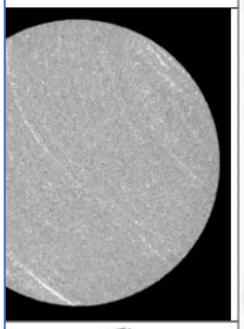

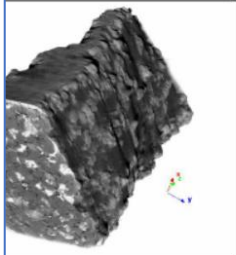

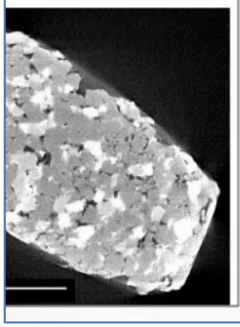

Table. 6. Results of numerical calculation and visualizations

Feature of rock	**Sample 1** Tortuosity of flow path: 2.3	**Sample 2** Tortuosity of flow path: 3.71
Porosity of cylindrical sample 4 cm x 2.54 cm	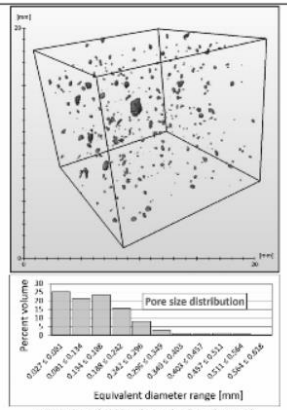 Porosity: 0.49% (voxel size=27 μm)	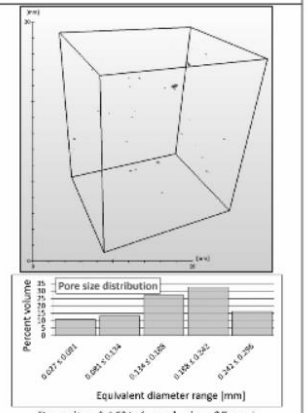 Porosity: 0.15% (voxel size=27 μm)
Porosity of sample fragments few mm in size	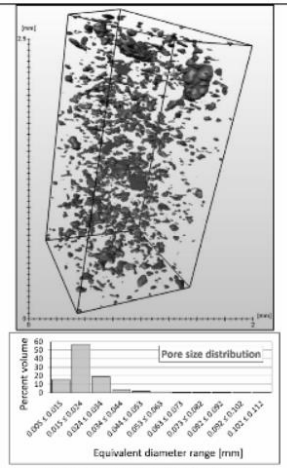 Porosity: 9.85% (voxel size 5 μm)	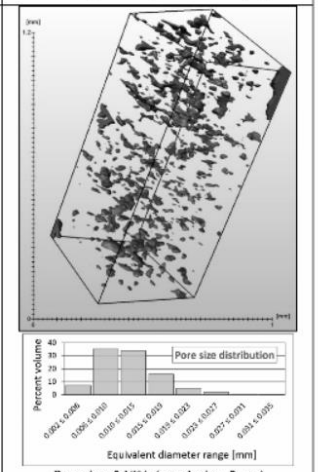 Porosity: 5.19% (voxel size 2 μm)

Fig. 5. Total porosity and full pore size distribution of samples 1 and 2

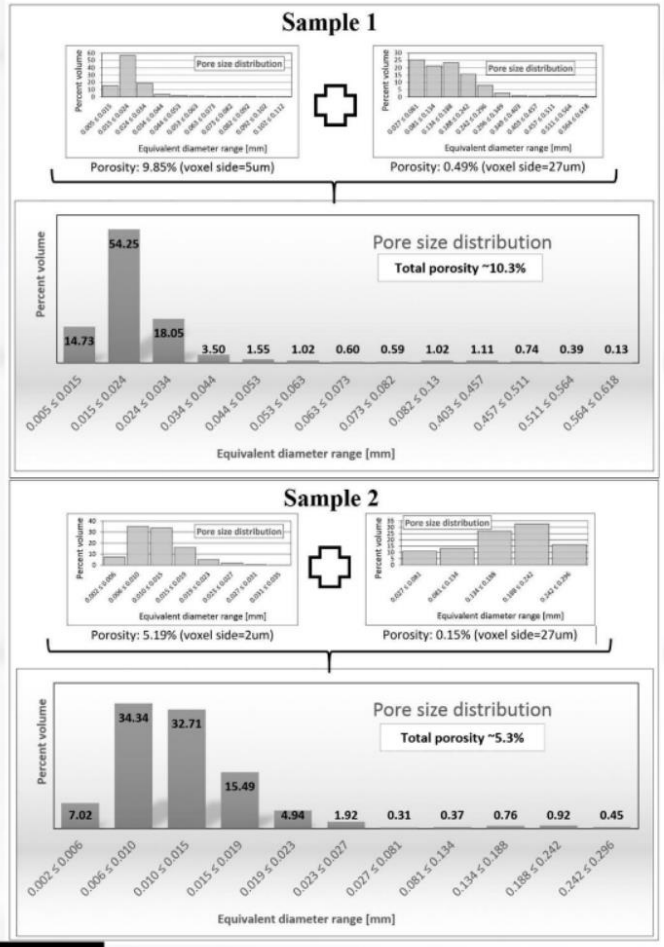

Table. 7. Results of numerical permeability testing

Feature of rock	Sample 1 k = 2.72 md	Sample 2 k = 0.65 md
Connectivity of pores	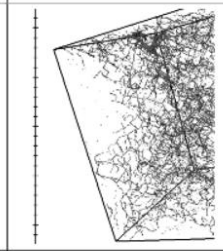	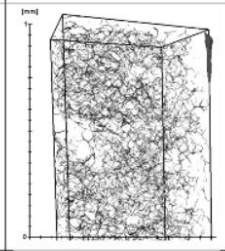
Permeability streamlines and their vectors	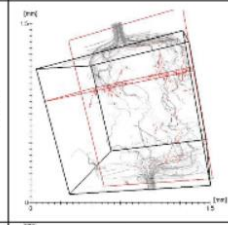	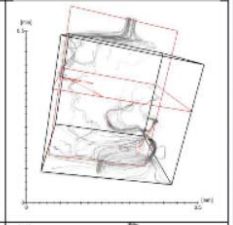
Particle flow	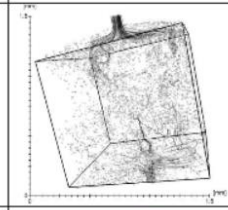	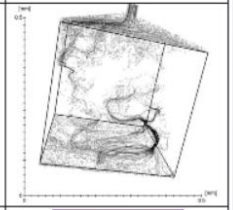
Pressure distribution in the region of interest	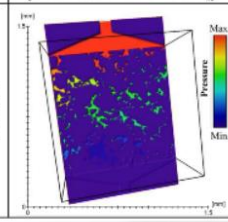	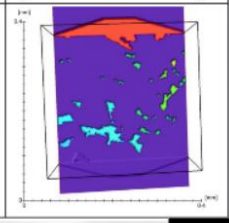

Fig. 5. Total porosity and full pore size distribution of samples 1 and 2

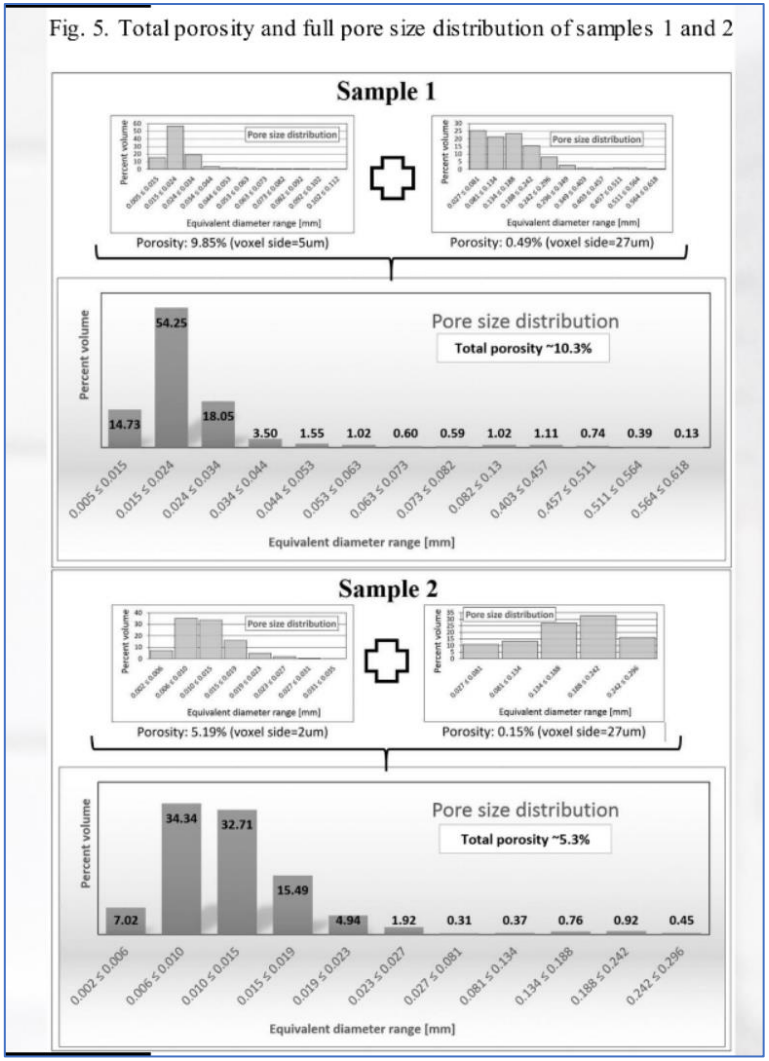

Table. 7. Results of numerical permeability testing

Feature of rock	**Sample 1** k = 2.72 md	**Sample 2** k = 0.65 md
Connectivity of pores	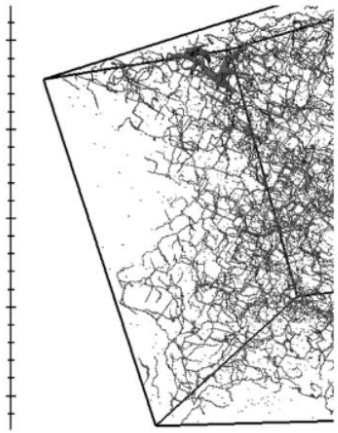	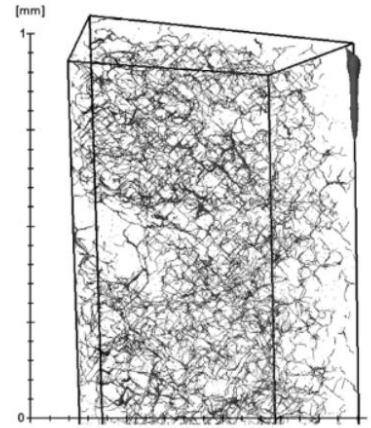
Permeability streamlines and their vectors	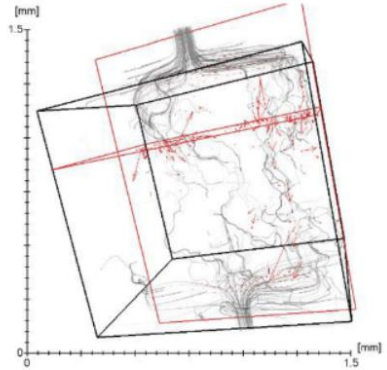	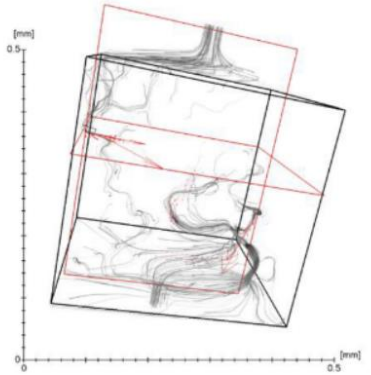

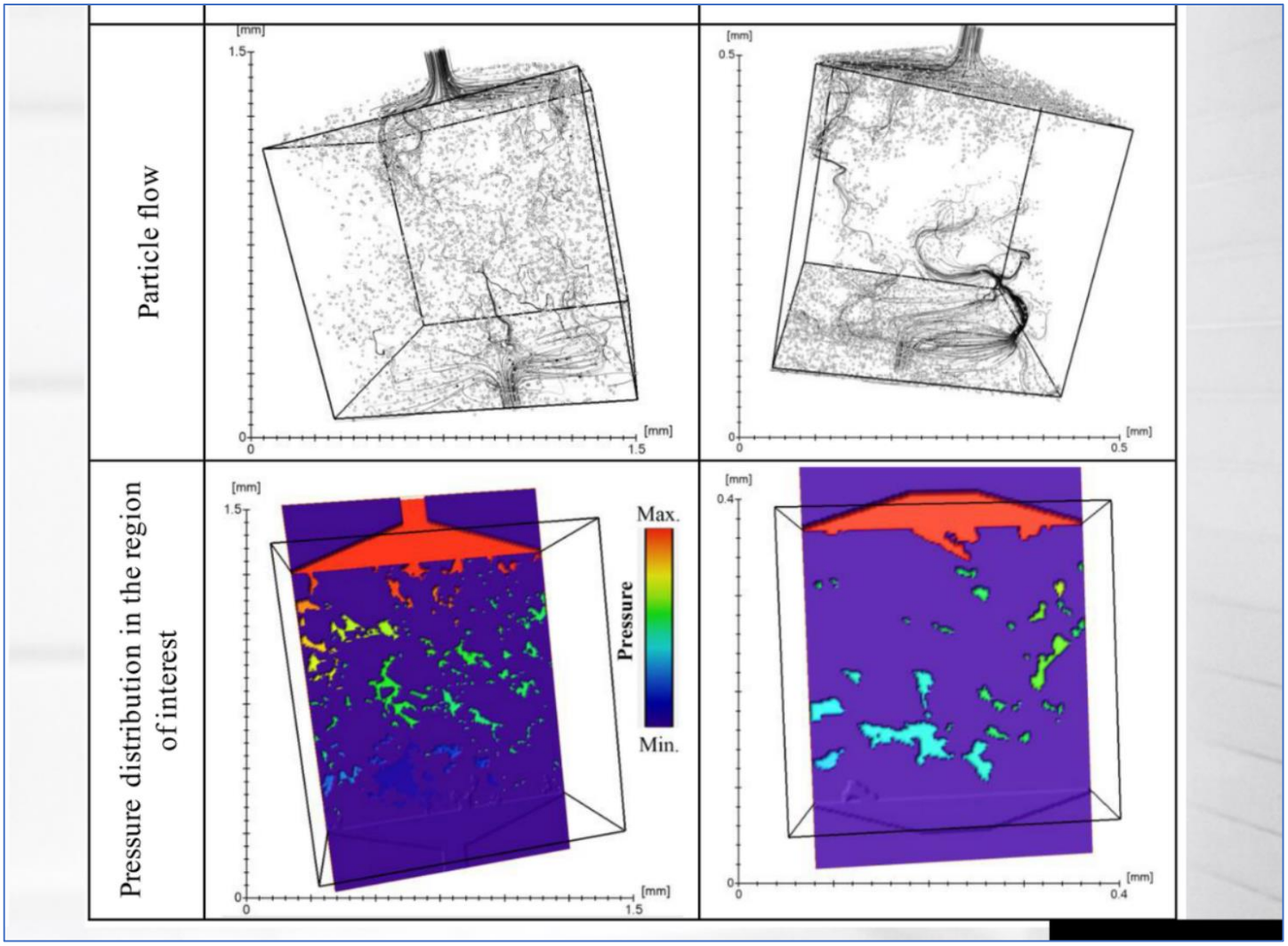
Particle flow
Pressure distribution in the region of interest
[mm]
1.5
0
[mm]
1.5
0.5
0.4
Max.
Pressure
Min.

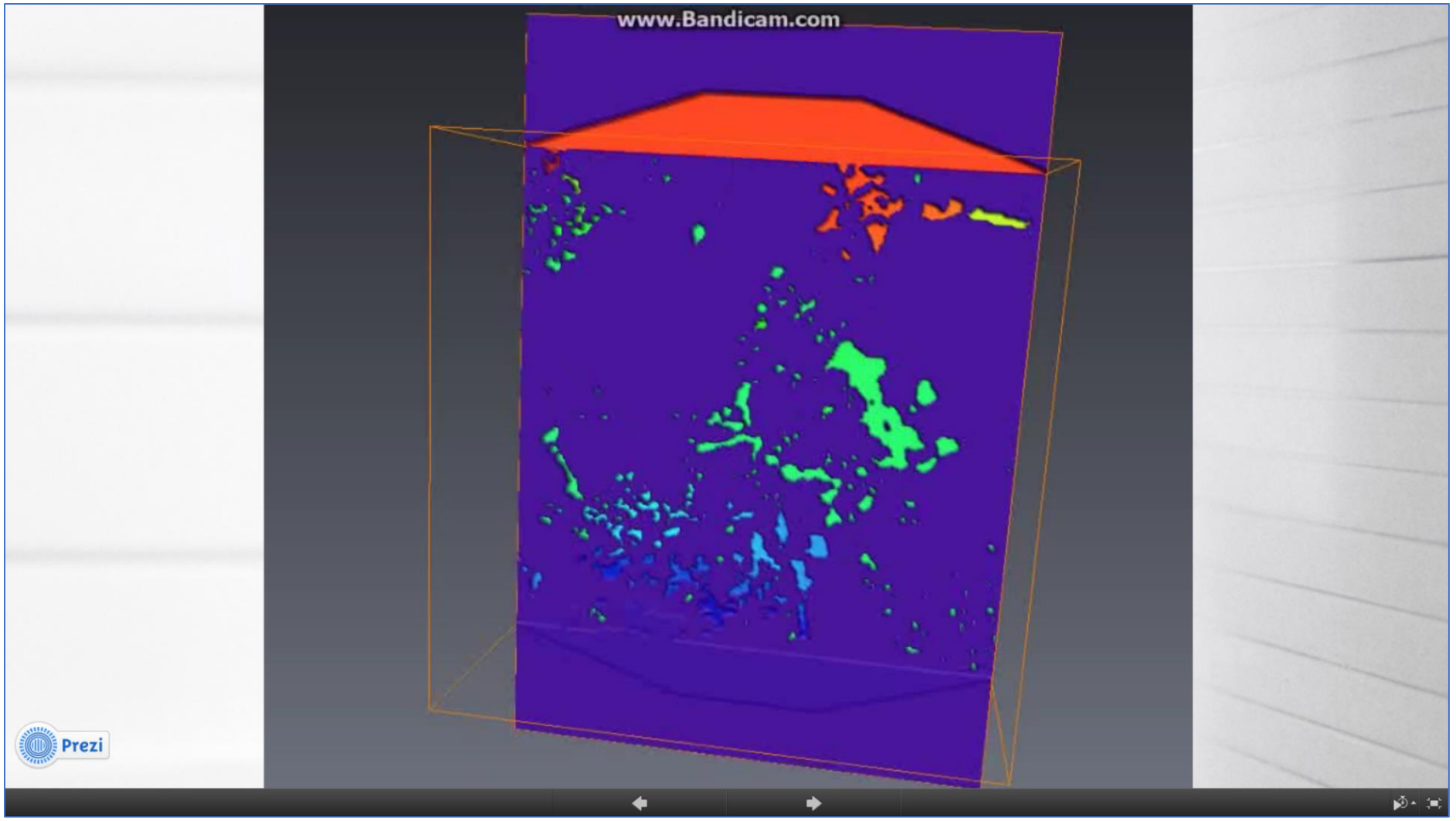
www.Bandicam.com
Prezi

Verification

PETROPHYSICAL CHARACTERIZATION OF THE MIOCENE SANDSTONES OF THE CARPATHIAN FOREDEEP (SOUTH-EAST POLAND)

Alicja Pstrucha

Dr. Grzegorz Machowski

Dr. Artur T. Krzyżak

AGH University of Science and Technology, **Poland**

A

Sample	Effective porosity [%]	Permeability [mD]
P1	13.74	0.423
P4	11.07	0.877
P6	12.48	1.789
P7	18.38	2.755
P9	8.76	0.077
P10	10.78	0.135
P13	10.70	0.131
P15	6.90	0.125
P16	14.52	0.207
P17	15.24	0.061

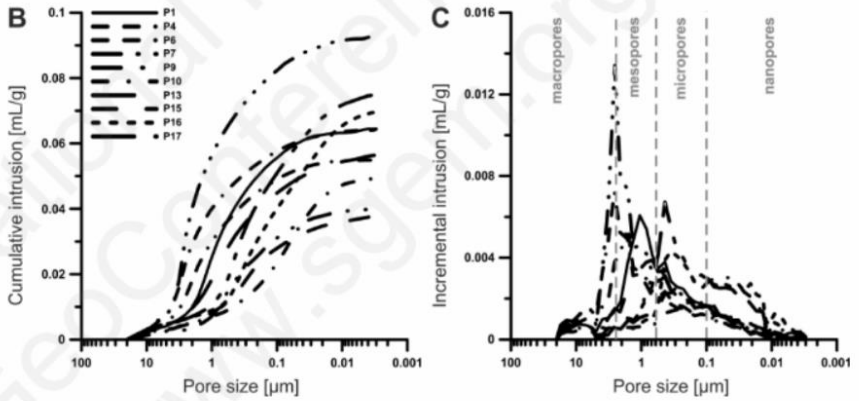

Figure 2. Results obtained from MICP tests: A – Effective porosity and permeability values; B – cumulative intrusion volume curves; C – incremental intrusion volume curves corresponding to pore size distribution; pore size classification acc. to [12].

AGH University of Science and Technology, **Poland**

A

Sample	Effective porosity [%]	Permeability [mD]
P1	13.74	0.423
P4	11.07	0.877
P6	12.48	1.789
P7	18.38	2.755
P9	8.76	0.077
P10	10.78	0.135
P13	10.70	0.131
P15	6.90	0.125
P16	14.52	0.207
P17	15.24	0.061

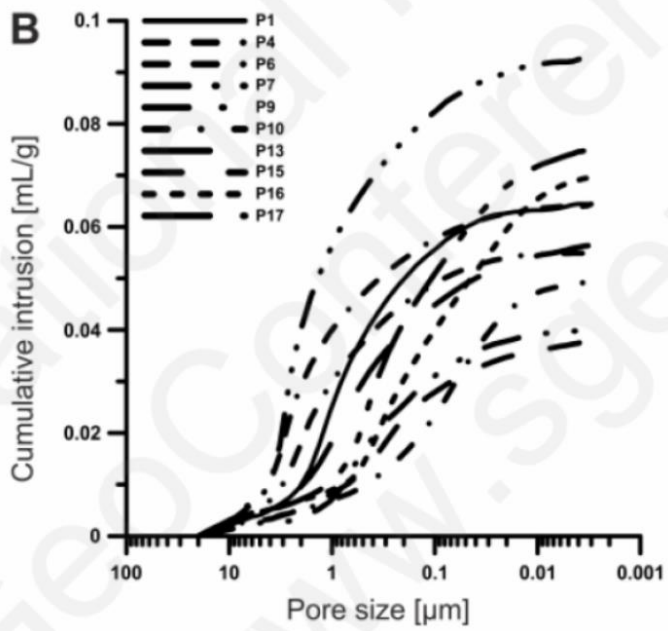

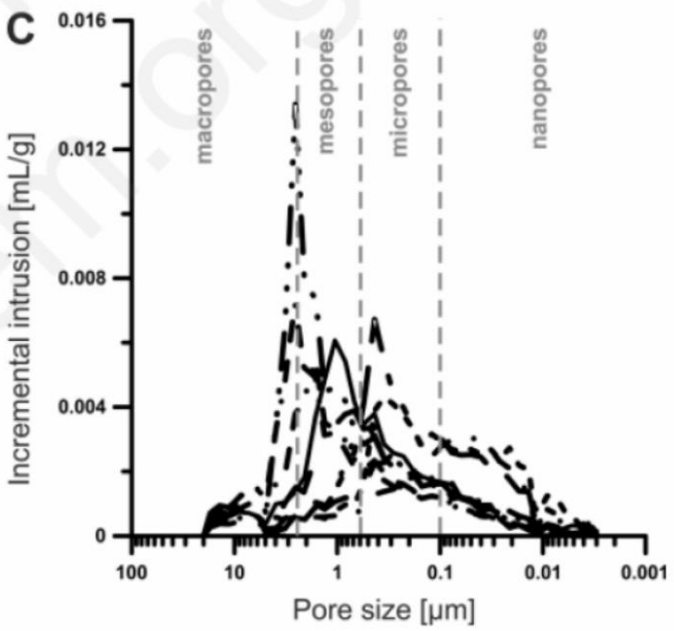

Figure 2. Results obtained from MICP tests: A – Effective porosity and permeability values; B – cumulative intrusion volume curves; C – incremental intrusion volume curves corresponding to pore size distribution; pore size classification acc. to [12].

Table 1. Model parameters in 2D simulation

Model Element	Parameter	Rock matrix (sandstone)	Lamination (small grains of quartzite)	Model Element	Parameter	Loading plates (wall)
Particles	Radius r [mm]	0.05	0.05	walls	Effective modulus E [MPa]	8×10^3
	Density ρ [kg/m^3]	2500	2700			
	Effective modulus E [MPa]	8×10^3	8×10^3			
Flat-joint contact (ball-ball)	Effective modulus E_c [MPa]	1.06×10^4	3.69×10^4	Linear model (ball-facet)	Normal stiffness k_n [GPa/m]	21.2
	Tension strength σ_c [MPa]	2.28	0.29		Shear stiffness k_s [GPa/m]	21.2
	Cohesion c [MPa]	1.69	15.35			
	Friction coefficient μ	0.5	0.5		Friction coefficient β	0.05
	Friction angle ϕ [°]	43.83	47.82			

Table 2. Numbers of particles in each model

Number of particles N	Model 1-1	Model 1-2	Model 2-1	Model 2-2
Rock matrix (sandstone)	58918	59250	59136	61440
Lamination(small grains of quartzite)	0	0	2304	0

Table. 3. Calculation model employee during the UCS tests

Sample	Original group	Control group
1	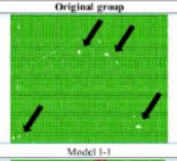 Model 1-1	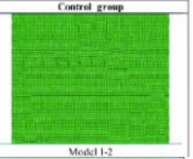 Model 1-2
2	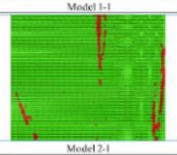 Model 2-1	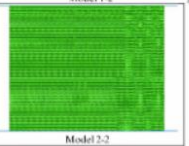 Model 2-2

UCS RESULTS

Fig. 6. Stress-strain curved obtained from numerical UCS tests

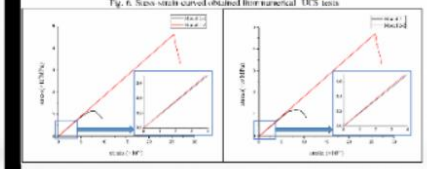

Table. 8. Uniaxial compressive strength of rock models

Model 1-1	Model 1-2	Model 2-1	Model 2-2
1.15×10^7MPa	4.64×10^6MPa	1.21×10^7MPa	4.76×10^6MPa

The numerical compressive strength simulations revealed the impact of structure heterogeneity on rock strength. The uniaxial compression test demonstrated the huge impact of even minimal heterogeneity of samples, 4-5 times loss of strength compared to the uniform sample.

Table. 9. Stress-strain curves obtained from numerical UCS tests with marked points representing different moments of stress field

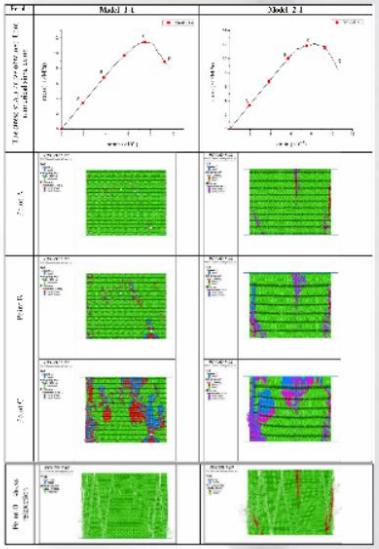

Prezi

Table 1. Model parameters in 2D simulation

Model Element	Parameter	Rock matrix (sandstone)	Lamination (small grains of quartzite)	Model Element	Parameter	Loading plates (wall)
Particles	Radius r [mm]	0.05	0.05	**walls**	Effective modulus E [MPa]	8×10^2
	Density ρ [kg/m^3]	2500	2700			
	Effective modulus E [MPa]	8×10^2	8×10^2			
Flat-joint contact (ball-ball)	Effective modulus E_{fj} [MPa]	1.06×10^4	3.69×10^3	**Linear model (ball-facet)**	Normal stiffness k_n [GPa/m]	21.2
	Tension strength σ_c [MPa]	2.28	0.29		Shear stiffness k_s [GPa/m]	21.2
	Cohesion c [MPa]	1.69	15.35			
	Friction coefficient μ	0.5	0.5		Friction coefficient μ	0.05
	Friction angle ϕ [°]	43.83	47.82			

Table 2. Numbers of particles in each model

Number of particles N	Model 1-1	Model 1-2	Model 2-1	Model 2-2
Rock matrix (sandstone)	58918	59250	59136	61440
Lamination(small grains of quartzite)	0	0	2304	0

Table. 3. Calculation model employee during the UCS tests

Sample	Original group	Control group
1	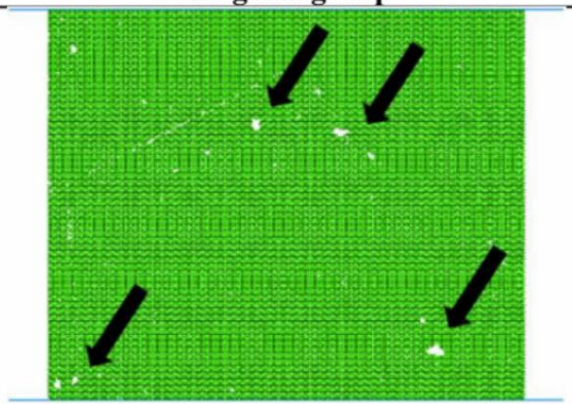 Model 1-1	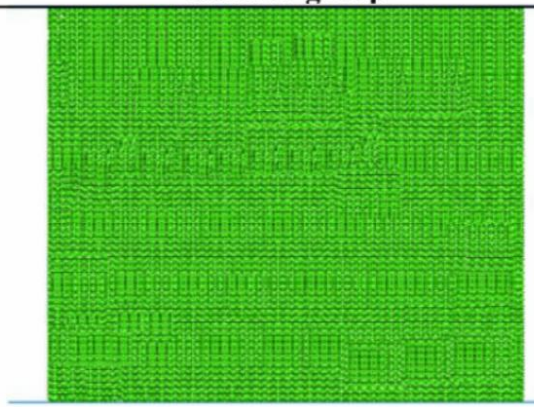 Model 1-2
2	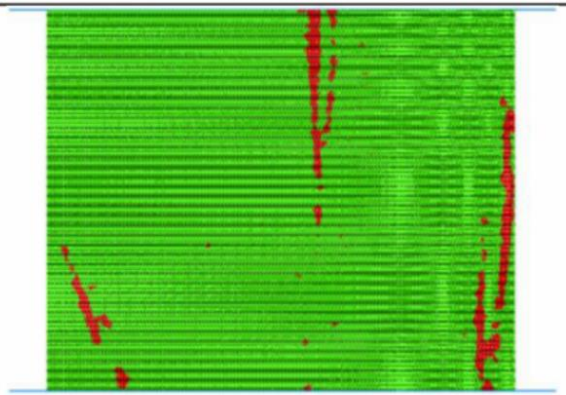 Model 2-1	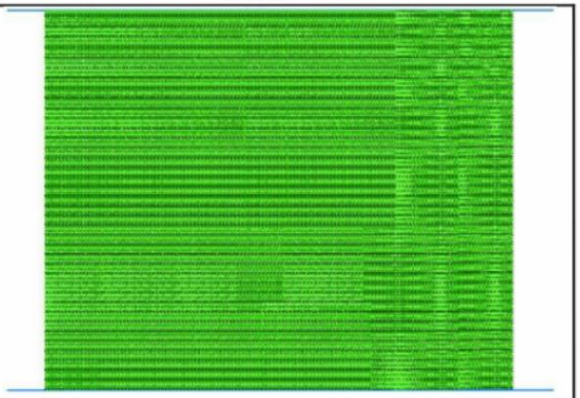 Model 2-2

UCS RESULTS

Fig. 6. Stess-strain-curved obtained from numerical UCS tests

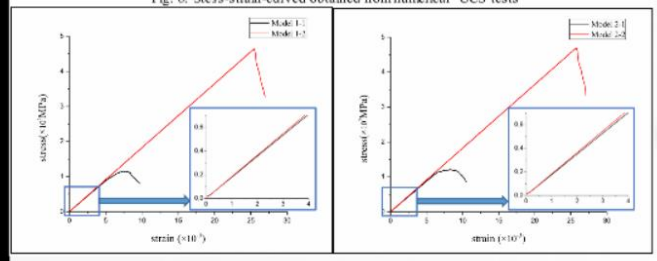

Table. 8. Uniaxial compressive strength of rock models

Model 1-1	Model 1-2	Model 2-1	Model 2-2
1.15×10^2MPa	4.64×10^2MPa	1.21×10^2MPa	4.70×10^2MPa

The numerical compressive strength simulations revealed the impact of structure heterogeneity on rock strength. The uniaxial compression test demonstrated the huge impact of even minimal heterogeneity of samples, 4-5 times loss of strength compared to the uniform sample.

Table. 9. Stress-strain curves obtained from numerical UCS tests with marked points representing different moments of stress field

Results	Model 1-1	Model 2-1
The stress-strain curve obtained from numerical simulation	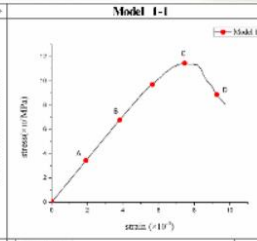	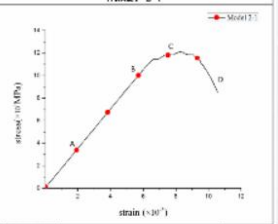
Point A		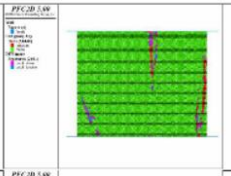
Point B	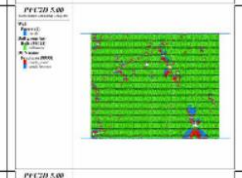	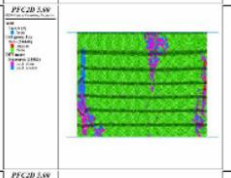
Point C	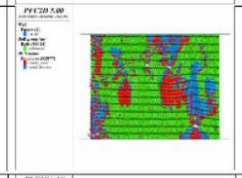	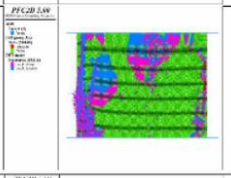
Point D – stress relaxation		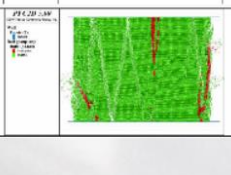

Fig. 6. Stess-strain-curved obtained from numerical UCS tests

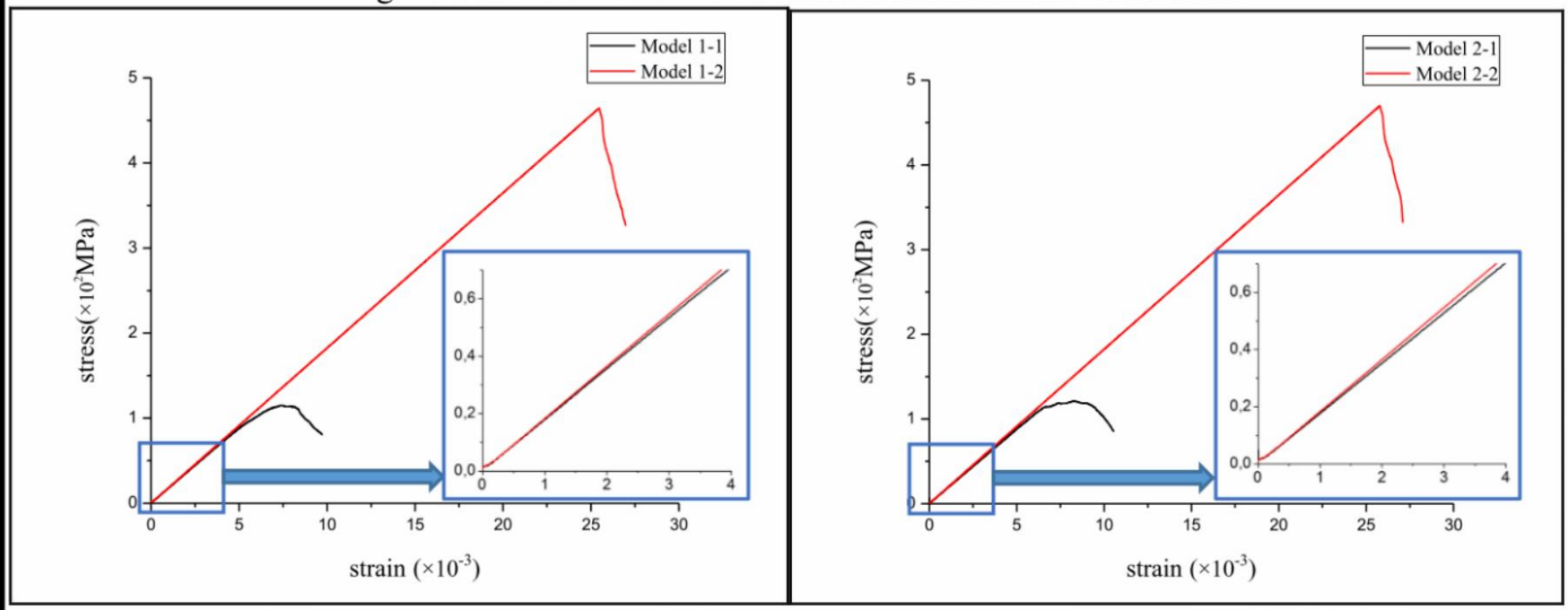

Table. 8. Uniaxial compressive strength of rock models

Model 1-1	Model 1-2	Model 2-1	Model 2-2
1.15×10^2MPa	4.64×10^2MPa	1.21×10^2MPa	4.70×10^2MPa

Prezi

Table. 9. Stress-strain curves obtained from numerical UCS tests with marked points representing different moments of stress field

Results	Model 1-1	Model 2-1
The stress-strain curve obtained from numerical simulation	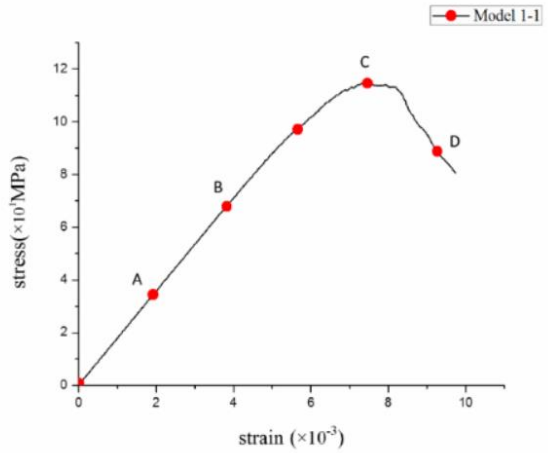	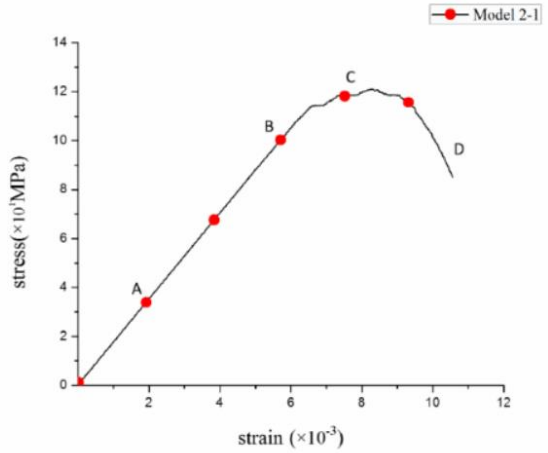
Point A	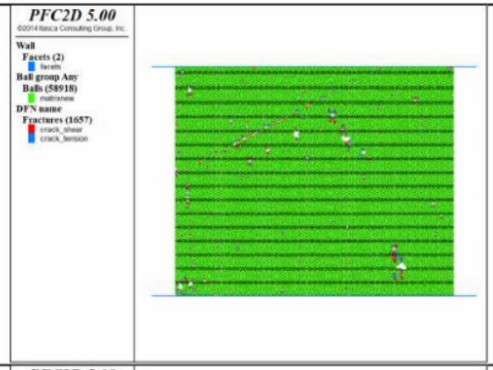	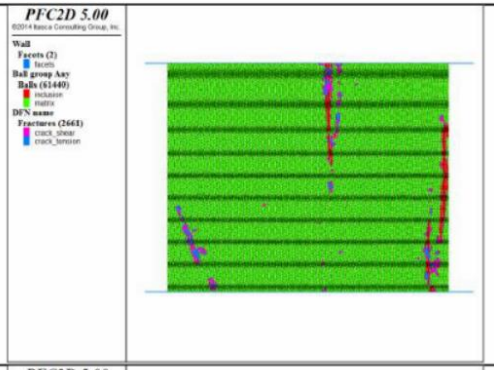

Point B	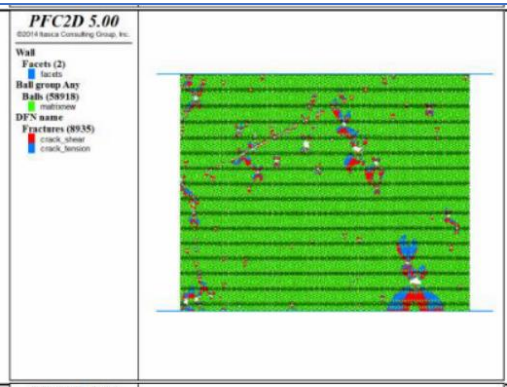	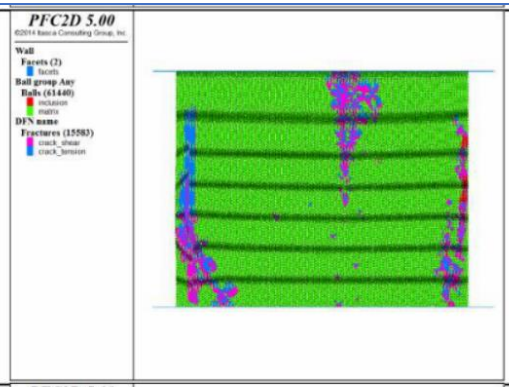
Point C	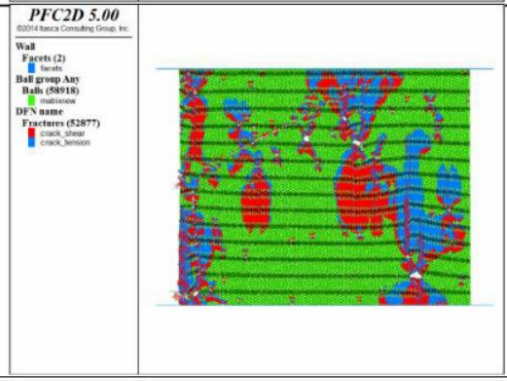	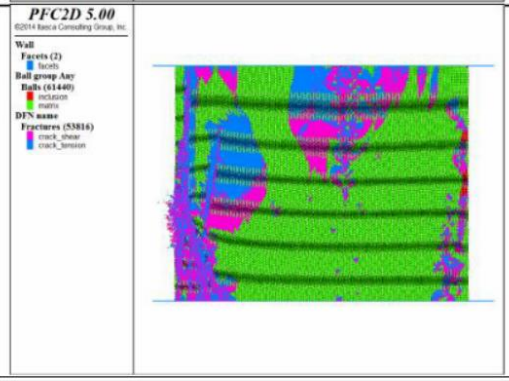
Point D – stress relaxation	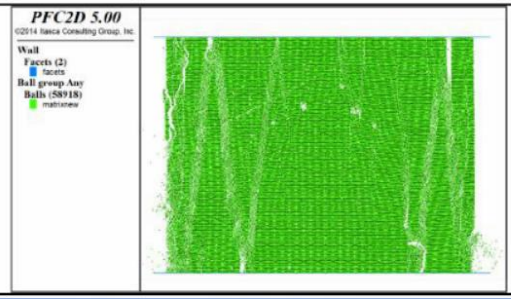	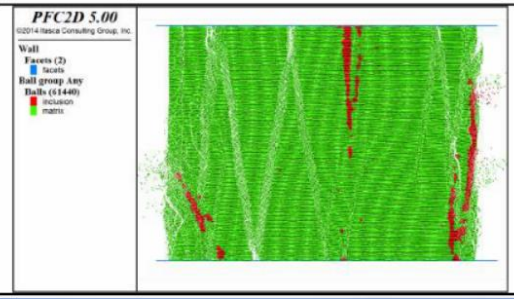

4.SUMMARY

Numerical calculations based on µCT results revealed storage and permeability features of a hybrid sandstone hydrocarbon reservoir.

The outlined procedure provides a universal way to evaluate structural features and their impact on the hydraulical and mechanical behavior.

Sample 1 has petrophysical features of conventional reservoir deposits, in contrast to sample 2.

More specific calculations of lab tests with analysis of variable boundary conditions as well as parametric and back analysis should be carried out in the future.

The potential of µCT has been extended into the field of petrophysical and geomechanical science.

Prezi

fii w geoinżynierii:
'skiej

Warszawa, 20.04.2017

ZASTOSOWANIE W PRAKTYCE

Komputerowa analiza właściwości zbiornikowych przestrzeni porowej piaskowców oraz ich wytrzymałości, na podstawie mikrotomografii rentgenowskiej

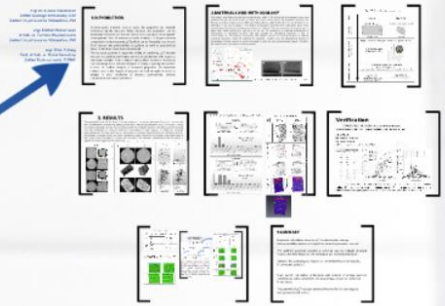

Przebieg pełzania iłu neogeńskiego z Warszawy w badaniach trójosiowych z wykorzystaniem mikrotomografii komputerowej

Prezi

Przebieg pełzania iłu neogeńskiego z Warszawy w badaniach trójosiowych z wykorzystaniem mikrotomografii komputerowej

1. INTRODUCTION

Investigating creep is fundamental for practical issues, such as assessing the stability of slopes on hills and embankments which are in a constant stress state. In order to recreate the real three-dimensional stress state and strain field, triaxial tests were applied in the present study.

The research question in this study concerns the course of strain changes during constant stress state resulting in creep soil deformation. Therefore, three multistage (multistress levels) triaxial creep tests were performed. Axial and radial strains measuring sensors were used to determine the full characteristics of soil behavior during the triaxial tests. Neogene clay was used in the study, due to its prevalence in construction sites in Warsaw. In respect of undisturbed cohesive soil with strong glacial tectonic involvement history we expect structure heterogeneity, micro cracks and even empty voids. For non-invasive and non-destructive internal structure recognition, X-ray computed microtomography (XμCT) was applied.

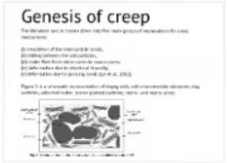

3. MATERIAL

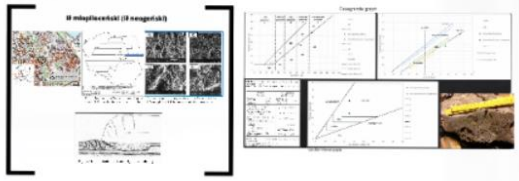

2. METHODOLOGY

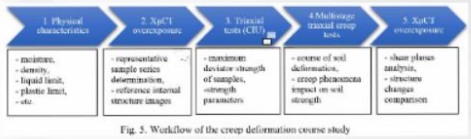

Fig. 5. Workflow of the creep deformation course study

4. RESULTS

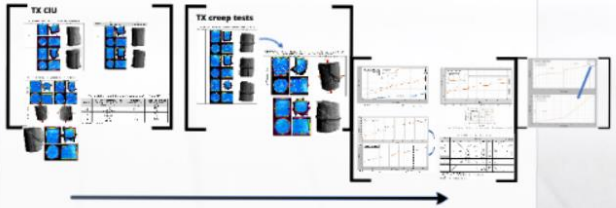

5. SUMMARY

The study identified the rheological strain course, which can be broken down into three characterizations: decreasing creep strain rate, transitional constant creep velocity, and accelerating creep deformation.

The study found that due to multistage creep loading, the samples were strengthened. Furthermore, there is a visibly "brittle" character of failure, which can be the consequence of redistribution of the microstructure as a function of time as well as collapse of voids. Due to the glacial tectonic of the analyzed samples, the reactivation of micro cracks might also serve as an explanation. The number of the various sizes of shear planes after failure is confirmed by XμCT overexposure.

More detailed summary →

Prezi

1. INTRODUCTION

Investigating creep is fundamental for practical issues, such as assessing the stability of slopes on hills and embankments which are in a constant stress state. In order to recreate the real three-dimensional stress state and strain field, triaxial tests were applied in the present study.

The research question in this study concerns the course of strain changes during constant stress state resulting in creep soil deformation. Therefore, three multistage (multistress levels) triaxial creep tests were performed. Axial and radial strains measuring sensors were used to determine the full characteristics of soil behavior during the triaxial tests. Neogene clay was used in the study, due to its prevalence in construction sites in Warsaw. In respect of undisturbed cohesive soil with strong glacial tectonic involvement history we expect structure heterogeneity, micro cracks and even empty voids. For non-invasive and non-destructive internal structure recognition, X-ray computed microtomography (XμCT) was applied.

Genesis of creep

The literature can be broken down into five main groups of explanations for creep mechanisms:

(i) breakdown of the interparticle bonds,
(ii) sliding between the soil particles,
(iii) water flow from micro-pores to macro-pores,
(iv) deformation due to structural viscosity,
(v) deformation due to jumping bonds (Le et al., 2012).

Figure 2 is a schematic representation of clayey soils, with characteristic elements: clay particles, adsorbed water, coarse grained particles, micro- and macro-pores.

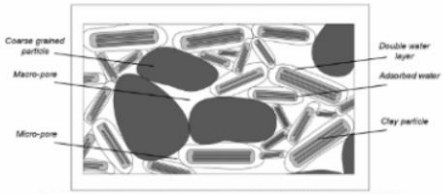

Fig. 2. Schematic view of clay-water system (modified after Lee et al., 2012)

Prezi

Genesis of creep

The literature can be broken down into five main groups of explanations for creep mechanisms:

(i) breakdown of the interparticle bonds,
(ii) sliding between the soil particles,
(iii) water flow from micro-pores to macro-pores,
(iv) deformation due to structural viscosity,
(v) deformation due to jumping bonds (Le et al., 2012).

Figure 2 is a schematic representation of clayey soils, with characteristic elements: clay particles, adsorbed water, coarse grained particles, micro- and macro-pores.

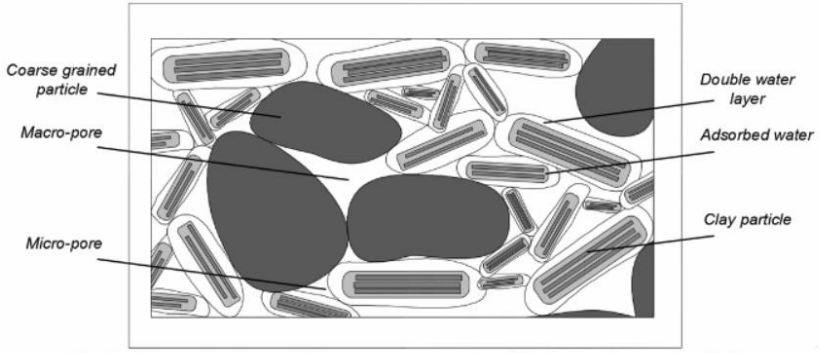

Fig. 2. Schematic view of clay-water system (modified after Lee et al., 2012)

3. MATERIAL

Ił mioplioceński (ił neogeński)

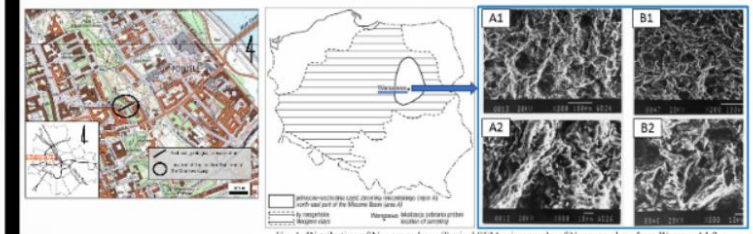

Fig. 1. Distribution of Neogene clays; Typical SEM micrographs of Neogene clays from Warsaw A1,2 - sample STG5, matrix-turbulent microstructure; B1,2 - sample STG11, laminar-turbulent microstructure

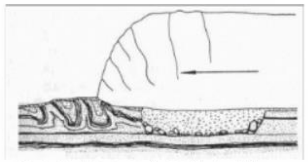

Fig. 2. Glacial tectonic; front of glacier folding

Casagrande graph

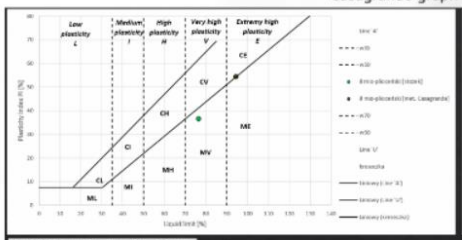

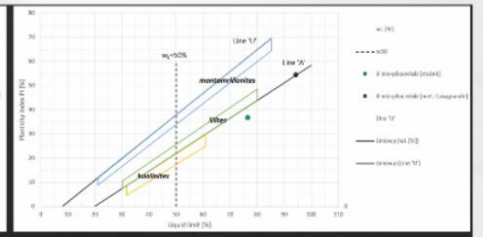

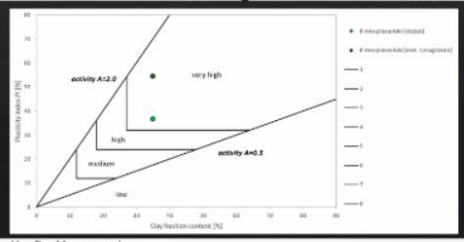

Van Der Merwe graph

Prezi

Ił mioplioceński (ił neogeński)

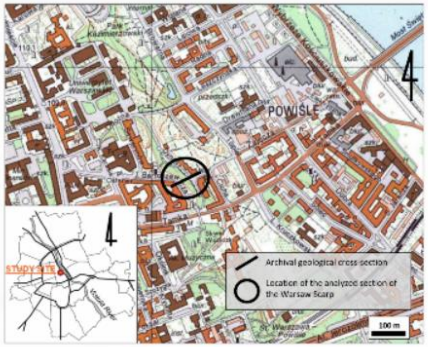

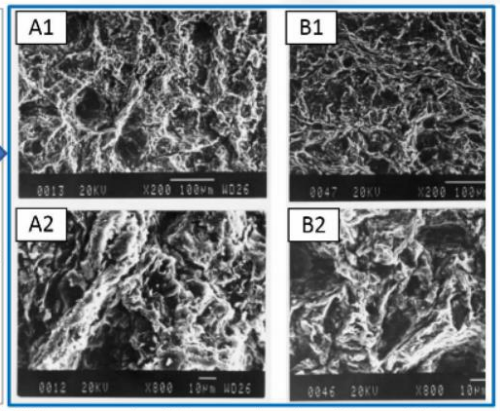

Fig. 1. Distribution of Neogene clays; Typical SEM micrographs of Neogene clays from Warsaw A1,2 - sample STG5, matrix-turbulent microstructure; B1,2 - sample STG11, laminar-turbulent microstructure

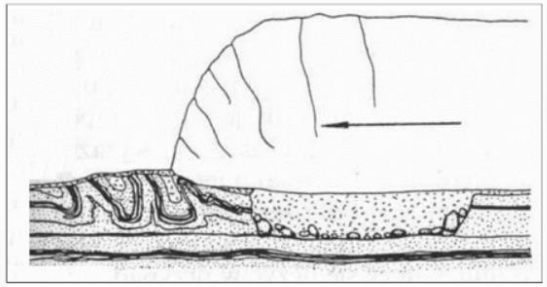

Fig. 2. Glacial tectonic; front of glacier folding

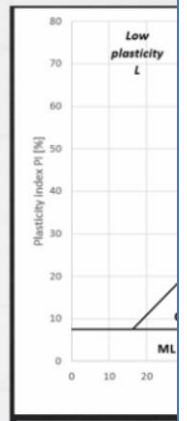

Tab. 1. Zestawienia wyników
iłów miopliocenskich
Table. 1. Results of analysis of
clay

Parametry *Parameters*	
Zawartość frakcji [%] *Fraction content* [%]	<2 µm 2–50 µm >50 µm
Gęstość właściwa, ρ_s, Mg/m³ *Grain density*, ρ_s, *Mg/m³*	
Gęstość objętościowa, ρ, Mg/m³ *Bulk density*, ρ, *Mg/m³*	
Gęstość objętościowa szkieletu, Mg/m³ *Dry density of solid particles*, ρ_s, *M*	
Porowatość [%] *Porosity* [%]	
Wskaźnik porowatości – *e* *Void ratio – e*	
Wilgotność naturalna – *w* [%] *Moisture – w* [%]	

min, max – minimalna i maksymal
maximum value
X – średnia arytmetyczna / *arithm*
n – liczba badań / *number of teste*

Prezi

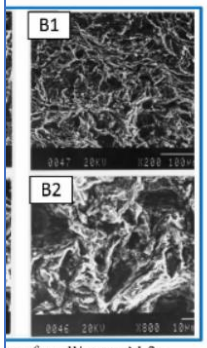

ays from Warsaw A1,2 -
urbulent microstructure

Casagrande graph

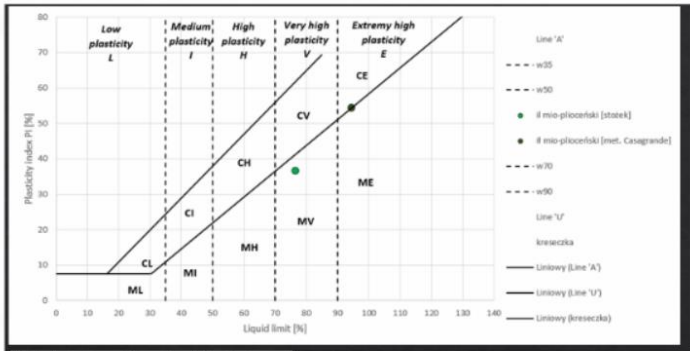

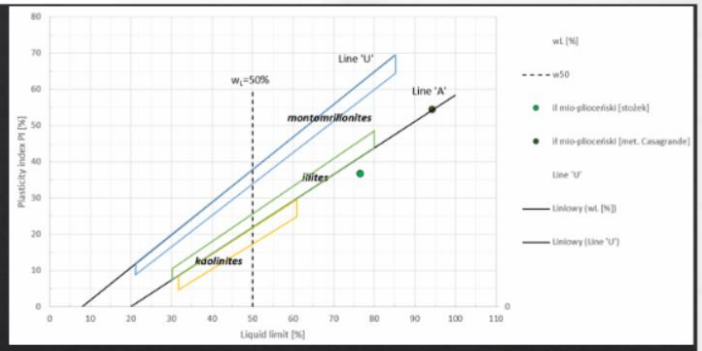

Tab. 1. Zestawienia wyników analizy właściwości fizycznych iłów mioplioceńskich
Table. 1. Results of analysis of physical properties of Mio-Pliocene clay

Parametry *Parameters*		II mioplioceński *Mio-Pliocene clay*	
Zawartość frakcji [%] *Fraction content [%]*	<2 μm	32–39; X = 35;	n = 3
	2–50 μm	38–45; X = 42;	
	>50 μm	16–30; X = 23;	
Gęstość właściwa, ρ_s, Mg/m³ *Grain density, ρ_s, Mg/m³*		2,67–2,70; X = 2,68; n = 5	
Gęstość objętościowa, ρ, Mg/m³ *Bulk density, ρ, Mg/m³*		1,91–1,92; X = 1,92; n = 5	
Gęstość objętościowa szkieletu, ρ_d, Mg/m³ *Dry density of solid particles, ρ_d, Mg/m³*		1,49–1,50; X = 1,50; n = 5	
Porowatość [%] *Porosity [%]*		44–45; X = 44; n = 5	
Wskaźnik porowatości – *e* *Void ratio – e*		0,78–0,80; X = 0,79; n = 5	
Wilgotność naturalna – w [%] *Moisture – w [%]*		22,95–31,85; X = 28,00; n = 6	

min, max – minimalna i maksymalna wielkość parametru / *minimum and maximum value*
X – średnia arytmetyczna / *arithmetic mean*
n – liczba badań / *number of tests*

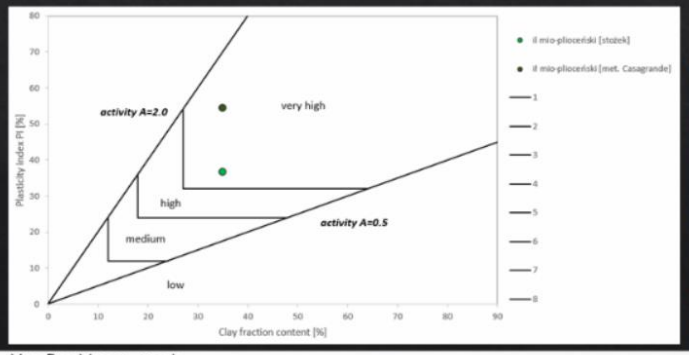

Van Der Merwe graph

2. METHODOLOGY

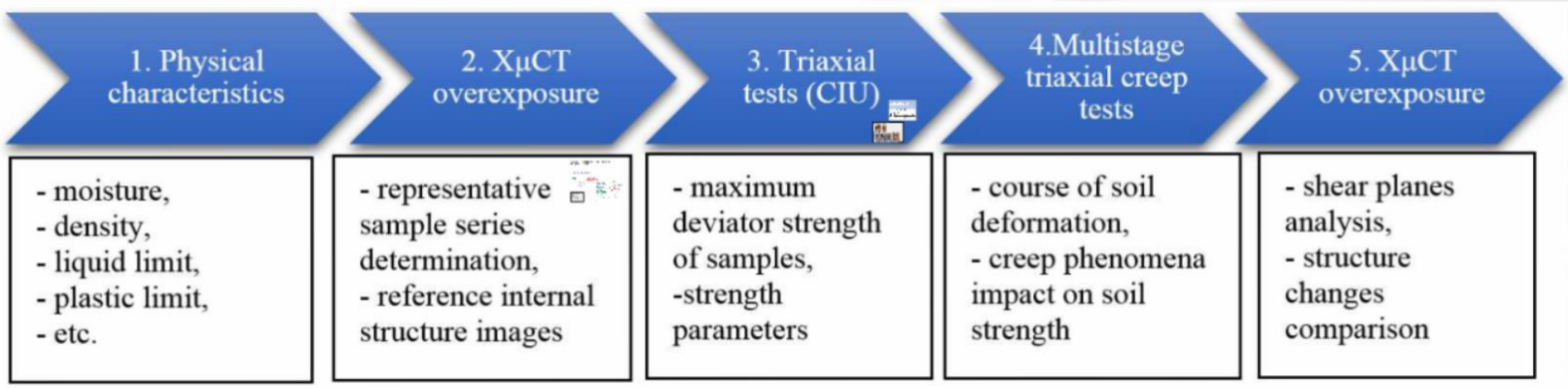

Fig. 5. Workflow of the creep deformation course study

Prezi

2. XμCT overexposure

Prezi

- representative sample series determination,
- reference internal structure images

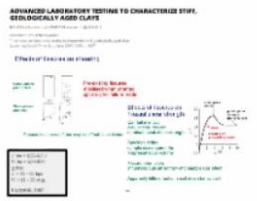

ADVANCED LABORATORY TESTING TO CHARACTERIZE STIFF, GEOLOGICALLY AGED CLAYS

Prof. Richard Jardine | ISSMGE IT Administrator | 23-09-2016

Presenter: Prof. Richard Jardine
Title: Advanced laboratory testing to characterize stiff, geologically aged clays
Launching Date & Time: 1st of June 2015 12:00pm GMT

Effects of fissures on shearing

Observations prior to test

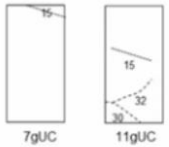

Shear planes after test

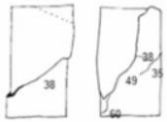

Pre-existing fissures mobilised when oriented optimally for failure mode

Fissures that promote failure may be difficult to see before

Effects of fissures on Triaxial shear strength

Can fail in intact clay, or fissures can dominate peak shear strength

Spacings define sample size required for 'Representative Volume'

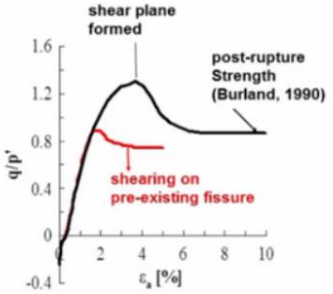

Fissure orientation, influences bulk anisotropy and sample size effect

Apparently little effect on small strain behaviour?

c' zw = 0,55-0,7 c'
fi' zw = 0,7-09 fi'
gdzie:
c' = 25 - 55 kpa
fi' = 12 - 22 stop.

Kaczyński, 2007

3. Triaxial tests (CIU)

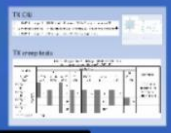

Prezi

Aparat trójosiowego ściskania (TX)

Fig. 3. Identification of the void inside (white arrow) the monolith during the preparation of samples

Fig. 7. Designed specifically for the sample dimensions elements supporting the radial strain sensor

TX CIU

a) 100 kPa for sample 1T (1000kPa of cell pressure, 900 kPa of pore pressure) ➔

b) 200 kPa for sample 2T (in situ stress; 480 cell pressure, 280 kPa of pore pressure) ➔

c) 300 kPa for sample 3T (580 cell pressure, 280 kPa of pore pressure).

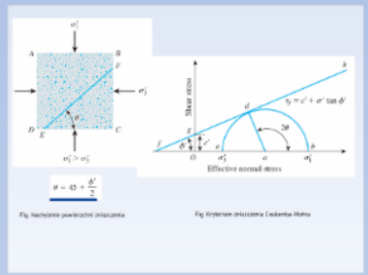

TX creep tests

Table 2. Program for Multistage Triaxial Creep Tests in compression conditions (σ' = 200 kPa)

Test data		Stage No.								Comments
		1	2	3	4	5	6	7	8	
q [kPa]		42.80	57.06	80.84	95.10	109.37	123.63	137.90	152.16	
SL*		0.45	0.60	0.85	1.00	1.15	1.30	1.45	1.60	
Sample 1a	t [days]	20		15						Apparatus malfunction
Sample 1b		6	2	4	5	4.5	1	~0.5		With radial strain sensor
Sample 2			10	10	10	10	10	10	~0	
Sample 3				10	10	10	~0.5			

*Stress level SL = q/q_f [-]

Prezi

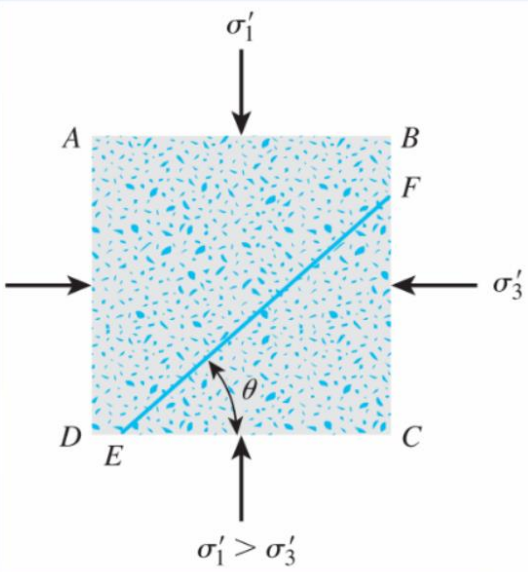

$$\theta = 45 + \frac{\phi'}{2}$$

Fig. Nachylenie powierzchni zniszczenia

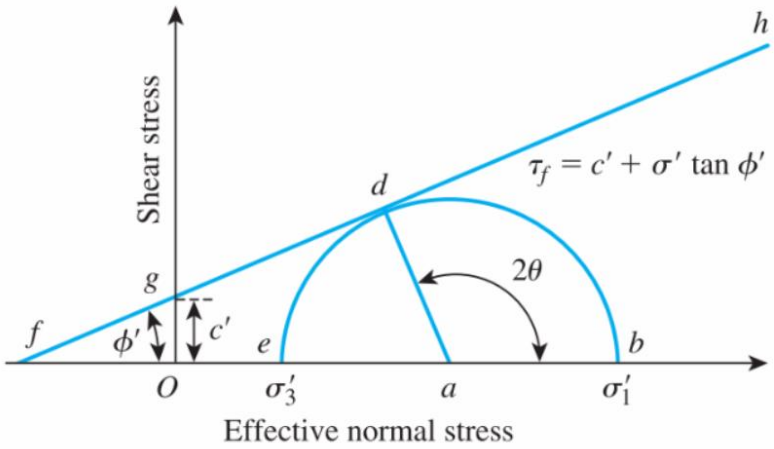

Fig. Kryterium zniszczenia Coulomba-Mohra

4. RESULTS

TX CIU

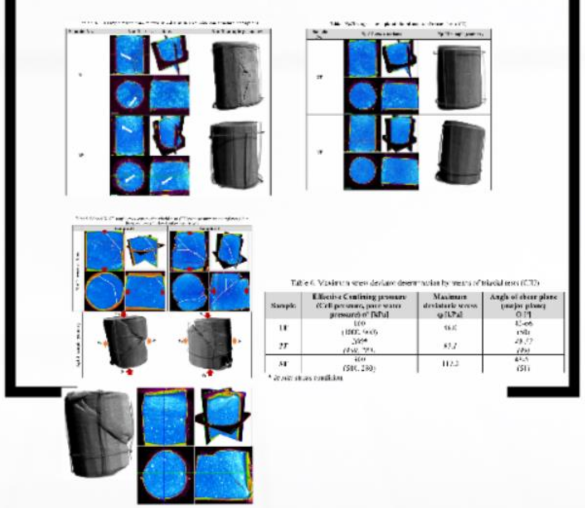

TX creep tests

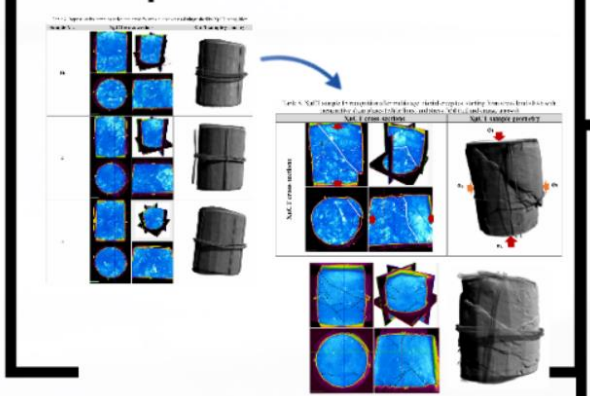

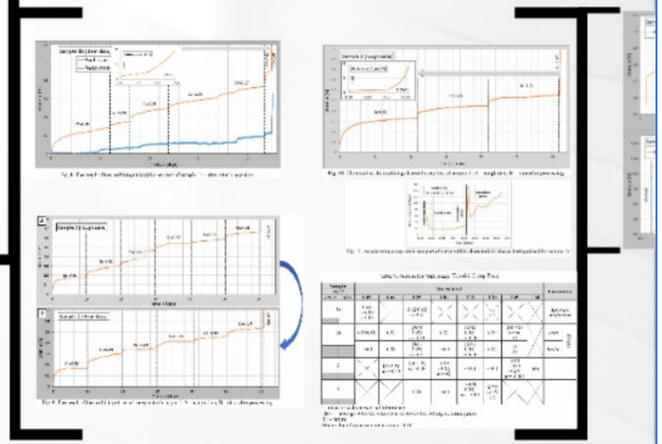

TX CIU

Table 3. XpCT sample recognition - rejected samples (white arrows indicate structure interruption)

Sample No.	XpCT cross-sections	XpCT sample geometry
01	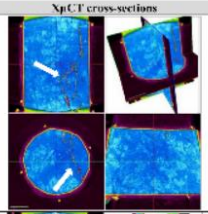	
02	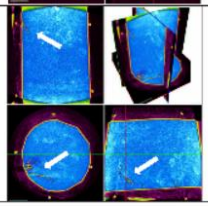	

Table 4. XpCT recognition examples of selected samples before triaxial tests (CIU)

Sample No.	XpCT cross-sections	XpCT sample geometry
2T	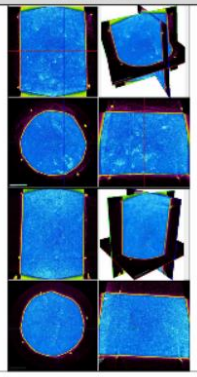	
3T		

Table 5. Selected XpCT sample cross-sections after triaxial tests (CIU) with presumptive shear planes (white lines) and stress field (red and orange arrows)

	Sample 2T	Sample 3T
XpCT cross-sections	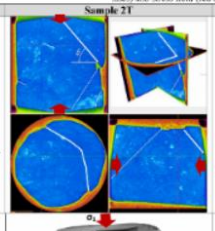	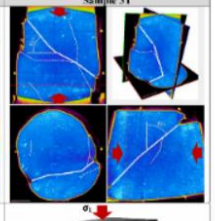
XpCT sample geometry	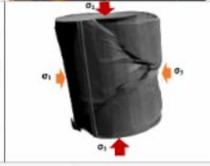	

Table 6. Maximum stress deviator determination by means of triaxial tests (CIU)

Sample	Effective Confining pressure (Cell pressure, pore water pressure) σ' [kPa]	Maximum deviatoric stress q_f [kPa]	Angle of shear plane (major plane) Θ [°]
1T	100 (1000, 900)	86.0	42-66 (50)
2T	*200** *(480, 280)*	*95.1*	*49-57* *(49)*
3T	300 (580, 280)	117.3	43-51 (51)

* *in situ* stress condition

Table 3. XμCT sample recognition - rejected samples (white arrows indicate structure interruption)

Sample No.	XμCT cross-sections	XμCT sample geometry
01	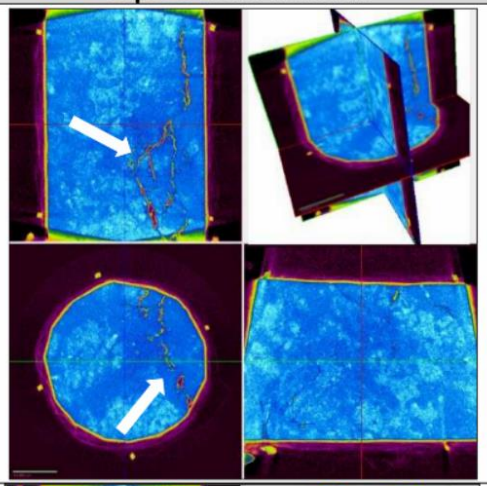	
02	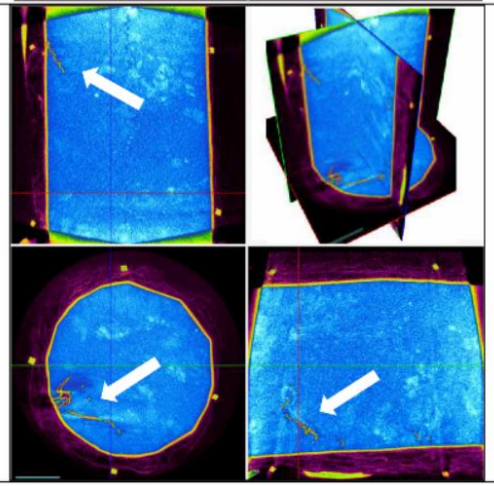	

Table 4. XμCT recognition examples of selected samples before triaxial tests (CIU)

Sample No.	XμCT cross-sections	XμCT sample geometry
2T	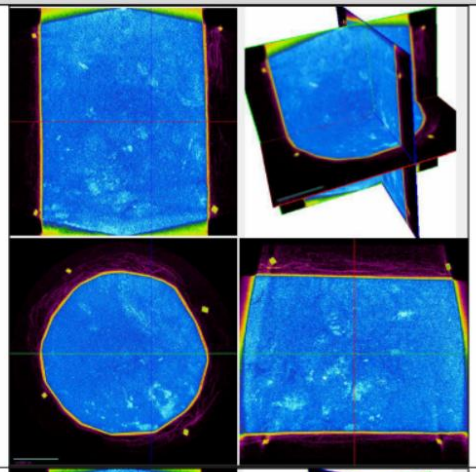	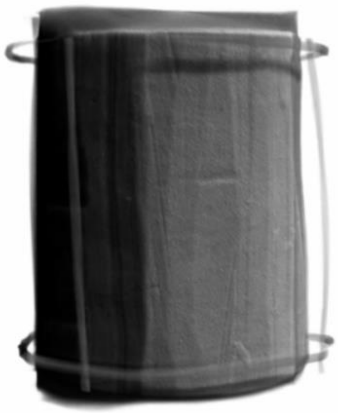
3T	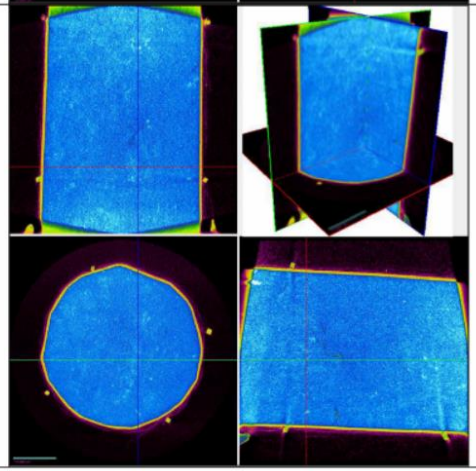	

Table 5. Selected XμCT sample cross-sections after triaxial tests (CIU) with presumptive shear planes (white lines) and stress field (red and orange arrows)

	Sample 2T	Sample 3T
XμCT cross-sections	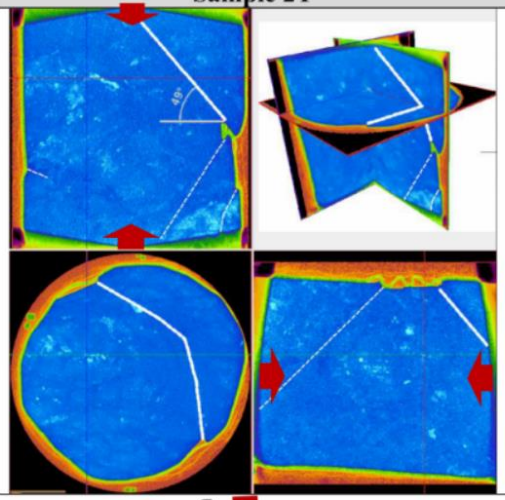	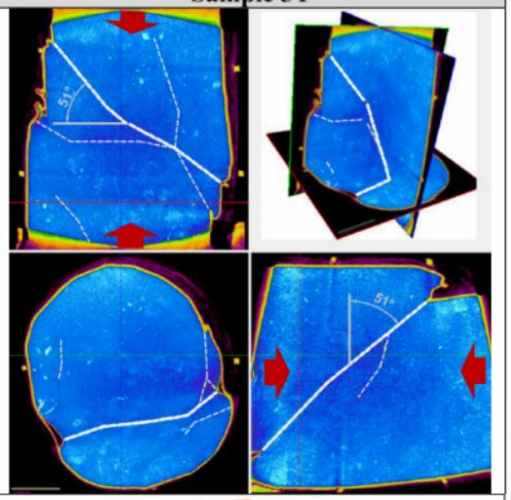
XμCT sample geometry	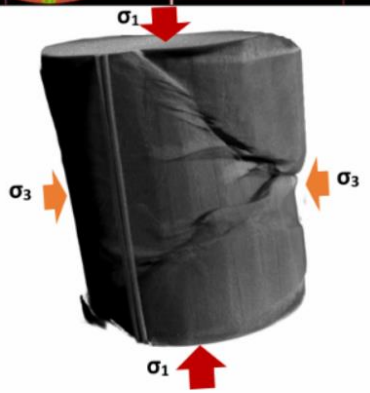	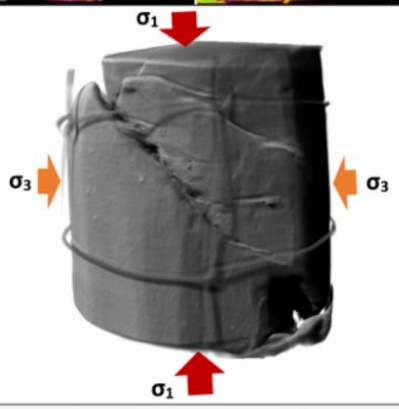

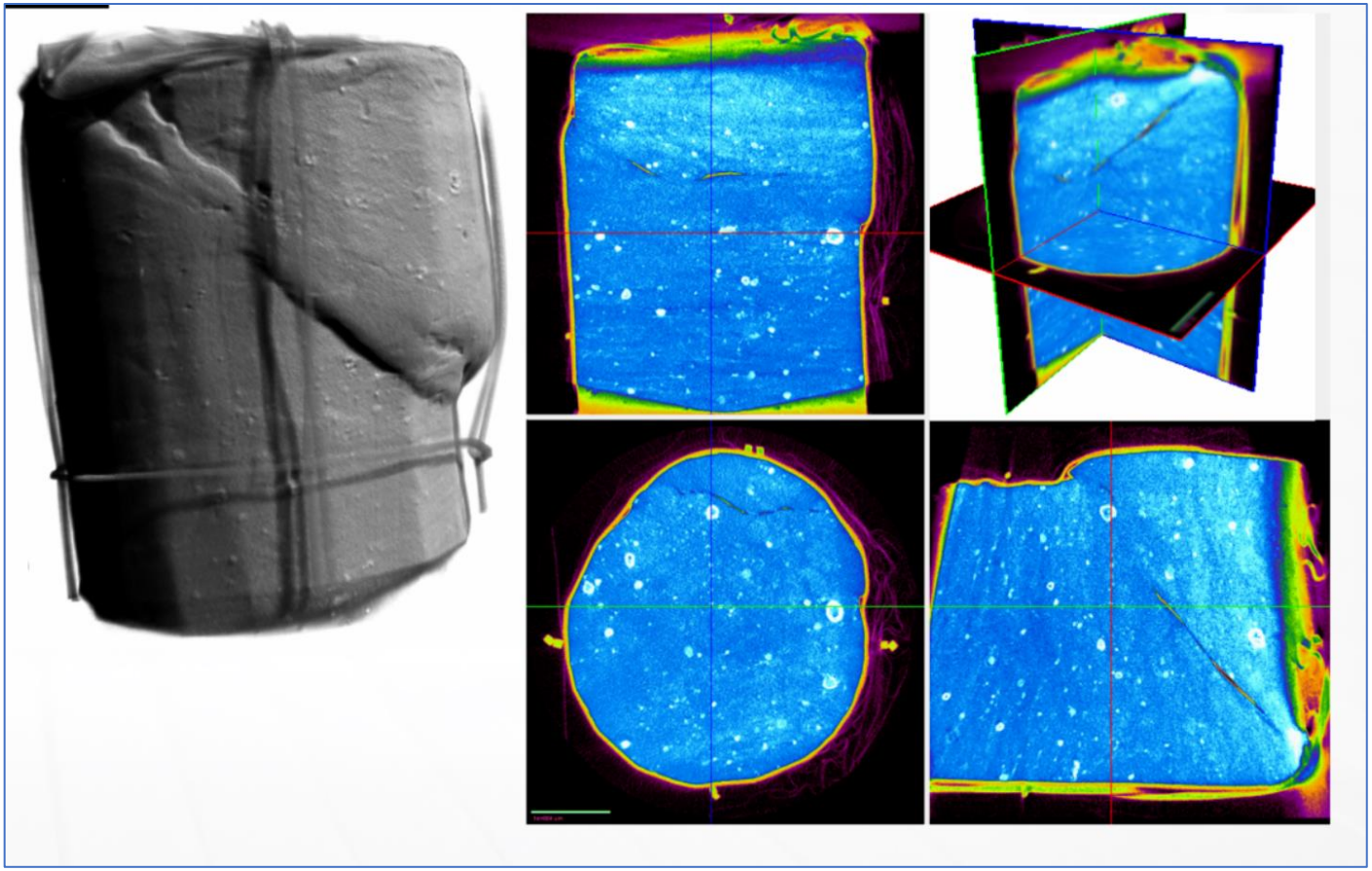

Table 6. Maximum stress deviator determination by means of triaxial tests (CIU)

Sample	**Effective Confining pressure (Cell pressure, pore water pressure) σ' [kPa]**	**Maximum deviatoric stress q_f [kPa]**	**Angle of shear plane (major plane) Θ [º]**
1T	100 (1000, 900)	86.0	42-66 (50)
2T	*200** *(480, 280)*	*95.1*	*49-57* *(49)*
3T	300 (580, 280)	117.3	43-51 (51)

* *in situ* stress condition

Prezi

TX creep tests

Table 7. Representative samples series dedicated for triaxial creep tests distinguished by XμCT recognition

Sample No.	XμCT cross-sections	XμCT sample geometry
1b	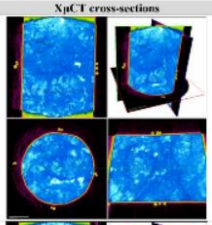	
2	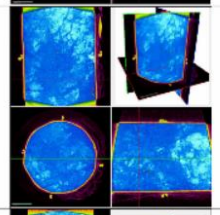	
3	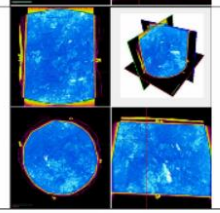	

Table 8. XμCT sample 1b recognition after multistage triaxial creep test starting from stress level=0.45 with presumptive shear planes (white lines) and stress field (red and orange arrows)

	XμCT cross-sections	XμCT sample geometry
XμCT cross-sections	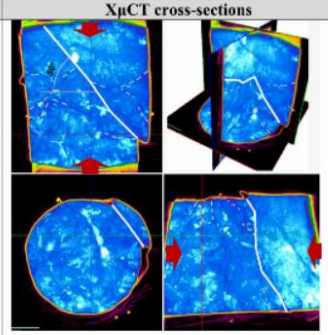	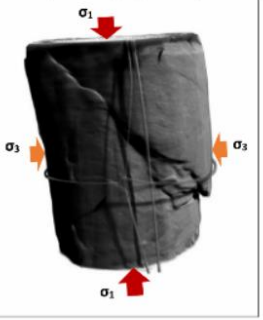

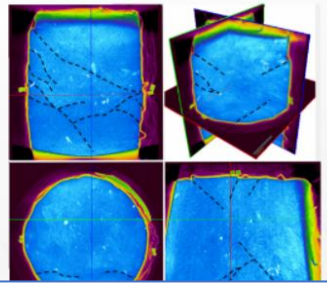

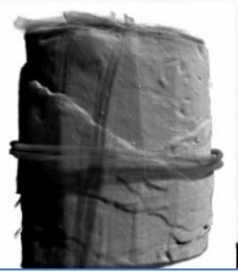

Table 7. Representative samples series dedicated for triaxial creep tests distinguished by XμCT recognition

Sample No.	XμCT cross-sections	XμCT sample geometry
1b	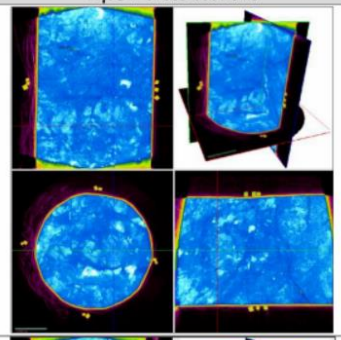	
2	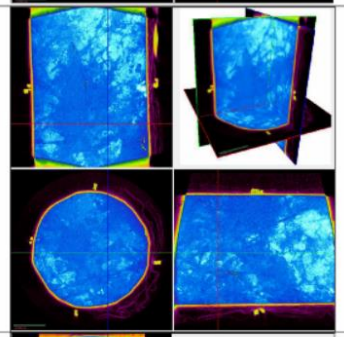	
3	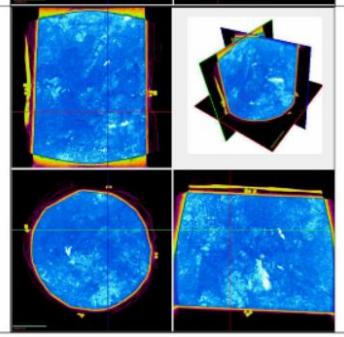	

Table 8. XμCT sample 1b recognition after
presumptive shear planes (w

	XμCT cross-sec
XμCT cross-sections	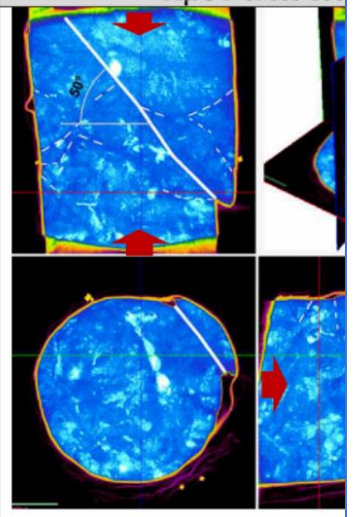

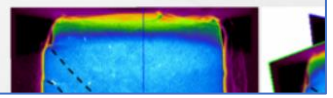

Prezi

Table 8. XμCT sample 1b recognition after multistage triaxial creep test starting from stress level=0.45 with presumptive shear planes (white lines) and stress field (red and orange arrows)

	XμCT cross-sections	XμCT sample geometry
XμCT cross-sections	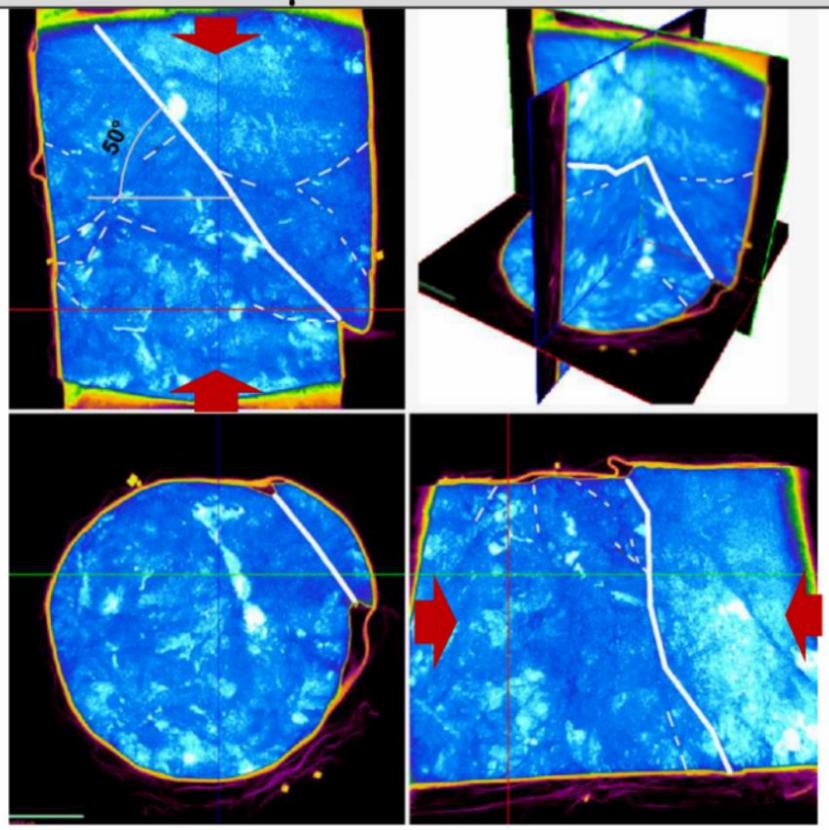	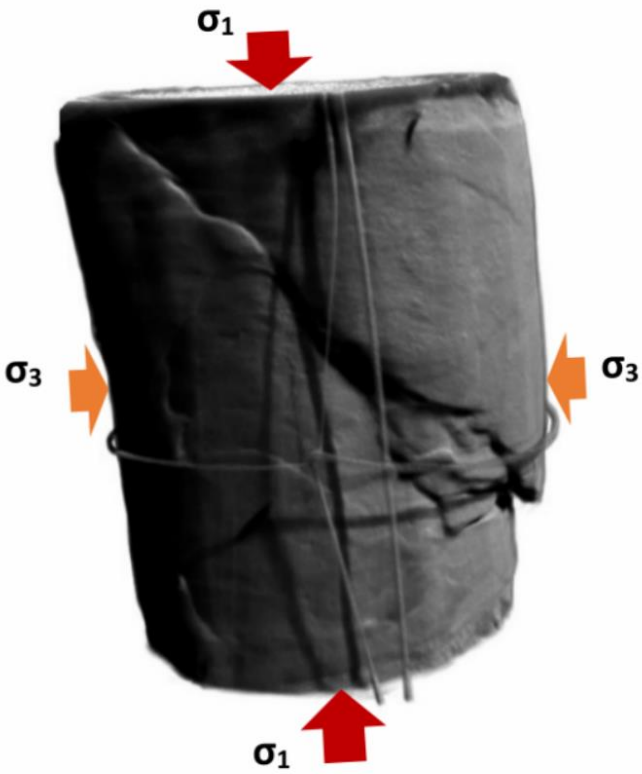

Prezi

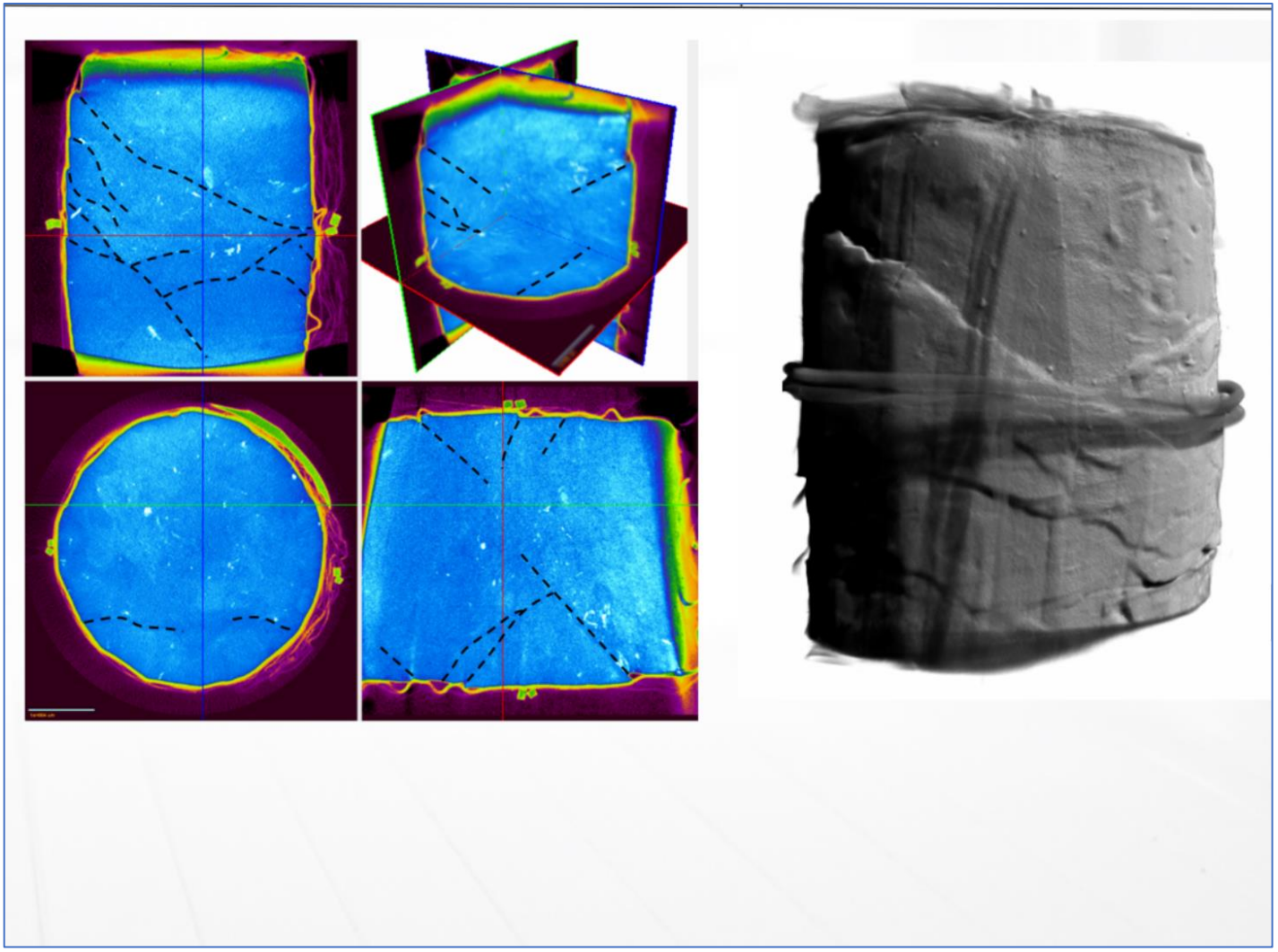

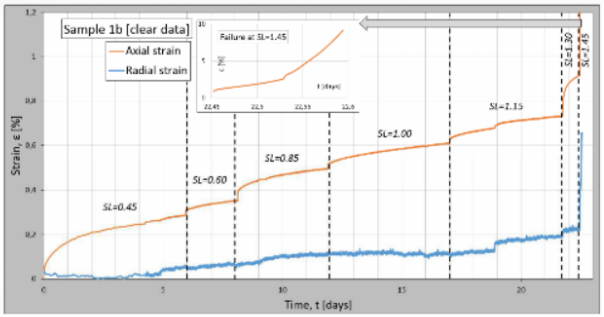

Fig. 8. The result of the multistage triaxial creep test of sample 1b – data after processing

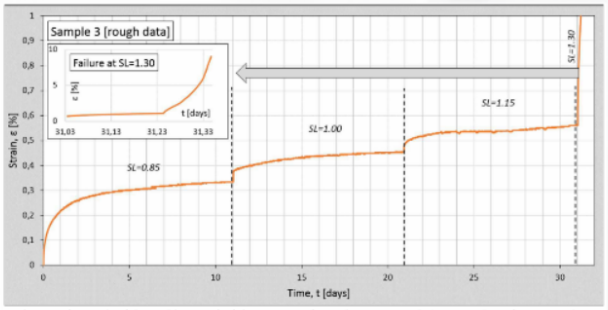

Fig. 10. The result of the multistage triaxial creep test of sample 3: A – rough data; B – data after processing

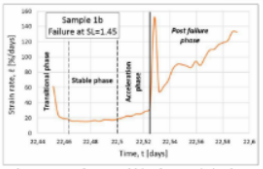

Fig. 11. Accelerating creep strain rate part of curve within characteristic phases distinguished for sample 1b

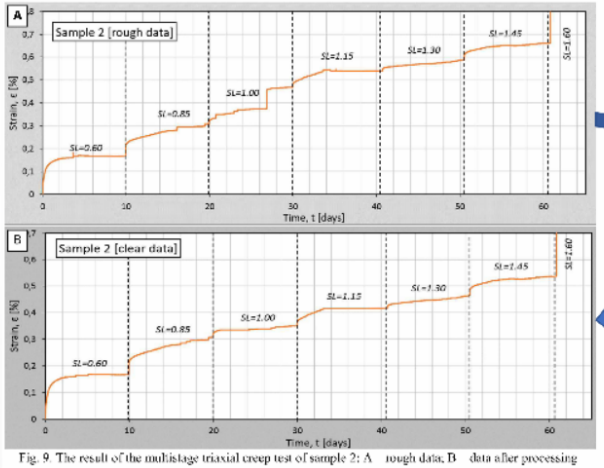

Fig. 9. The result of the multistage triaxial creep test of sample 2: A – rough data; B – data after processing

Table 9. Results for Multistage Triaxial Creep Tests

Sample / XyCT before	Sample / XyCT after	Stress level 0.45	0.60	0.85	1.00	1.15	1.30	1.45	1.60	Comments
1a		0.01 /~0.00 /~0.00	X	{0.02/0.01} av=0.01	X	X	X	X	X	*Apparatus malfunction*
1b		0.01/0.01	0.02	{0.04/ 0.02} av=0.03	0.02	{0.02/ 0.01} av=0.02	0.09	{18/102} av=60 (F)	X	*Axial Strain*
		~0.00	0.01	{0.01/ 0.02} av=0.01	~0.00	{0.01/ 0.01} av=0.01	0.04	11 (F)	X	*Radial*
2		X	{0.02-0} av=~0/~0	{0.01-0} av=~0.00	{0.01 /~0/0} av=~0}	~0.00	~0.00	{0.01 ~0.00 ~0.00/ av=~0.00}	(F)	
3		X	X	0.01	~0.00	{~0.00 0.01} av=~0.00	{2/70} av=27 (F)	X	X	

/ micro ckracks or external intererence
{}av= – average value for whole part of curve after cutting off strain jumps
(F) – failure
Mean value of measurement accuracy: 0.005

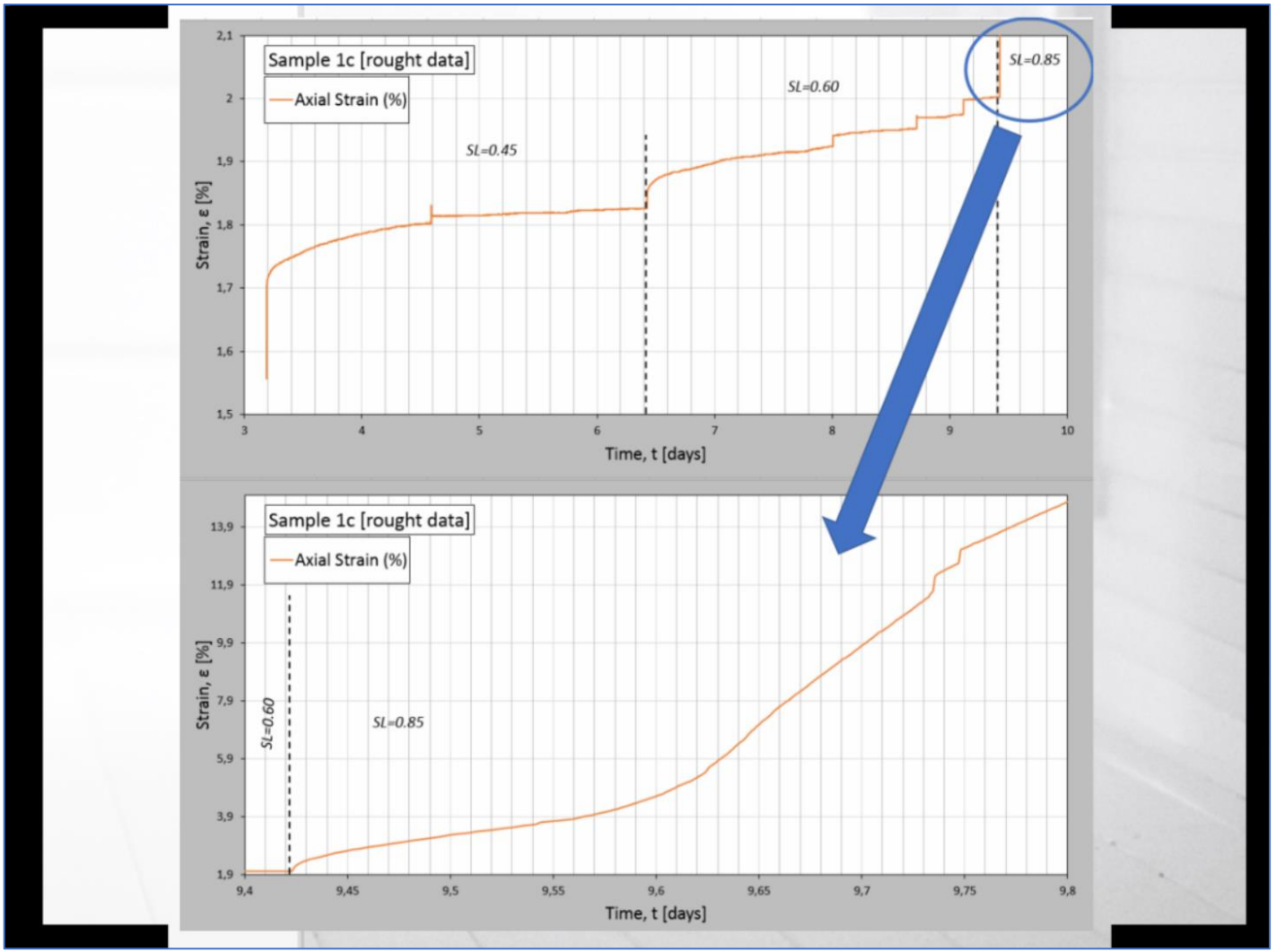
Sample 1c [rought data]
Axial Strain (%)
SL=0.45
SL=0.60
SL=0.85
Strain, ε [%]
Time, t [days]
Sample 1c [rought data]
Axial Strain (%)
SL=0.60
SL=0.85
Strain, ε [%]
Time, t [days]

5. SUMMARY

The study identified the rheological strain course, which can be broken down into three characterizations: decreasing creep strain rate, transitional constant creep velocity, and accelerating creep deformation.

The study found that due to multistage creep loading, the samples were strengthened. Furthermore, there is a visibly "brittle" character of failure, which can be the consequence of redistribution of the microstructure as a function of time as well as collapse of voids. Due to the glacial tectonic of the analyzed samples, the reactivation of micro cracks might also serve as an explanation. The number of the various sizes of shear planes after failure is confirmed by XuCT overexposure.

More detailed summary

From this study following conclusion can be drawn:

•There are three general creep course deformation characterizations: with increasing strain rate, the constant value of deformation, and with decreasing speed of deformation. The creep with increasing strain rate can be broken down into three phases: transitional, stable and accelerating with following failure moment.

•The change of rate strain is similar during the various creep deformation stages up to the stage before the failure, followed by an apparent increase.

•At the destructive stress level after the accelerating creep, the plastic flow occurs. It is worth noting that during the plastic flow the structure impact is observed in the form of abrupt changes of strain rate.

•Under multistage constant creep stress level started below maximum deviatoric stress of the tested sample in the in situ stress state, Neogene clay samples strengthening in function of time.

•The samples under multistage creep stress condition started from 0.45 and 0.60 maximum deviatoric stress obtained higher strengthen than the sample under multistage creep stress condition started from 0.85 deviatoric stress.

•XμCT has improved it is useful for shear plane analysis as well as micro cracks identification and for selection of representative samples series. Furthermore, this method enables for calculation of shear plane angle which is strongly correlated with strength characteristic of the sample (especially with internal friction angle).

Prezi

Zastosowanie mikrotomografii w geoinżynierii: od nauki do praktyki inżynierskiej

Łukasz Kaczmarek

Warszawa, 20.04.2017

BADANIA NUAKOWE

Magnetyczny Rezonans Jądrowy

Wietrzenie skał

Geofizyka

ZASTOSOWANIE W PRAKTYCE

Komputerowa analiza właściwości zbiornikowych przestrzeni porowej piaskowców oraz ich wytrzymałości, na podstawie mikrotomografii rentgenowskiej

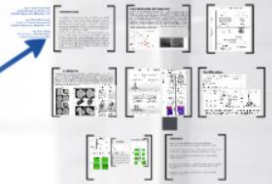

Przebieg pełzania iłu neogeńskiego z Warszawy w badaniach trójosiowych z wykorzystaniem mikrotomografii komputerowej

Prezi

Dziękuję za uwagę

REFERENCES

Baker, D. R., Mancini, L., Polacci, M., Higgins, M. D., Gualda, G. A. R., Hill, R. J., & Rivers, M. L. (2012). An introduction to the application of X-ray microtomography to the three-dimensional study of igneous rocks. Lithos, 148, 262 – 276.

Dvorkin, J., Derzhi, N., Fang, Q., Nur, A., Nur, B., Grader, A., Baldwin, C., Tono, H., & Diaz E. (2009). From micro to reservoir scale: Permeability from digital experiments, The Leading Edge, 28, 1446 – 1452.

Itasca (2015). PFC3D v5.0 User manual. Minneapolis, USA: Itasca Consulting Group,.

Li, X., Konietzky, H., & Li, X. (2016). Numerical study on time dependent and time independent fracturing processes for brittle rocks. Engineering Fracture Mechanics, 163, 89 – 107.

Oszczypko, N., Krzywiec, P., Popadyuk, I., & Peryt, T. (2006). Carpathian Foredeep Basin (Poland and Ukraine): Its Sedimentary, Structural, and Geodynamic Evolution. In: Golonko, J., Picha, F. J. (Eds.). The Carpathians and their foreland: Geology and hydrocarbon resources. AAPG Memoir 84, 293 – 350.

Paszkowski, M., Porębski, S. J., & Warchol M. (2009). Koncepcja projektu otworu kierunkowego w mioceńskich utworach zapadliska przedkarpackiego. Wiadomości Naftowe i Gazownicze, 3(131), 4 – 13.

Petchsingto, T., & Karpyn, Z. T. (2009). Deterministic Modeling of Fluid Flow through a CT-scanned Fracture Using Computational Fluid Dynamics. Energy Sources, Part A: Recovery, Utilization, and Environmental Effects, 31(11), 897–905.

Pstrucha, A., Machowski, G., & Krzyżak A. T. (2016). Petrophysical characterization of the miocene sandstones of the carpathian foredeep (south-east Poland). In 16th International Multidisciplinary Scientific Geoconference GREEN SGEM 2016 (Vol. 3, pp. 891–898). SGEM.

Kaczmarek, Ł. (2016). Możliwości wykorzystania wysokorozdzielczej mikrotomografii komputerowej w badaniach geologiczno-inżynierskich na przykładzie analizy iłów mio-plioceńskich. Przegląd Geologiczny, 64(2), 105-102.

Kaczmarek, Ł. & Kiełbasiński, K. (2016) Propozycja wykorzystania wysokorozdzielczej mikrotomografii komputerowej do analizy gruntu spoistego w badaniach pełzania. Prz. Nauk. Inż. Kszt. Środ., 25(3), 277-289.

Kaczmarek, Ł., Łukasiak, D., Maksimczuk, M., & Wejrzanowski, T. (2015). Wykorzystanie wysokorozdzielczej mikrotomografii komputerowej oraz analizy ultradźwiękowej w charakterystyce struktury paleozoicznych gazonośnych łupków z basenu bałtyckiego. Nafta-Gaz, 71(12), 1017–1023.

Kaczmarek, Ł., Machowski, G., Maksimczuk, M., & Wejrzanowski, T. (2015). Strukturalna analiza mioceńskich piaskowców z zapadliska przedkarpackiego za pomocą wysokorozdzielczej mikrotomografii komputerowej. Nafta-Gaz, 71(9), 647–654.

Kaczmarek, Ł., Kozłowska, A., Maksimczuk, M., & Wejrzanowski, T. (2017). The use of X-ray computed microtomography for graptolite detection in rock based on core internal structure visualization. Acta Geologica Polonica, (in press).

Krzyżak, A., & Kaczmarek, Ł. (2016). Comparison of the efficiency of 1H NMR and μCT for determining the porosity of the selected rock cores. In 16th International Multidisciplinary Scientific Geoconference GREEN SGEM 2016 (Vol. 4, pp. 81–88). SGEM.

Prezi